

UC Riverside

UC Riverside Electronic Theses and Dissertations

Title

Graphene and its Hybrid Nanostructures for Nanoelectronics and Energy Applications

Permalink

<https://escholarship.org/uc/item/61b5j7f4>

Author

LIN, JIAN

Publication Date

2011

Peer reviewed|Thesis/dissertation

UNIVERSITY OF CALIFORNIA
RIVERSIDE

Graphene and its Hybrid Nanostructures for Nanoelectronics and Energy Applications

A Dissertation submitted in partial satisfaction
of the requirements for the degree of

Doctor of Philosophy

in

Mechanical Engineering

by

Jian Lin

June 2011

Dissertation Committee:

Dr. Cengiz S. Ozkan, Chairperson

Dr. Mihrimah Ozkan

Dr. Kambiz Vafai

Copyright by
Jian Lin
2011

The Dissertation of Jian Lin is approved:

Committee Chairperson

University of California, Riverside

Acknowledgements

I would like to express my most sincere gratitude to all those who provided me the support during my Ph.D. work.

First of all, from the bottom of my heart, I would like to give my sincere appreciation to my research advisor Professor Cengiz Okzan and co-advisor Professor Mihrimah Ozkan for their guidance, encouragement and financial support throughout the whole course of my Ph.D. work. I genuinely appreciate their kindness of giving me the freedom of implementing the research projects that interested me the most. Their amiable personalities, support of cultural diversity, and their encouragement of independent and original ideas and work, have had a compelling influence on me on both academic and personal levels.

Also, I would like to thank Professor Kambiz Vafai for serving as my committee member in both the qualify exam and Ph.D. defense. Also, I want to give my deepest thanks to Professor Roger Lake and Professor Guanshui Xu for their kindness to participate in my qualify exam committee, special thanks to Professor Roger Lake for his invaluable advice on my first journal paper.

It is my honor to work with such wonderful colleagues under the comfortable and inspiring environment, thus I would like to acknowledge the former and current research members including Dr. Alfredo Martinez-Morales, Miroslav Penchev, Jiebin Zhong, Liang Wang, Dr. Yu Zhang, Dr. Xiaoye Jing, Dr. Xu Wang, Dr. Ibrahim Khan, Dr. Emre Yengel, Jennifer Reiber Kyler, Shirui Guo, Ali Guvenc, Rajat Paul, Mazair Ghazinejad, Engin Akin, Wei Wang, Aaron Scott George, Issac Ruiz. I want to express my special

thanks to Dr. Alfredo Martinez-Morales who mentored me when I first joined this group. His always positive attitudes toward work and life have been a great motivation for me. I could not thank Miroslav Penchev more, with whom I have shared and discussed everything from research topics, philosophy, and politics to personal life. The friendship with these colleagues I made during my Ph.D. time I will cherish for a lifetime.

I would like to thank my friends, especially the staff Mark Heiden, Dexter Humphrey, Dong Yan in CNSE at UCR. They could always provide the immediate and genuine help to move forward the research projects. I also want to give my sincere thanks to my other friends who are always supporting me, and not to incriminate too many people, I will leave you guys nameless.

Finally, I would like to give my thanks to my family for their unconditional love and support, special thanks to my wife who is always beside me, through the good and the bad times. Her love makes my life colorful and meaningful.

ABSTRACT OF THE DISSERTATION

Graphene and its Hybrid Nanostructures for Nanoelectronics and Energy Applications

by

Jian Lin

Doctor of Philosophy, Graduate Program in Mechanical Engineering
University of California, Riverside, June 2011
Dr. Cengiz S. Ozkan, Chairperson

This dissertation focuses on investigating the synthesis of graphene and its hybrid nanostructures by chemical vapor deposition (CVD) process, as well as their applications in nanoelectronics and energy conversion/storage. The substantial understanding of interaction of graphene layers between the bio-molecules and gas molecules will enable the improvement in the applications of graphene in bio-sensor and chemical sensor. To achieve these objectives, graphene field effect transistors are fabricated to study the interactions of graphene between single stranded Deoxyribonucleic Acids (ssDNA) and gas molecules. ssDNA is found to act as negative potential gating agent that increases the hole density in single layer graphene (SLG). The molecular photodesorption and absorption from pristine and functionalized graphene are studied. The photodesorption induced current decrease in functionalized graphene by concentrated HNO_3 becomes less significant than pristine graphene layers. We suggest this is due to the passivation of oxygen-bearing functionalities to CVD grown

graphene structure defects via HNO_3 functionalization, which prevents the further absorption of gas molecules.

The advance of synthesis of graphene and its hybrid nanostructures by CVD promotes their applications in the industrial level. We synthesize the graphene both on nickel thin film and copper foils by CVD, and investigate the grow kinetics, such as the effect of growth pressure on the uniformity and quality of Cu-grown graphene. By controlling the growth pressure we achieve uniform single layer graphene sheets and suggest the feasible methods of synthesizing uniform few-layer graphene. To decrease the sheet resistance, we stack the single layer graphene using layer-layer transfer technique. Highly concentrated HNO_3 is employed to improve the conductivity and surface wettability of graphene layers. Four-layer graphene films with optical transmittance of 90% after HNO_3 treatment are applied in organic solar cell as anode. Further, we report the fabrication of highly conductive, large surface-area 3D pillar graphene nanostructures (PGN) films from assembly of vertically aligned CNT pillars on flexible copper foils and directly employed for the application in electrochemical double layer capacitor (EDLC). The PGN films with MWCNTs on graphene layers, which were one-step synthesized on flexible copper foil (25 μm) by CVD process, exhibit high conductivity with sheet resistance as low as 1.6 Ohm per square and high mechanical flexibility. The fabricated EDLC supercapacitor based on high surface-area PGN electrodes ($563\text{m}^2/\text{g}$) showed high performance with high specific capacitance of 330F/g.

We demonstrate the synthesis and characterization of three dimensional heterostructures graphene hybrid nanostructures (HGN) comprising continuous large area

graphene layers and ZnO nanostructures, fabricated via two-step CVD process. The material characterizations exhibit the highly crystalline ZnO nanostructures synthesized on few-layer graphene film. Ultraviolet spectroscopy and photoluminescence spectroscopy indicate that the CVD grown HGN layers has excellent optical properties. The electrical study on the graphene/ZnO/graphene devices suggests that graphene readily form Ohmic contact to ZnO, although rarely Shockley may exist. The electron transport properties highly depend on the temperature. Devices show photoconductive effect under UV illumination. A combination of electrical and optical properties of graphene and ZnO building blocks in ZnO based HGN provides unique characteristics for opportunities in future optoelectronic devices.

Table of Contents

Title Page

Copyright Page

Signature Page

Acknowledgements.....iv

Abstract.....vi

Table of Contents.....ix

List of Figures.....xiii

List of Table.....xxi

Chapter 1 Introduction

1.1 Graphene.....1

1.1.1 History of Graphene.....1

1.1.2 Graphene Crystal and Band Structures.....2

1.1.3 Properties and Applications of Graphene7

1.1.3.1 Field Effect Transistor and Integrate Circuits.....8

1.1.3.2 Graphene Based Chemical and Bio Sensor.....9

1.1.3.3 Transparent and Conducting Electrode.....11

1.1.3.4 Supercapacitor.....15

1.2 Synthesis of Graphene.....18

1.2.1 Exfoliation and Cleavage.....18

1.2.2 Thermal Decomposition of SiC.....20

1.2.3 Chemical Vapor Deposition.....21

1.2.4 Other Methods.....	25
1.3 Graphene Hybrid Nanostructures: Synthesis and Applications.....	27
1.4 Thesis Outline.....	31
Chapter 2 Graphene Field Effect Transistors for Studying the Interactions Between Graphene and Bio/gas Molecules	
Abstract.....	34
2.1 DNA Negative Gating Effect in Single Layer Graphene.....	36
2.1.1 Introduction.....	36
2.1.2 Material and Experimental Methods.....	37
2.1.3 Material and Electrical Characterizations.....	38
2.1.4 Raman Spectroscopy Characterization.....	44
2.1.5 Modeling and Theoretical Investigation.....	46
2.1.6 Conclusion.....	50
2.2 Gas Molecular Absorption and Photodesorption in Pristine and Functionalized Large-area Graphene Layers.....	51
2.2.1 Introduction.....	51
2.2.2 Materials and Experimental Methods.....	52
2.2.3 Molecular Absorption and Photodesorption of Pristine Graphene.....	54
2.2.4 Molecular Absorption and Photodesorption of Functionalized Graphene.....	58
2.2.5 Conclusion.....	63
2.3 Conclusion.....	64

Chapter 3 Synthesis of Graphene by Chemical Vapor Deposition and its Application in Organic Solar Cell

Abstract.....	65
3.1 Introduction.....	66
3.2 Material Synthesis and Experimental Methods.....	67
3.2.1 Material Synthesis.....	67
3.2.2 Graphene FET and Solar Cell Devices Fabrication.....	69
3.2.3 Experimental Methods.....	70
3.3 Results and Discussion.....	71
3.3.1 Growth Kinetic of CVD Graphene Synthesized on Ni Thin Films and Cu Foils.....	71
3.3.2 Organic Solar Cell Based on Few-layer Graphene	77
3.4 Conclusion.....	81

Chapter 4 Synthesis of Pillar Graphene Nanostructures and its Application in Supercapacitor

Abstract.....	82
4.1 Introduction.....	83
4.2 Material Synthesis and Experimental Methods	84
4.2.1 Material Synthesis.....	84
4.2.2 Experimental Methods.....	86
4.3 Results and Discussion.....	84
4.3.1 Material Characterizations of PGN.....	86

4.3.2 Supercapacitor Based on Flexible Pillar Graphene Nanostructures.....	94
4.4 Conclusion.....	98
Chapter 5 Synthesis of Heterogeneous Graphene/ZnO Hybrid Nanostructures and Studies on Their Electrical and Photoelectrical Properties	
Abstract.....	99
5.1 Introduction.....	101
5.2 Synthesis of Graphene/ZnO Hybrid Nanostructures.....	103
5.2.1 Material Synthesis and Experimental Methods.....	103
5.2.2 Material Characterizations.....	105
5.2.3 Optical Properties of Graphene/ZnO Hybrid Nanostructures.....	111
5.2.4 Growth Mechanism.....	112
5.3 Studies on Electrical and Photoelectrical Properties of Graphene/ZnO/Graphene Hybrid Nanostructures.....	113
5.3.1 Material Characterizations.....	113
5.3.2 Electrical Properties of Graphene/ZnO/Graphene Hybrid Nanostructures.....	115
5.3.3 Photoelectrical Properties of Graphene/ZnO/Graphene Hybrid Nanostructures.....	119
5.4 Conclusion.....	121
Chapter 6 Conclusions.....	122
Reference.....	125

List of Figures

Figure 1.1 Various structural forms of carbon from zero to three-dimensions.....	2
Figure 1.2 Graphene is 2D building material that can be wrapped to 0D buckminsterfullerene, rolled into 1D carbon nanotube and stacked to graphite.....	3
Figure 1.3 (a) Electron orbitals in graphite. (b) Electron orbital of graphene: sp^2 hybridized orbital responsible for the bonding on x-y plan; 2p orbital perpendicular to the x-y plan.....	4
Figure 1.4 a) Direct lattice of graphene. Shaded area is the primitive unit cell. (b) Reciprocal lattice of graphene. Shaded area is the first Brillouin Zone defined by the vector b_1 and b_2	5
Figure 1.5 (a) Crystal structure of graphene. (b) Band structure of graphene. The right zoom-in is conical energy band spectrum associated with sublattices intersected at zero E near the edge of Brillouine zone.....	6
Figure 1.6 Evolution of MOSFET gate length in integrated circuits (filled red circle) and International Technology Roadmap for semiconductor targets (open red circle). The number of transistor per processor (blue stars).....	7
Figure 1.7 (a) Electron mobility versus bandgap engineering in low electrical fields for different material. (b) Carrier mobility versus graphene nanoribbon width from simulation and experiment.....	9
Figure 1.8 Single molecule detection based on graphene field effect transistor.....	10
Figure 1.9 Response of the graphene sensor to 2,4 dinitrotoluene.....	10
Figure 1.10 (A) Photograph of 50um aperture covered by graphene and its bilayer. (B) Transmittance spectrum of single-layer graphene. (Inset) Transmittance of white light as function of number of graphene layers.....	12

Figure 1.11 (A) Schematic of dye-sensitized solar cell using graphene film as electrode. (B) The energy diagram of dye-sensitized solar cell. (C) I-V curve of graphene (black) and FTO based solar cell.....13

Figure 1.12 (a) Raman spectra of graphene films with different number of stacked layers. (b) UV-vis spectra of layer-by-layer transferred graphene films on quartz substrate. (c) Roll-to-roll transfer of graphene film from thermal release tape to PET film at 120 °C. (d) An assembled graphene/PET touch panel showing outstanding flexibility. (e) A transparent graphene film transferred on a 35-inch PET sheet. (f) A graphene-based touch screen panel connected to computer with control software.....15

Figure 1.13 (a) SEM image of graphene particles. (b) TEM image showing individual graphene sheets. (c) Low and high magnification SEM image of graphene electrode. (d) Schematic of test cell.....17

Figure 1.14 Various spectroscopic analyses of the large-scale graphene films grown by CVD. (a) SEM images of as-grown graphene films on thin (300-nm) nickel layers and thick (1-mm) Ni foils (inset). (b) TEM images of graphene films of different thicknesses. (c) An optical microscope image of the graphene film transferred to a 300-nm-thick silicon dioxide layer. The inset AFM image shows typical rippled structures. (d) A confocal scanning Raman image corresponding to c. The number of layers is estimated from the intensities, shapes and positions of the G-band and 2D-band peaks. (e) Raman spectra (532-nm laser wavelength) obtained from the corresponding coloured spots in c and d. a.u.: arbitrary units.....22

Figure 1.15 (A) SEM image of graphene transferred on SiO₂/Si (285-nm thick oxide layer) showing wrinkles, and 2 and 3 layer regions. (B) Optical microscope image of the same regions as (A). (C) Raman spectra from the marked spots with corresponding colored circles or arrows showing the presence of graphene, 2 layers of graphene and 3 layers of graphene; (D, E, and F) Raman maps of the D (1300 to 1400 cm⁻¹), G (1560 to 1620 cm⁻¹), and 2D (2660 to 2700 cm⁻¹) bands, respectively (WITec alpha300, $\lambda_{\text{laser}} = 532$ nm, ~500 nm spot size, 100 objective). Scale bars are 5 μm24

Figure 1.16 Nanoribbon formation and imaging. (a) Representation of the gradual unzipping of one wall of a carbon nanotube to form a nanoribbon. Oxygenated sites are not shown. (b) The proposed chemical mechanism of nanotube unzipping. The manganate ester could also be protonated. (c) TEM images depicting the transformation of MWCNTs (left) into oxidized nanoribbons (right). The right-hand side of the ribbon is

partly folded onto itself. The dark structures are part of the carbon imaging grid.....26

Figure 1.17 Schematic of three types of graphene hybrid nanostructures.....28

Figure 1.18 (a) Schematic illustration of the fabrication process for CCG/CNT composite films. (b) SEM image of cross section of CCG/CNT composite film prepared following the process illustrated in (b). (c) SEM image of pattern CNT on CCG film.....30

Figure 2.1 Raman spectrum collected from the SLG between two contacts after device fabrication showing the typical features. The absence of the D-band indicates that no substantial damage was caused during the fabrication process and electrical measurements.....39

Figure 2.2 (a), (b) AFM images ($1.1\text{ }\mu\text{m}\times 1.1\text{ }\mu\text{m}$, Z-range 15nm) and accordingly cross sectional profiles of SLG before (a) and after (b) patterning with ssDNA. The measured thickness of SLG increases from $\sim 1.0\text{nm}$ to $\sim 1.8\text{nm}$ after ssDNA patterning. And the increased roughness (shown in two squares in image (a) and (b)) is due to the nonspecific and irregular binding of ssDNA to the SLG. The scale bar are 200nm. Color bar is 10nm.....40

Figure 2.3 $I_{\text{ds}}-V_{\text{gs}}$ characteristics of SLG before (black) and after (red) ssDNA patterning of SLG devices at $T=300\text{K}$. Source-drain bias voltage is 100mV. The dotted lines correspond to the Dirac point (Minimum conductance point). From the current-voltage measurements, it shows: (1) the gate voltage when minimum conductance point reaches shifts from 60V to 80V; (2) overall conductance shifts up. The top inset is the SEM image of the SLG device used in the measurements. The device channel length and effective width are $1.8\text{ }\mu\text{m}$ and $0.6\text{ }\mu\text{m}$ respectively.....42

Figure 2.4 Micro-Raman spectroscopy of the signature G-peak and the 2D band for pristine SLG and the ssDNA/SLG system. In (a) the G-peak is centered at 1580cm^{-1} , observed at 488nm excitation wavelength, shifts an average 2cm^{-1} after ssDNA patterning. (b) Second order 2D band shifts by $\sim 4\text{cm}^{-1}$ as a result of ssDNA patterning. Both signature peaks also show relative shortening of their respective full width half max (FWHM) values.....45

Figure 2.5 (a) An adenine neocleoside on the graphene supercell. (b) Energy versus k relation of a pristine graphene sheet along the armchair direction. A supercell is used for repeat unit that contains 16 layers in the zigzag direction and 12 layers in the armchair direction. The dotted line shows the charge neutral Fermi level of the system. (c) Energy versus k relation of a graphene sheet with physisorbed adenine neocleoside. The dimensions of the graphene supercell is identical to the one used for (b). The dotted line shows the charge neutral Fermi level of the system.....48

Figure 2.6 Molecular photodesorption of CVD grown graphene layers before HNO₃ treatment. (a) Raman spectra of CVD grown graphene indicating single layer and few-layer graphene region. (b) Normalized conductivity G/G_i [initial conductivity: $G_i = (4\text{k}\Omega)^{-1}$] of a GFET vs time during UV illumination cycles in ambient air. Shaded and unshaded regions represent the UV-on and -off periods respectively. The inset is the optical image of a four-contact GFET device. (c) Transfer characteristics of GFET under continuous UV illumination in vacuum ($p=10\text{mTorr}$). Inset: Correspondingly extracted transconductance of the same device. (d) Sheet resistance changes with time under UV illumination. (e) Normalized conductivity [initial conductivity: $G_i = (4.4\text{k}\Omega)^{-1}$] of GFET devices during NH₃ absorption and photo-desorption cycles. Shaded regions represent the UV-on periods. The samples were degassed before NH₃ absorption and photo-desorption. (f) Transfer characteristics of NH₃ absorbed GFET under continuous UV illumination in vacuum ($p = 10 \text{ mTorr}$).....55

Figure 2.7 (a) Raman spectra of pristine and HNO₃ treated CVD grown single-layer graphene region. About 8.5cm^{-1} of a blue shift for the G peak is observed in the spectra, showing the strong p-type doping effect of HNO₃. Inset is the Raman spectrum of single layer graphene region chose for comparison before and after HNO₃ treatment. (b) Transfer characteristics ($I_{ds}-V_{gs}$) of GFET measured under vacuum ($p=10\text{mTorr}$) before and after HNO₃ functionalization.....59

Figure 2.8 Normalized conductivity G/G_i [initial conductivity $G_i = (3.1\text{k}\Omega)^{-1}$] of CVD grown graphene layers before and after HNO₃ functionalization vs time in vacuum ($p = 10 \text{ mTorr}$).....60

Figure 2.9 Molecular absorption and desorption of CVD grown graphene layers before and after HNO₃ functionalization under different pressures. (a) Normalized conductivity G/G_i [$G_i = (4.6\text{k}\Omega)^{-1}$] of graphene layers before functionalization in air under different pressures. (b) Normalized conductivity [$G_i = (3.9\text{k}\Omega)^{-1}$] of graphene layers after functionalization in air under different pressures. (c) Normalized conductivity [$G_i = (4.2\text{k}\Omega)^{-1}$] of graphene layers before functionalization in NH₃ under different pressures. (d) Normalized conductivity [$G_i = (5\text{k}\Omega)^{-1}$] of graphene layers after functionalization in

NH₃ under different pressures. All of samples were degassed under UV illumination and voltage annealing under vacuum prior to electrical measurements.....62

Figure 3.1 Schematic of synthesis of large-area graphene films by chemical vapor deposition (CVD). (A) Schematic of vacuum tube furnace. (B) Synthesis and transfer procedure of graphene by CVD.....68

Figure 3.2 Raman spectrums of monolayer, bi-layer and few-layer CVD grown graphene on Ni thin film. Individual spectra correspond to spots indicated on the graphene layer (inset optical micrograph), in which the darker spots represent thicker graphene layers. Excitation wavelength is 514 nm.....71

Figure 3.3 (a) Transmission electron micrograph of a few-layer graphene area grown from nickel thin film and the corresponding electron diffraction pattern. (b) AFM image of a selected few-layer graphene region, color scale bar is 10nm. The inset figure shows the height measurement on the position indicated by the red line. The measured height is around 1.5nm indicating the presence of less than 5 graphene layers.....72

Figure 3.4 Optical images and the corresponding Raman spectra of transferred graphene (from copper) on 300 nm SiO₂ synthesized under different growth pressures (shown in table 1) using Cu as a catalyst at the same methane gas compositions and growth temperature: (a)S1; (b)S2; (c)S3; (d)S4; (e)S5. Scale bars: 10 μ m.....74

Figure 3.5 The corresponding Raman spectra of transferred graphene (from copper) on 300 nm SiO₂ synthesized under different growth pressure (shown in table 1) using Cu as catalyst at the same methane gas compositions and growth temperature: (a)S1; (b)S2; (c)S3; (d)S4; (e)S5. Excitation: 514 nm.....75

Figure 3.6 (a) Raman spectra indicating single layer graphene grown on copper foil by CVD process using the same conditions as S5. Excitation laser: 514 nm. Inset is the optical image of monolayer graphene on Si substrate with 300nm SiO₂. (b) Optical transmittance of layer by layer transferred graphene films on quartz substrates.....76

Figure 3.7 The effect of highly concentrated HNO₃ on the sheet resistance and surface energy of graphene films with different number of layers. (a) Sheet resistance R_s of graphene films before and after HNO₃ treatment. (b) Contact angle of graphene films before and after HNO₃ treatment.....78

Figure 3.8 (a) Schematic of organic solar cell with four-layer graphene films as transparent and conductive electrode. (b) Energy diagram of the solar cell device with structure: graphene/PEDOT:PSS/P3HT:PCBM/LiF/Al. (c) I-V characteristic of four-layer graphene film based organic solar cell. Inset is the I-V characteristic of organic solar cell using ITO as electrode.....80

Figure 4.1 (a) Optical micrograph of PGN grown over copper foil. (b) Optical micrograph of PGN film floating in the aqueous $\text{Fe}(\text{NO}_3)_3$ solution. (c) Top-view SEM image of PGN film. Inset is the top-view high magnification SEM of PGN (scale bar: 10nm). (d) 45° side-view SEM image of PGN film. (e) Two probe and four probe I-V characteristic of PGN film. Sheet resistance: $R_s = (\pi / \ln 2) \times (V_{diff} / I_{ds})$. (f) Sheet resistance change of PGN film transferred on PET substrate under various bending radius. Inset shows the bending experiment setup.....88

Figure 4.2 (a) Optical micrograph of micropatterned large-area PGN grown at 750°C for 5min. (b) SEM micrograph of PGN showing highly aligned CNT pillars on graphene film. (c, d) Optical micrographs micropatterned PGN in (a), transferred on quartz and SiO_2/Si , respectively.....90

Figure 4.3 (a) Raman spectra of few-layer graphene region. (b) Raman spectra of PGN film from CNT pillars region. The excitation laser: 532 nm.....91

Figure 4.4 (a) Low magnification TEM micrograph of micropatterned large-area PGN suspended on lacey carbon supported TEM Cu grid. (b) TEM micrograph of PGN (bottom view) showing crystalline integrity of individual CNT's root (dashed circles) with the surface of the graphene film. HRTEM micrographs of suspended PGN taken from (b), showing individual CNT's root (c) and tip (d) regions.....93

Figure 4.5 (a) Contact angle of PGN film before acid treatment. (b) Contact angle PGN film after acid treatment. Insets in a) and b) are the comparison optical micrographs of PGN films before and after acid treatment. (c) Schematic of test cell assembly. (d) CV curves of supercapacitor based on PGN films without and with acid treatment. The scanning rate is 100mV/s. The weight of one PGN film is 90ug/cm².....95

Figure 4.6 (a) comparison CV curves of capacitors based on copper foils, graphene layers on copper foils and PGN films on copper foils. Scanning rate: 100mV/s. inset is the zoom-in CV curves of capacitors based on copper foils and graphene layers on copper

foils. (b) CV curves of supercapacitor based on PGN films at scanning rate of 100mV/s and 200mV/s.....97

Figure 5.1 (a) SEM image of a CVD grown graphene layer on a SiO₂/Si substrate. The Inset AFM phase image shows the ripples formed on the graphene surface. (b) SEM image of ZnO nanostructures grown on the same CVD-graphene film at 450°C. The bright boundary regions indicate the enhanced growth of ZnO nanostructures. (c) I_{ds} –V_{ds} characteristics of CVD graphene layers before and after the synthesis of ZnO nanostructures. The inset is the four probe device structures before and after synthesis of the ZnO nanostructures. (d) I_{ds}-V_{gs} characteristics of CVD graphene layer before the growth of ZnO nanostructures. The inset shows the metallic behavior of ZnO-graphene heterogeneous nanostructures.....106

Figure 5.2 (a) Low magnification SEM image of ZnO nanostructures grown on CVD-graphene layer. (b) EDS pattern of ZnO nanostructures on graphene/SiO₂/Si.....107

Figure 5.3 SEM images of ZnO nanostructures grown on CVD-graphene layers. (a) At 450°C, the formation of fine ZnO nanorods is observed; (b) coarser nanorods are observed at the 550°C growth temperature; (c) ZnO nanoneedles are grown at 650°C..109

Figure 5.4 SEM images of ZnO nanostructures grown on a graphene layer at 550°C using 60nm gold catalyst nanoparticles. (a) SEM image of entangled long and dense nanowires floating over a layer of short hexagonal cone-shaped nanorods. Inset provides a higher magnification micrograph. (b) SEM image showing the interface between the long nanowires and short nanorods. (c) SEM image showing the gold catalyst nanoparticles and nanowires 20nm and 80 nm in diameter.....109

Figure 5.5 XRD pattern of ZnO nanostructures on graphene/SiO₂/Si substrate.....110

Figure 5.6 (a) Optical transmittance of CVD graphene film with an average thickness of 2.5nm on a quartz plate, before and after the growth of ZnO nanostructures. (b) Photoluminescence spectrum of ZnO nanostructures grown on a graphene layer. The inset is the UV absorption spectrum of a CVD-graphene layer with an average thickness of 2.5 nm on a quartz plate before and after growth of ZnO nanostructures.....112

Figure 5.7 (a) Optical image of FLG film transferred on Si substrate with 300nm SiO₂. The inset shows UV-vis spectrum of few layer graphene transferred on quartz substrate.

(b) Raman spectrum of FLG film. Raman excitation: 514nm. (c) Top-view SEM image of ZnO nanowires grown on top of CVD graphene at low magnification. Inset is high magnification SEM image of ZnO nanowires grown on graphene. (d) Top view of graphene/ZnO/graphene heterostructure at low magnification. The right-up inset is high magnification SEM image of graphene/ZnO/graphene heterostructure. Left-down inset is the EDS spectrum of graphene/ZnO/graphene heterostructure.....114

Figure 5.8 (a) Schematic of graphene/ZnO graphene device with Ni/Au contacts on graphene. (b) Energy band profile of metallic graphene and semiconducting ZnO nanowires. The arrows indicate the possible shifts of work function of graphene and the Fermi level of ZnO depending on the doping level. (c) Energy band diagram of graphene and ZnO nanowires junction when $\Phi_{\text{ZnO}} > \Phi_{\text{graphene}}$ (Ohmic contact). (d) A I-V characteristic of graphene/ZnO NWs/graphene device showing linear behavior. Inset is the non-linear I-V curve. (e) Energy band diagram of graphene and ZnO nanowires junction when $\Phi_{\text{ZnO}} < \Phi_{\text{graphene}}$ (Schottky contact). (f) I-V characteristic of graphene/ZnO NWs/graphene device showing Schottky behavior. Inset is enlarged I-V curve as voltage from -0.1V to 0.1V.....117

Figure 5.9 I-V curve of graphene/ZnO/graphene device at various temperatures. Inset is the logarithm of the current at 1.0V via the reciprocal temperature.....119

Figure 5.10 Photoconductivity of graphene/ZnO/graphene heterostructure device. (a) I-V characteristic of devices with linear I-V behavior in dark (black) and under 365nm UV illumination (red). (b) I-V characteristic of devices with non-linear I-V behavior in dark (black) and under 365nm UV illumination. (c) Normalized conductance (G/G_0) versus time as the UV illumination is switched on and off. G_0 is the initial conductance.....120

List of Tables

Table 1 Graphene samples synthesized using copper foil at various pressures under constant growth temperature and constant gas composition.....	73
--	----

Chapter 1 Introduction

1.1 Graphene

1.1.1 History of Graphene

Graphene, a single layer of carbon packed in honeycomb lattice with carbon-carbon distance of 1.42 angstrom, has drawn appreciable attentions from researchers due to its exceptional properties like high mobility[1], ballistic transport[2], high thermal conductivity[3], optical transmittance[4] and mechanical hardness[5]. The term firstly appeared in 1987 by Mouras et. to refer to the single sheet of graphite within the graphite intercalation compounds[6]. It is also used to describe 1D carbon nanotubes[7] and 3D epitaxial graphite[8]. While, the concept of graphene can be dated back to 1947 when P.R. Wallace firstly theoretically explored it[9]. In 1984 Mele, E.J. et. pointed out the emergent massless Dirac equation to describe the electrons around the Fermi level[10]. However, before Geim's group observed the single atomic layer graphene in 2004[11], the theorists such as Landau (1937) and Peierls (1935) argued that the true 2D crystal could not exist because it was thermodynamically unstable and the atomic monolayer tended to roll or fold in order to achieve the lowest potential energy state. Later research discovered that the reason why the atomic layer graphene could be observed was the existing of the intrinsic ripple[12], which is believed to prevent graphene from rolling and to help suppress the thermal fluctuation.

Starting from 1970s the researchers have tried different methods to achieve very thin films of graphite like epitaxial growth[13, 14], chemical exfoliation[15, 16] and mechanical exfoliation. However, Novoselov et al. was accredited for discovering

graphene in 2004 when they extracted single-atomic-thick crystallites from HOPG by mechanical exfoliation method using ‘Scotch tape’. Since then, significant scientific advance has been made in graphene[17, 18].

1.1.2 Graphene Crystal and Band Structures

The dimensionality is one of the most important parameters that define the material. Taking carbon for example, there are various structural forms of carbon like zero-dimensional buckminsterfullerene observed in 1985[19], 1D carbon nanotubes discovered in 1991[20], 2D graphene isolated in 2004[11] and 3D graphite/ diamond (shown in figure 1.1). These various structural forms give the carbon unique variety of properties and applications.

Graphene is an allotrope of carbon, composed by single-atomic layer of sp^2 -bond carbon atoms which are closely and strongly packed in honeycomb crystal structure. Graphene is 2D building material that can be wrapped to 0D buckminsterfullerene, rolled into 1D carbon nanotube and stacked to graphite (see figure 1.2). In forming the graphite’s layer graphene layer shows thickness of 0.34 nm.

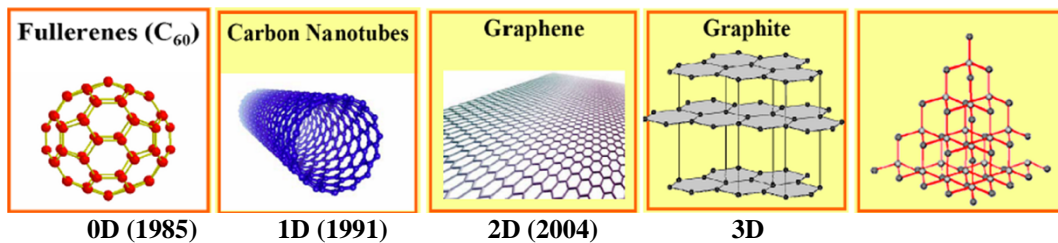


Figure 1.1 Various structural forms of carbon from zero to three-dimensions. From <http://www.physics.drexel.edu/~gyang/SOLID/lecture113010>

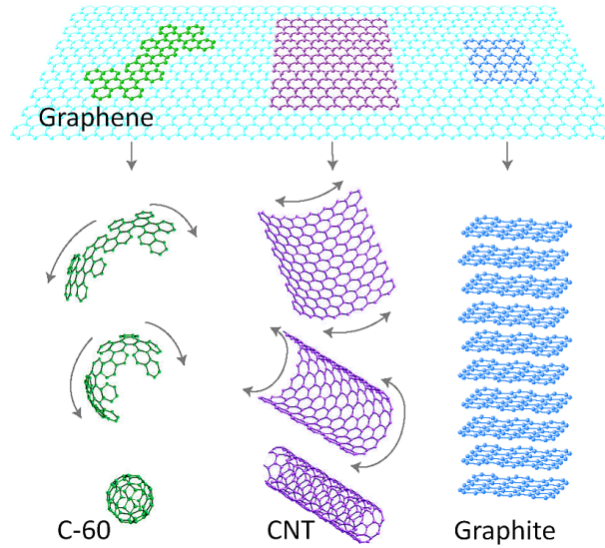


Figure 1.2 Graphene is 2D building material that can be wrapped to 0D buckminsterfullerene, rolled into 1D carbon nanotube and stacked to graphite. [1]

In the graphene structure, sp^2 hybridizations form σ and σ^* states which show high energy gap (14.26eV). Figure 1.3 shows the electron orbitals in graphene. These sp^2 hybridization orbitals closely pack the carbons on the x-y plane, but do not contribute to the electronic transport. The remaining $2p$ orbital takes place in p_z states which mix each other to form π bond. Therefore, in an finite graphene sheet p_z electrons are contributing one conducting electron per carbon and responsible for the weak van der Waals force between graphene layers in graphite[21].

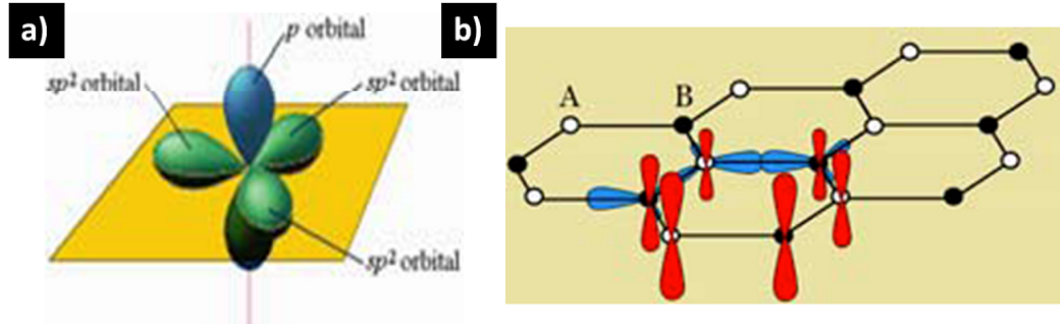


Figure 1.3 (a) Electron orbitals in graphite. (b) Electron orbital of graphene: sp^2 hybridized orbital responsible for the bonding on x-y plan; $2p$ orbital perpendicular to the x-y plan. From: <http://www.physics.drexel.edu/~gyang/SOLID/lecture113010>.

Figure 1.4a shows the graphene hexagonal lattice with bond length $d_{cc} = 1.42 \text{ \AA}$, two carbon atoms are in one unit cell with lattice constant $a = \sqrt{3}d_{cc} = 2.46 \text{ \AA}$. a_1 and a_2 are the unit vectors of the unit cell. $a_1 = (\frac{a}{2}, \frac{\sqrt{3}a}{2})$, $a_2 = (-\frac{a}{2}, \frac{\sqrt{3}a}{2})$. Figure 1.4b is the reciprocal lattice of graphene with lattice constant b . The unit vectors of unit cell are indicated with b_1 and b_2 , $b_1 = (\frac{\sqrt{3}b}{2}, \frac{b}{2})$, $b_2 = (-\frac{\sqrt{3}b}{2}, \frac{b}{2})$.

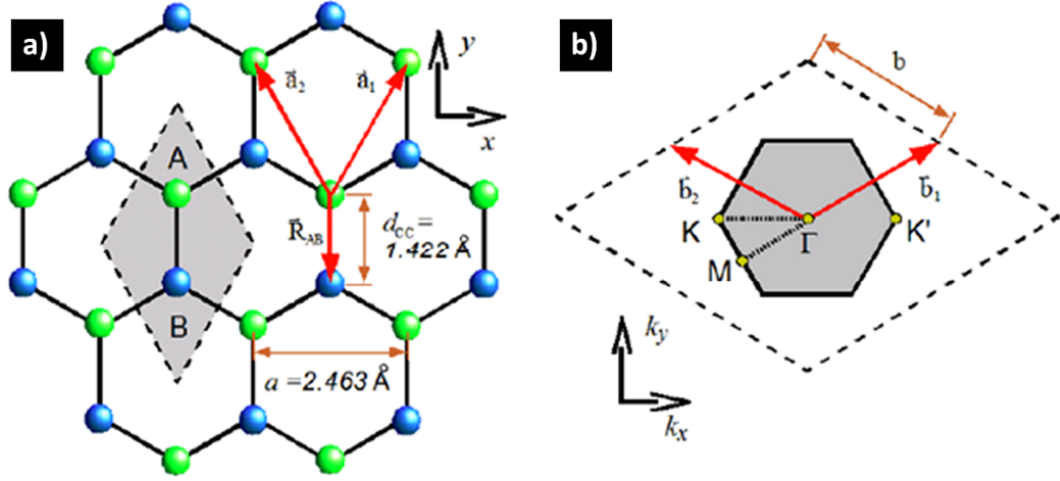


Figure 1.4 (a) Direct lattice of graphene. Shaded area is the primitive unit cell. (b) Reciprocal lattice of graphene. Shaded area is the first Brillouin Zone defined by the vector b_1 and b_2 . From: <http://www.physics.drexel.edu/~gyang/SOLID/lecture113010>.

Band structure of graphene around the Fermi level is determined by the p_z orbital. In 1991 Michenaud, J.C. and Michenaud J.P. used tight binding Hamiltonian including only p_z states to approximate the low energy electronic property[22]. Considering the interaction between neighbor p_z wave functions, the electronic structure of graphene can be approximated with the following expression:

$$E(k_x, k_y) = \pm \gamma \sqrt{1 + 4 \cos\left(\frac{\sqrt{3}k_x a}{2}\right) \cos\left(\frac{k_y a}{2}\right) + 4 \cos^2\left(\frac{k_y a}{2}\right)} \quad (1.1)$$

Figure 1.5b is extracted from the equation 1.1. The Fermi surface is characterized by six double cones. Near the Fermi lever, the low-E quasiparticles can be described by the Dirac-like Hamiltonian:

$$\hat{H} = \hbar v_F \begin{pmatrix} 0 & k_x - ik_y \\ k_x + ik_y & 0 \end{pmatrix} = \hbar v_F \boldsymbol{\sigma} \cdot \boldsymbol{\kappa} \quad (1.2)$$

Near the Fermi level the energy is linear dispersion of wave vector, so we can derive

$\left(\frac{d^2 E}{d\kappa^2} \right) = \infty$. Therefore, the electron effective mass expressed in

$$m^* = \hbar^2 \left(\frac{d^2 E}{d\kappa^2} \right)^{-1} \quad (1.3)$$

will be zero. It indicates that at the Fermi level, the electrons behave as zero-effective - mass Dirac fermions. This unique band structure illustrates the unique electrical property.

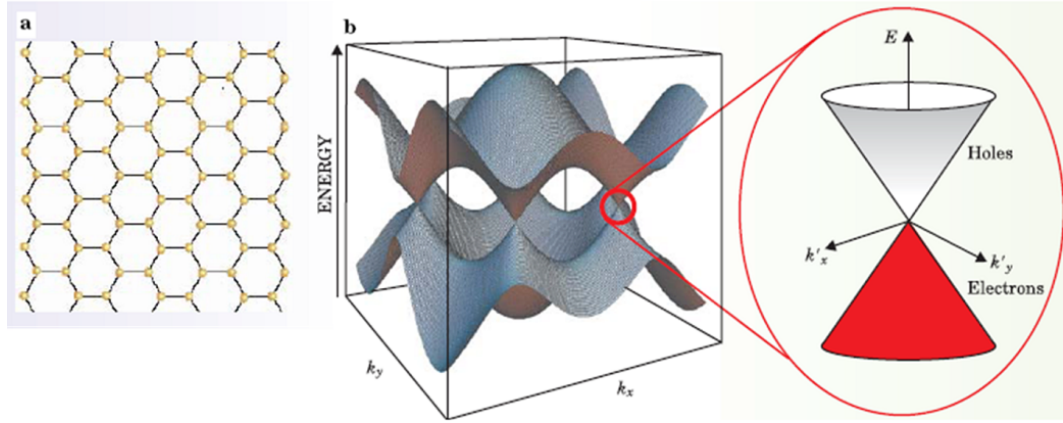


Figure 1.5 (a) Crystal structure of graphene. (b) Band structure of graphene. The right zoom-in is conical energy band spectrum associated with sublattices intersected at zero E near the edge of Brillouine zone.

1.1.3 Properties and Applications of Graphene

1.1.3.1 Field Effect Transistor and Integrate Circuits

In the past fifty years, Moore's law plays important role in the gigantic semiconducting industry: the typical dimensions of MOSFET (Metal Oxide Semiconductor Field Effect Transistor) on the integrated circuits decrease in size by a factor of two roughly every eighteen months. In 2006 Intel has achieved 65 nm technology node for dual-core and continued to push to 45nm even 22nm Silicon based MOSFET technology. As the gate length of MOSFET shrinks the number of integrated transistor dramatic increase (see figure 1.6). However, after 1990s the further size reduction causes significant negative impact in the performance of devices, not to mention the exponential increased fabrication cost. The problems caused by the short channel effect include leakage current, uncontrollably increased heat, statistical fluctuations in the channel resistance, electromigration in the channel and so on.

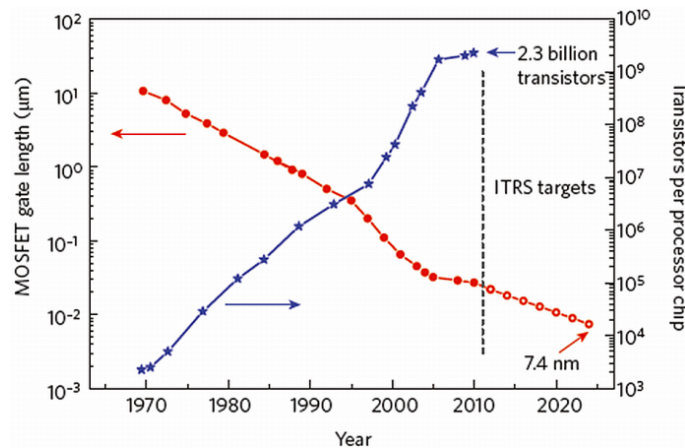


Figure 1.6 Evolution of MOSFET gate length in integrated circuits (filled red circle) and International Technology Roadmap for semiconductor targets (open red circle). The number of transistor per processor is indicated with blue stars. [23]

These problems inspire the scientists and engineers to investigate the alternative channel material. And the semiconducting nanowires[24, 25] and carbon nanotube[26, 27] have drawn much attention. But common problem existing so far is alignment of these nanowires and nanotubes. Graphene has high electron mobility ($2 \times 10^5 \text{ cm}^2 \text{ V}^{-1} \text{ s}^{-1}$) [28], low electrical noise[29], high thermal conductivity ($5.30 \pm 0.48 \times 10^3 \text{ W m}^{-1} \text{ K}^{-1}$) [3], and high cut-off frequency (up to 100GHz) [30]. More importantly it is compatible to current CMOS technology. All of these make graphene the promising candidate for channel material for the next-generation MOSFET. Facing the fact that at the state of art large-area graphene transistors still show low on-off ratio (in the range of 2-20) caused by the zero-bandgap for large-area graphene researchers are trying different approaches to improve it. One of the approaches to introduce energy bandgap is to create the graphene nanoribbons. And up to 10^6 on-off ratio has been achieved in 5 nm graphene nanoribbons[31, 32]. Although the carrier mobility in graphene nanoribbons could be decreased, from the experiment and simulation the mobility can still maintain satisfactory value to meet the industrial applications (shown in figure 1.7).

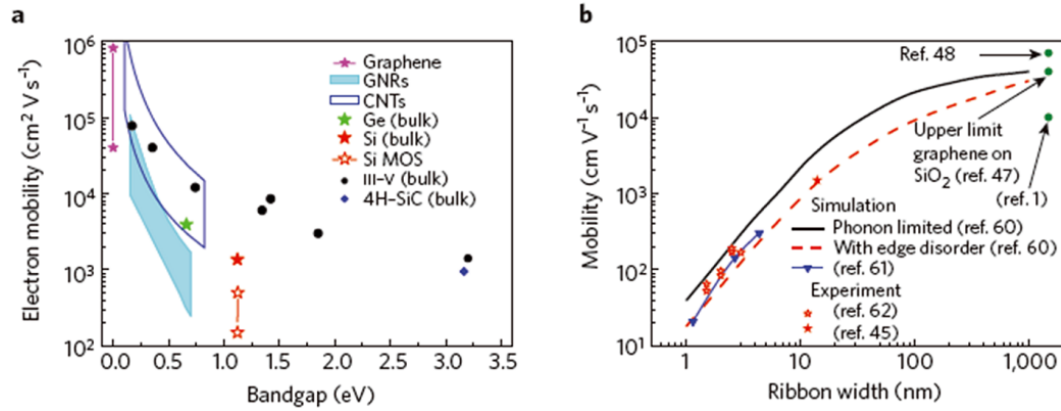


Figure 1.7 (a) Electron mobility versus bandgap engineering in low electrical fields for different materials. (b) Carrier mobility versus graphene nanoribbon width from simulation and experiment. [23]

1.1.3.2 Graphene Based Chemical and Bio Sensors

Another promising application for graphene is gas/bio sensors. In the sensing process, all of the carbon atoms are exposed to the analytic subjects because of the 2D graphene, and high conductive graphene has low Johnson noise. These properties make the graphene ultra sensitive to the external molecules. The sensitivity can reach single atomic or molecular level (see figure 1.8)[33]. Since the firstly reported graphene based gas sensor towards NO_2 , NH_3 , HO_2 and CO by Shedin et al. in 2007[33], there have been a number of theoretical[34-36] and experimental[33, 37-41] studies that investigated the gas sensing properties of mechanically exfoliated, chemically derived graphene and graphene oxide layers. Fowler et al.[40] demonstrated the graphene chemical sensor to detect dinitrotoulene (shown in figure 1.9).

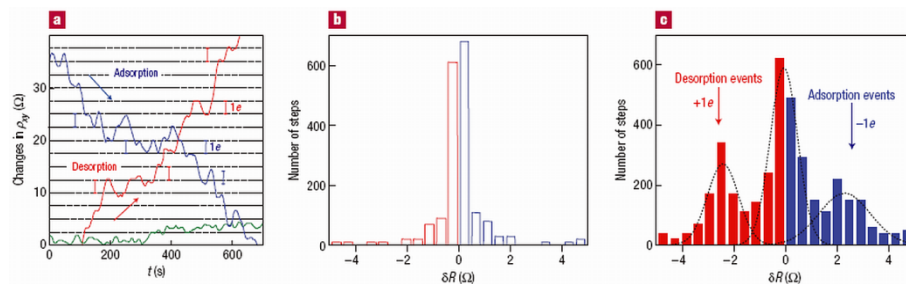


Figure 1.8 Single molecule detection based on graphene field effect transistor.[33]

The important fact is that graphene sensing properties are fully recoverable either by thermal annealing[33] or by the UV illumination for short time[37, 42]. Also, the mechanism of the gas or chemical sensing properties of graphene was also investigated[34-36]. That is attributed to the charge transfer between graphene and the absorbed gas or chemical molecules. The decoration of graphene surface with some metal nanoparticles like Pd was also employed to improve the respond to H_2 detection[38].

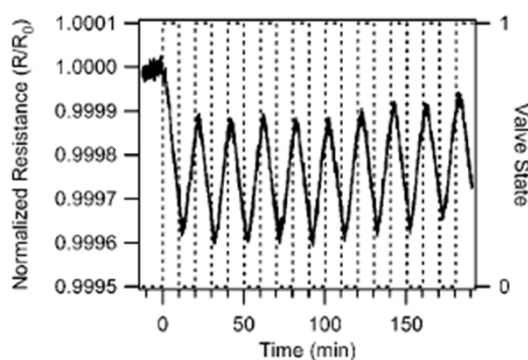


Figure 1.9 Response of the graphene sensor to 2,4 dinitrotoluene. [40]

In addition to the gas sensing, graphene biosensor has been widely explored. Mohanty et al. applied graphene oxide for sensing DNA and studied the interface of bacterial and graphene oxide[43]. The shift of Dirac point was explained by the negative charge gating effect of DNA. Further Lin et al. verified this effect by Raman spectroscopy and deeply understood the mechanism by theoretical modeling[44]. Recently, Shan et al. reported glucose sensor by constructing a novel polyvinylpyrrolidone protected graphene/polyethylenimine/glucose oxidase (GOD) devices. Up to 14mM glucose can be detected in their devices[45]. Alwarappan et al. demonstrated the graphene sensing properties toward catecholamine neurotransmitters[46]. Overall, as the further research is done in the graphene, graphene will show more promising applications in the gas or bio sensing fields.

1.1.3.3 Transparent and Conductive Electrode

Generally researchers use transparent and conductive metal oxides such as indium tin oxide (ITO) or fluorine tin oxide (FTO) optoelectronics. A major disadvantage of ITO is its high cost due to Indium being a rare element. Also the ITO shows instability in presence of acid as well as the limited optical transmittance in the near or infrared region. Graphene, a monolayer two-dimensional atomic carbon sheet, has attracted great attention because of its unique electrical and optical properties. Figure 1.10 shows that the transmittance of graphene reaches over 90% in the visible range dependent on the number of layers[4]. The low sheet resistance and high optical transmittance make graphene the good substitute of ITO as transparent electrode for optoelectronic

devices[47-49]. In 2008, Wang et al. firstly reported the fabrication of dye-sensitized solar cell based on graphene transparent electrodes[49]. The thermally reduced graphene oxide films with over 70% transmittance had good conductivity over 550S/cm. The power conversion efficiency (PCE) was around 0.26% (shown in figure 1.11).

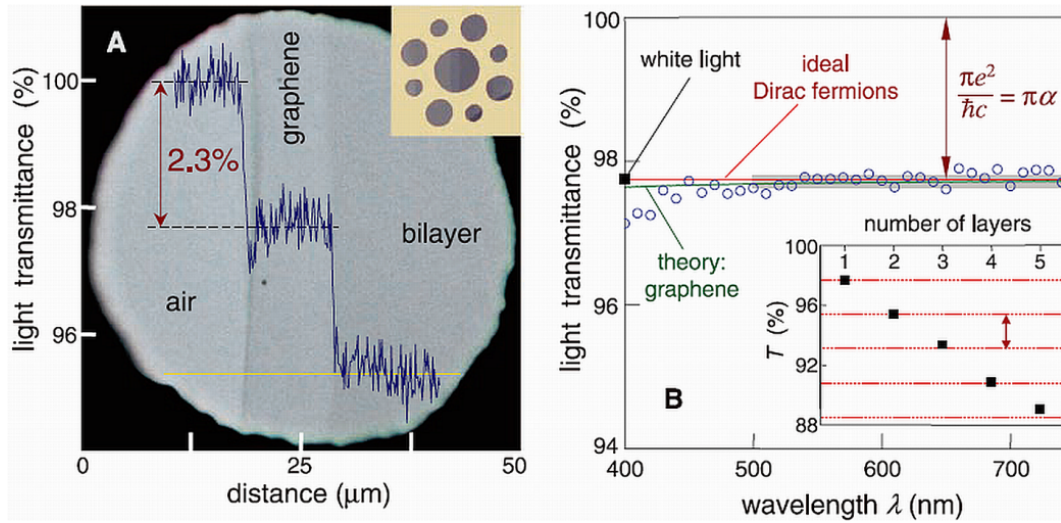


Figure 1.10 (A) Photograph of 50um aperture covered by graphene and its bilayer. (B) Transmittance spectrum of single-layer graphene. (Inset) Transmittance of white light as function of number of graphene layers. [4]

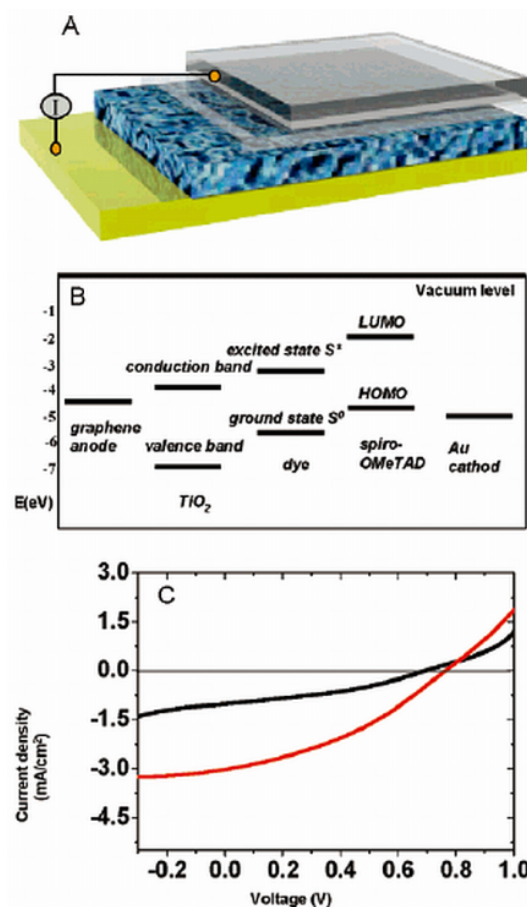


Figure 1.11 (A) Schematic of dye-sensitized solar cell using graphene film as electrode. (B) The energy diagram of dye-sensitized solar cell. (C) I-V curve of graphene (black) and FTO based solar cell. [49]

Also Blake et al. demonstrated graphene based liquid crystal device in 2008[48]. However the graphene films still showed high sheet resistance of 5k ohm/sqr at 90% optical transmittance. After 2009 the advancement of chemical vapor deposition method of growing large-area and continuous graphene films has greatly promoted these research fields[47, 50-54]. In 2009 Kim et al. reported the few layer graphene from Nickel by chemical vapor deposition (CVD) with sheet resistance of 280 ohm/sqr at 80%

transmittance[52]. Later Li et al. demonstrated high quality 95% single layer graphene grown on copper foil[53]. Further different transferred method (roll to roll) was employed by Bae et al. to lower the sheet resistance of 30-inch graphene films for the transparent electrodes in touch screen (see figure 1.12)[51]. What was more, these CVD grown graphene films showed excellent mechanical properties which made them promising candidates as stretchable electrodes. For the application of graphene in the solar cell researchers tried to functionalized the graphene surface either to change the work function or increase the conductivity[55]. And Wang et al. employed functional group PBASE to make the graphene surface hydrophilic thus increased the power convert efficiency (PCE) of organic solar cell[47]. Overall, graphene as transparent electrode will be most promisingly commercialized in near few years. Farther improvement in quality and mass production to decrease the cost will be research direction. For the application in organic solar cell graphene surface functionalization needs to be employed to improve the PCE of photovoltaic cells.

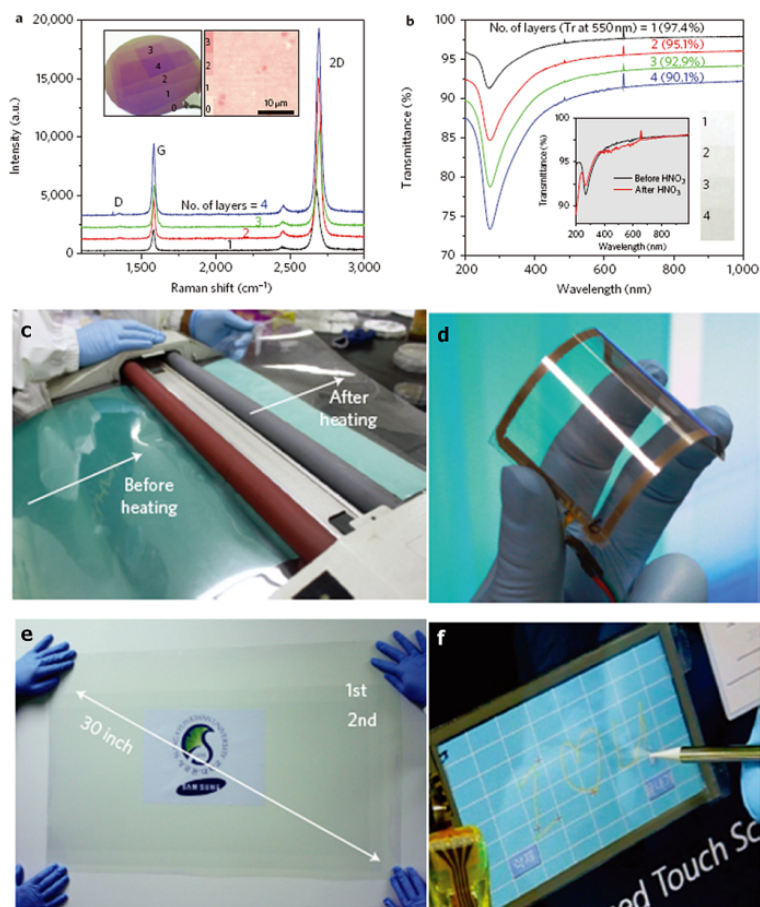


Figure 1.12 (a) Raman spectra of graphene films with different number of stacked layers. (b) UV-vis spectra of layer-by-layer transferred graphene films on quartz substrate. (c) Roll-to-roll transfer of graphene film from thermal release tape to PET film at 120 °C. (d) An assembled graphene/PET touch panel showing outstanding flexibility. (e) A transparent graphene film transferred on a 35-inch PET sheet. (f) A graphene-based touch screen panel connected to computer with control software.[51]

1.1.3.4 Supercapacitor

Ultra or supercapacitor based on electrochemical double layer capacitance (EDLC), consisting of the porous electrodes in the electrolyte solution that store or release the energy among the electrode/electrolyte interface, has been widely explored in the past 30

years[56]. The supercapacitor can be widely applied in energy capture like load cranes, forklifts, electric vehicles and power absorb/release at short time. However, energy density of supercapacitor is still significantly lower than the battery or fuel cell. Thus, increasing the energy density of supercapacitor to be close to that of battery, as stated by U.S. Department of Energy, is a strong interest to researchers. One of approach to increase the performance of supercapacitor is to tackle with electrode material. Among the carbonaceous material, graphene having high electrical conductivity and high specific surface area, was demonstrated as promising electrode material for supercapacitor[57]. In 2008, Stoller et al. fabricated double layer supercapacitor based on chemically modified graphene and achieved specific capacitance 135 F/g and 99 F/g in aqueous and organic electrolyte respectively[57]. The schematic of the fabricated supercapacitor is shown in figure 1.13. Later on a few groups developed similar supercapacitor based on chemically reduced graphene oxide or liquid exfoliated graphene[58-61]. Liu et al. demonstrated graphene based supercapacitor with ultrahigh energy density. The reported value was as high as 85.6 Wh/kg at room temperature and 136 Wh/kg at 80 degree using ionic liquid as electrolyte[62]. All of these graphene based supercapacitor were utilizing the basal planar carbons to store the energy, which had relatively lower specific capacitance (3 uF/cm^2) compared with edge orientations of graphene ($50\text{-}70 \text{ uF/cm}^2$)[63]. Recently, new material synthesis and device fabrication approaches have been employed to utilize the edge orientation to improve the performance of graphene based supercapacitor[64, 65]. Miller et al. demonstrated supercapacitor with electrodes made from vertically aligned graphene nanosheets grown directly from metal current collectors.

By fully utilizing the edge orientations of graphene they demonstrated that the fabricated supercapacitor has high capacitance (above 175 uF/cm^2)[64]. Yoo et al. employed original “in-plane” fabrication approach to sufficiently utilize the basal plane and edge orientations, thus increased the capacitance of graphene. They achieved specific capacitance as high as 80 uF/cm^2 for CVD grown 1-2 graphene layers and 394 uF/cm^2 for reduced graphene oxide electrodes[65].

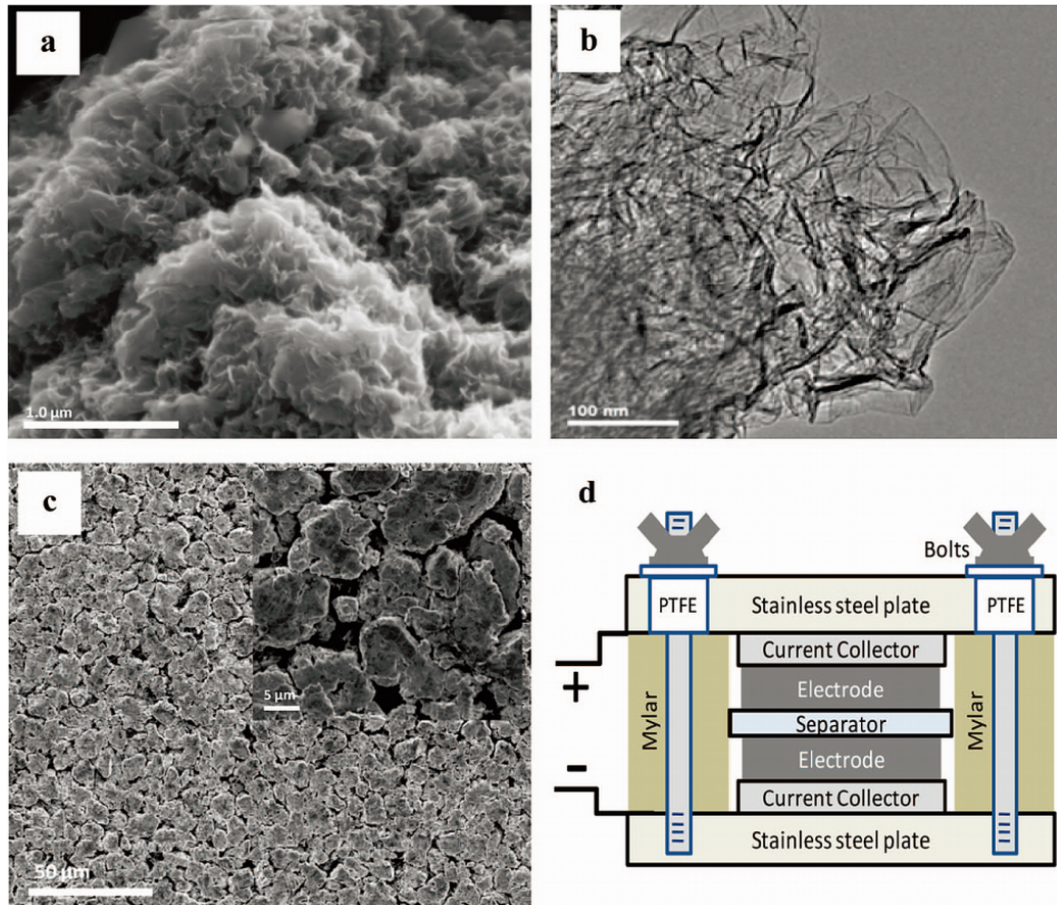


Figure 1.13 (a) SEM image of graphene particles. (b) TEM image showing individual graphene sheets. (c) Low and high magnification SEM image of graphene electrode. (d) Schematic of test cell. [57]

1.2 Synthesis of Graphene

The earliest trial of synthesizing monolayer graphite can track back to 1975[13], when B. Lang formed monolayer or few layer graphene through thermal decomposition of ethylene on Pt surface. However, at that time the unique properties and potential application had not been extensively explored, thus it did not intrigue much attention from the researchers[66]. After 20 years, a few trials from Japan had been reported in producing graphene through thermal decomposition[67, 68] or exfoliation[16]. However, Novoselov et al. was accredited for discovering graphene in 2004 when they extracted single-atomic-thick crystallites from HOPG by mechanical exfoliation method using ‘Scotch tape’. They showed repeatable method of producing the single layer graphene and extensively explored the physical[4, 11, 17, 69] and chemical properties[33]. Since then, various approaches such as exfoliation, thermal decomposition, and chemical vapor deposition have been employed to produce graphene. Some of the main routes are categorized in the following sections.

1.2.1 Exfoliation and Cleavage

Graphite is stacked from graphene layers through weak Van der Waals force. In principle, single layer graphene can be exfoliated or cleaved by mechanical or chemical energy. In 2001, the pioneer work was done by Shioyama who produced graphene from graphite through expansion of potassium-graphite intercalation compound (GIC) by introducing unsaturated hydrocarbon into the interlayer of potassium-GIC[16]. The other important work was done by Viculis et al., who used potassium to intercalate into the

graphite layers and exfoliated in ethanol by sonication[70]. Also, mechanical exfoliation was employed to get ultra thin graphite film. However, until 2004 Geim's group reported the successful exfoliation of single layer graphene. Their major approach was to transfer the graphene layers onto 300 nm SiO₂ substrate so that they could efficiently identify the number of graphene layers by optical microscopy because of the high optical contrast between graphene and 300nm SiO₂. This approach was proved to be reliable and easy, thus attracted immediate attention from the science community[3, 71, 72].

Besides, another important catalog of exfoliation is chemical exfoliation in liquid phase. Stankovich et al. achieved partially reduced graphene oxide (GO) nanosheets by ultra-sonication of the graphite oxide flakes in aqueous suspension and then reduced the GO nanosheets in hydrazine hydrate[73, 74]. However, graphene oxide nanosheets were not fully reduced and had significant oxygen group left in the carbon structures. To overcome this drawback, another liquid exfoliation in organic solvent without oxidization of graphite was proposed by Hernandaz et al. in 2008[75]. This process showed the promise of large scale production of graphene layers with high quality. Similar process of producing single, few layer graphene was employed by Lotya et al. by dispersing the graphite in SDBS followed by ultro-sonication to get graphene[76]. Nevertheless, the exfoliated graphene is generally in micrometer scale, which limits its application in electronics.

1.2.2 Thermal Decomposition of SiC

One of the highly promising growth techniques is to synthesize graphene by thermal decomposition of SiC. What makes this approach attractive to researchers in the application of post-CMOS electronics is the discovery that even few-layer epitaxial graphene on SiC shows similar electronic properties to the isolated graphene sheet[77, 78]. The other advantage of epitaxial graphene is that the process is compatible with standard CMOS technology. Sprinkle et al. used standard CMOS technology to synthesize graphene nanoribbons by fabricating scalable templates, which advanced the research in graphene as the channel material in post-CMOS technology[79]. To go back to history, the pioneering work was done by Vanbommel et al. in 1975[80], while the major advance was promoted in recent years by several scientists, one of whom is de Heer[77, 78, 81]. He comprehensively reviewed the growth and electronic properties of epitaxial graphene on SiC[81]. Generally, the epitaxial graphene on SiC is synthesized under ultra high vacuum and at heating temperature between 1000 °C to 1500 °C for short time (1-20 minutes). These extra conditions limit the industrial application. Recently some significant developments were made to this process. Juang et al. synthesized the epitaxial graphene on SiC at low temperature (750 °C)[82]. And Emtsev et al. improved the process and produced the epitaxial graphene on SiC at ambient pressure[83]. These advances to the process on one hand could produce the wafer scale graphene; on the other hand it improved the process and made it more cost-effective to the industry.

Although huge advances have been made in this process, issues such as the uniformity in the thickness of graphene, repeated production of large-scale graphene need

to be solved. SiC has two polar sides perpendicular to c-axis. The bulk terminated SiC(0001)Si-terminated face (Si-face) has one dangling Si bond per Si atom, while the SiC(000-1) C-terminated face (C-face) has one C dangling bond per C atom[81]. Graphene, grown on these two polar planes, shows different growth behaviors and electronic properties. Further research has to be done to understand the mechanism and the graphene-SiC interface.

1.2.3 Chemical Vapor Deposition

Compared with the previous two methods chemical vapor deposition technique in synthesis of graphene has drawn much attention because it can produce wafer scale graphene in economical way. Generally speaking, CVD approach of synthesizing single layer or few layer graphene is to use eco-friendly precursor (CH_4 , C_2H_2) by thermally cracking of Carbon elements on metal catalysts like nickel, copper, Pt, Ru or Co either through precipitation process or surface catalyzed process. The first use of CVD techniques on the synthesis of planar few layer graphene on Pt crystal surface was reported by Lang in 1975[13]. However, the intense research effort were put into this field starting from 2006[84]. Somani et al. grew the graphene layers on Ni surface, and the number of layers was estimated to be 35 layers. This approach opened up a new path for graphene synthesis, although several issues like thickness control and uniformity had to be solved. Then nanometer thick (1-2 nm) graphene films grown on nickel foil (hundred micrometer) were achieved by several groups through CVD approach [85, 86]. Later on a few trials were made to synthesize the few-layer graphene (FLG) on thin film

polycrystalline nickel thin films (<500 nm)[52, 54]. The part of the results obtained from Kim et al. is shown in figure 1.14.

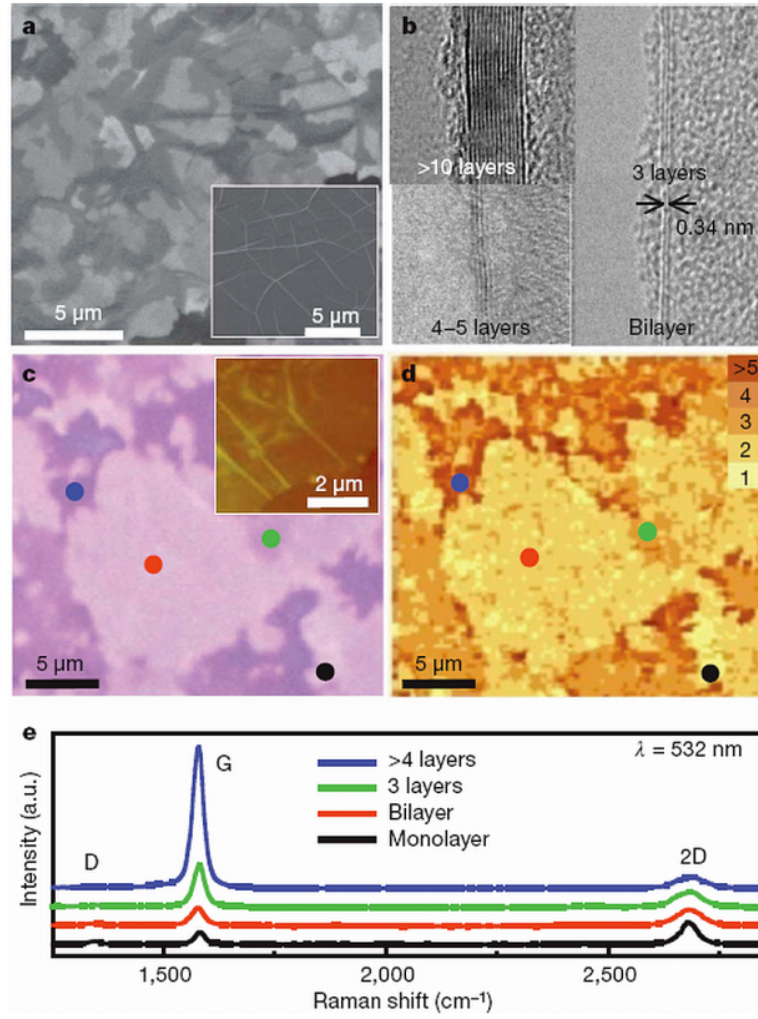


Figure 1.14 Various spectroscopic analyses of the large-scale graphene films grown by CVD. (a) SEM images of as-grown graphene films on thin (300-nm) nickel layers and thick (1-mm) Ni foils (inset). (b) TEM images of graphene films of different thicknesses. (c) An optical microscope image of the graphene film transferred to a 300-nm-thick silicon dioxide layer. The inset AFM image shows typical rippled structures. (d) A confocal scanning Raman image corresponding to c. The number of layers is estimated from the intensities, shapes and positions of the G-band and 2D-band peaks. (e) Raman spectra (532-nm laser wavelength) obtained from the corresponding coloured spots in c and d. a.u., arbitrary units.[52]

In the case of synthesizing graphene on nickel by CVD, carbon atoms cracked from precursor gas (CH_4 or C_2H_2) at high temperature ($900/1000^\circ\text{C}$) diffuse to the nickel and then segregate to form graphene film at fast/moderate cooling rate. This mechanism is called precipitation process. Therefore, in this process, the solubility of carbon atoms in nickel and cooling rate are critical for the high quality graphene[86]. In their process[52, 54], they used Nickel thin film rather than Nickel thick foil to minimize the solubility of carbon atoms in the nickel, and used the moderate and fast cooling rate to segregate C atoms to form graphene film. Other than nickel, a few metals like Co, Ru were employed to synthesize graphene[87-89], but controlling the uniformity of graphene layers in the large scale is still the challenge.

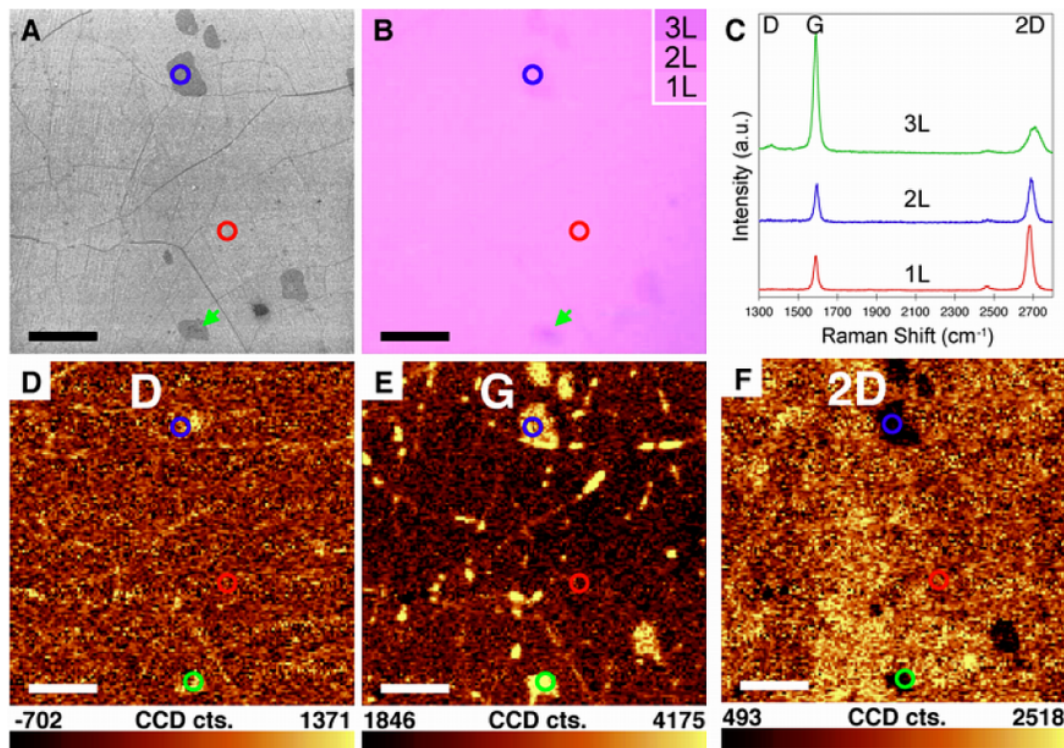


Figure 1.15 (A) SEM image of graphene transferred on SiO₂/Si (285nm thick oxide layer) showing wrinkles, and 2 and 3 layer regions. (B) Optical microscope image of the same regions as (A). (C) Raman spectra from the marked spots with corresponding colored circles or arrows showing the presence of graphene, 2 layers of graphene and 3 layers of graphene; (D, E, and F) Raman maps of the D (1300 to 1400 cm⁻¹), G(1560 to 1620 cm⁻¹), and 2D (2660 to 2700 cm⁻¹) bands, respectively (WITec alpha300, $\lambda_{\text{laser}} = 532$ nm, ~500 nm spot size, 100 objective). Scale bars are 5 μ m.[53]

In the further development of the process, Ruoff's group achieved graphene with high quality and uniformity in the large scale[53]. They claimed above 95% of the graphene film grown on copper foil was covered by the single layer region (see figure 1.15). The graphene film showed high electrical and optical properties. Other than the precipitation process, it was proposed to be surface catalyzed process on copper. Li et al. used carbon isotope labeling to prove this mechanism[90]. Based on this progress,

researchers synthesized the ultra large scale graphene film as transparent electrode for touch screen[51]. In the near future, researchers will focus on the solving the issues like controlling the uniformity and thickness of graphene in the wafer scale, improving the quality in term of electrical conductivity for the application in electronics and optoelectronics.

1.2.4 Other Methods

Another recent method of graphene or graphene nanoribbons synthesis was to use carbon nanotubes (CNT) as starting material. In 2009, three groups independently reported the similar results[91-93]. Tour's group unzipped the MWCNT by stepwise oxidization in KMnO_4 and H_2SO_4 , then reduced the opened graphene nanoribbons in NH_4OH and hydrazine in $\text{N}_2\text{H}_4\cdot\text{H}_2\text{O}$ solution, finally annealed in H_2 environment[91]. By this method they demonstrated 100% yield and graphene nanoribbons with high quality (shown in figure 1.16). Dai's group plasma etched the partially embedded CNT in polymer to get graphene nanoribbons[92]. In another study by Vega-Cantu et al., MWCNTs were opened longitudinally by using Li and ammonia intercalation followed by exfoliation in acid and rapid heating[93].

Besides, radio frequency PECVD was used to synthesize graphene flakes. The earliest reported graphene like carbon nanosheets synthesized by PECVD was found by Holloway's group in 2004[94, 95]. Since then, a lot of researcher around the world followed up the work. Employing this approach Holloway achieved vertically aligned graphene nanosheets which show AC filtering effect at 120 Hz in supercapacitor[64].

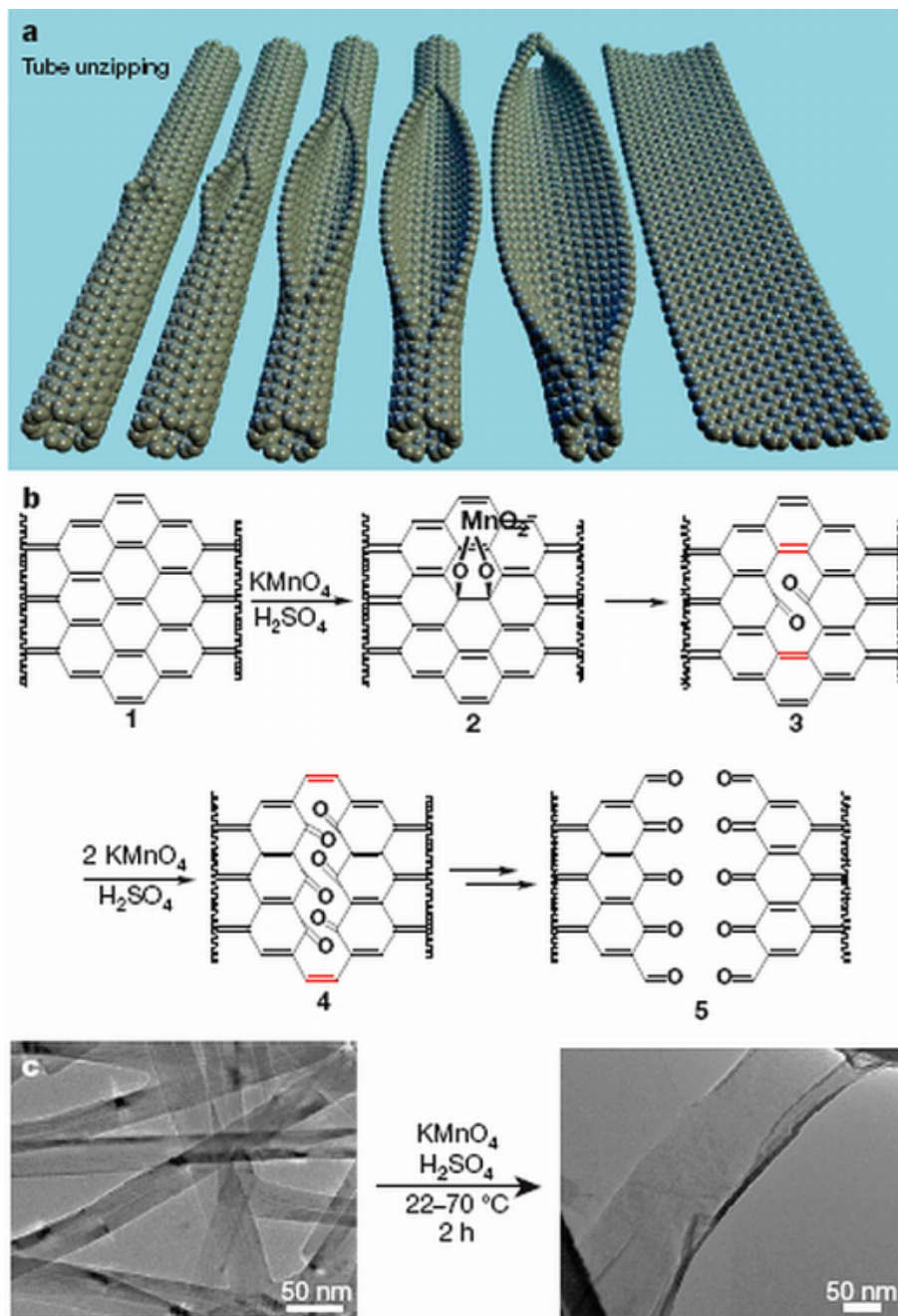


Figure 1.16 Nanoribbon formation and imaging. (a) Representation of the gradual unzipping of one wall of a carbon nanotube to form a nanoribbon. Oxygenated sites are not shown. (b) The proposed chemical mechanism of nanotube unzipping. The manganate ester in 2 could also be protonated. (c) TEM images depicting the transformation of MWCNTs (left) into oxidized nanoribbons (right). The right-hand side of the ribbon is partly folded onto itself. The dark structures are part of the carbon imaging grid. [91]

1.3 Graphene Hybrid Nanostructures: Synthesis and Applications

Despite the dramatic progress in the graphene research, another emerging research area is the graphene hybrid nanostructures through self-assembling graphene and other nanomaterials (carbon nanotubes, inorganic nanowires and nanoparticles, organic component) for various applications. Although there are various components involved in the graphene hybrid nanostructures, based on the role of graphene in the architectures of graphene hybrid nanostructures, they can be distributed into three types (shown in figure 1.17)[96]. In type I, The major role of graphene is to provide conductive or even transparent substrate for supporting the second active components assembled on top of graphene films. In type I, graphene film can be from reduced graphene oxide nanosheets or from continuous large-area graphene layers. The second components are usually inorganic nanostructures, for example, carbon nanotubes, nanowires or nanoparticles. The major applications for the type I are in the chemical sensing[97], catalyst[98], and energy conversion[99]/storage[100]. This is majorly attributed to the large surface areas obtained from graphene as well as the active functional inorganic nanostructures. The architecture of type II is that graphene and the components are mixed together to form continuous hybrid films in which graphene acts as equivalent role as the other component. The typical example is the graphene/CNT hybrid film via layer by layer assembly reported by Cai et al.[101]. The major benefit of the second type is the large surface interfacial areas which is promising for the application in energy storage[102], battery[103] or transparent electrode[104]. In type III, graphene, imbedded in the continuous matrix of the second component (usually polymer), plays the role of

improving the mechanical, electrical and thermal properties of the composites due to its high aspect ratio and excellent physical properties. The major application of this type of hybrid structure is to fabricate the conductive high-strength films[105, 106].

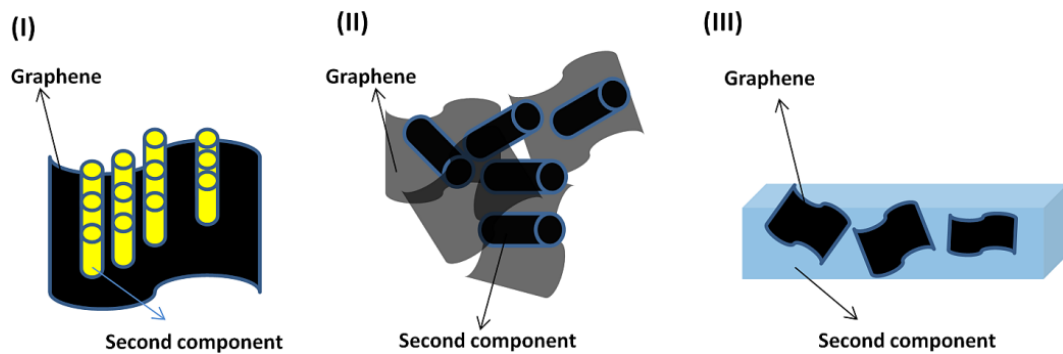


Figure 1.17 Schematic of three types of graphene hybrid nanostructures.

To review the synthesis of the graphene hybrid nanostructures, I will focus on the first type of graphene hybrid nanostructures which is the important subject of my thesis work. To synthesize the first type of graphene hybrid nanostructures there are two widely used approaches: layer by layer (LBL) self-assembly and in situ synthesis. In the LBL self-assembly, readily the graphene nanosheets with oxygenated groups which provide the negative charges in the aqueous solution are employed as the supporting substrates. Then the second component with positive charge can be attached to the negative charged graphene through self-assembly approach. Hong et al. employed electrostatic interaction of two oppositely charged components of graphene oxide nanosheets and MWCNTs to form graphene/CNT hybrid films by LBL self-assembly[107]. This method provided

excellent control in terms of performance in electrical conductivity. And multilayer of graphene/CNT hybrid films can be fabricated by LBL self-assembly. Also Kim et al. used similar approach to produce the graphene/CNT hybrid nanostructure as transparent electrode[108].

Another widely used method for the synthesizing type I graphene hybrid film is the in situ growth either through chemical synthesis or CVD synthesis. Metal nanoparticles like Au can be synthesized on the top of graphene oxide nanosheets film by immersing the graphene film into AuCl_3 solution to form graphene/nanoparticles hybrid film[109]. Sundaram et al. used electrochemical deposition of Pt nanoparticles on the graphene surface to enhance the sensitivity to Hydrogen[38]. Other than metal nanoparticles, some groups also synthesized the 1D ZnO nanowires on top of reduced graphene oxide nanosheets films by hydro-thermal method for the field emission application[110].

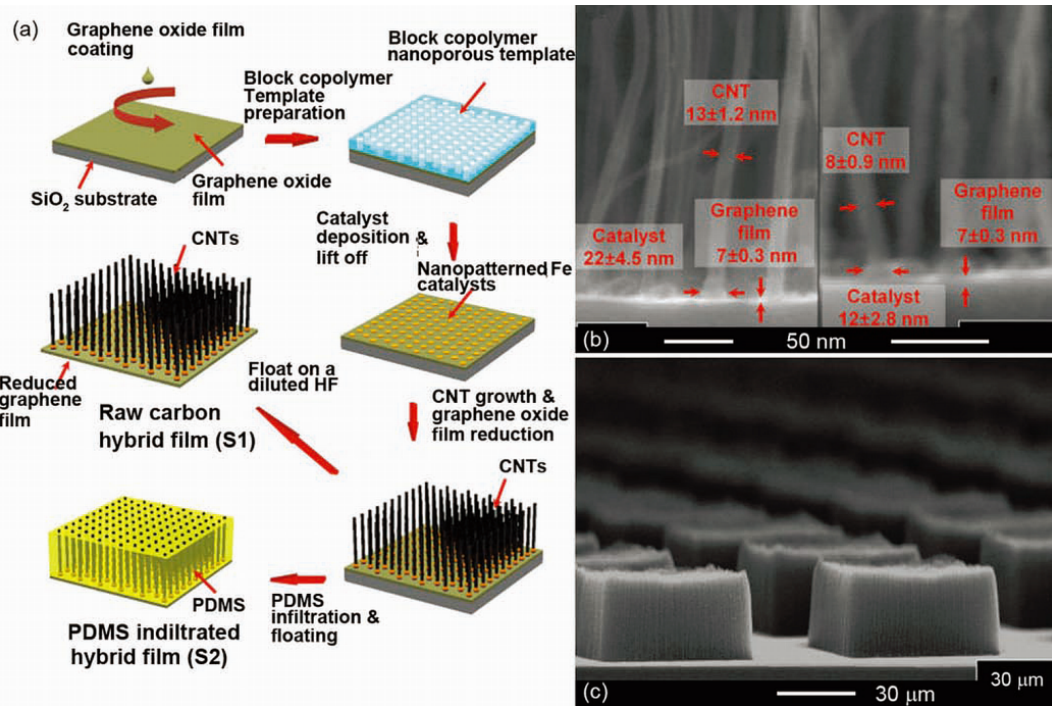


Figure 1.18 (a) Schematic illustration of the fabrication process for CCG/CNT composite films. (b) SEM image of cross section of CCG/CNT composite film prepared following the process illustrated in (b). (c) SEM image of pattern CNT on CCG film.[111]

In situ growth by CVD method is also an important one in synthesizing type I graphene hybrid nanostructures in a well controlled way, which is vertically orienting 1D nanotube or nanowire on top of graphene. Recently, Kim's group demonstrated carbon hybrid film composing vertically aligned CNTs on reduced graphene film for field emission application, as illustrated in figure 1.18[111]. Firstly, large area reduced graphene films with high electrical conductivity and transmittance were prepared by spin coating on transparent substrate, followed by Fe catalyst patterning on top of it through block copolymer lithography. n-type CNTs were vertically grown on top of the mechanically flexible reduced graphene films by PECVD approach. It exhibited excellent

electrical and mechanical properties. Also our group demonstrated in situ one-step synthesis of pillar graphene/CNT nanostructures on copper foil for the application in supercapacitor[100, 112]. Other than carbon nanotubes, in our group 1D ZnO nanostructures were successfully synthesized on CVD graphene film by two-step synthesis method[113]. It showed excellent electrical and optoelectronic properties and provided new path of application in optoelectronic devices.

1.4 Thesis Outline

This dissertation focuses on investigating synthesis of graphene and its hybrid nanostructures by CVD process as well as studying the potential applications in nanoelectronics and energy conversion/storage. The substantial understanding of interaction of graphene sheet with the bio-molecules and gas molecules will enable the capability of improving the applications of graphene in bio-sensor and chemical sensor. Synthesis of graphene by CVD process promotes the application of graphene as transparent electrode in photovoltaic cell. Novel synthesis of pillar graphene nanostructures provides potential use for energy conversion/storage, sensors and field emission. Studies on the heterogeneous graphene-ZnO nanostructures promote the understanding the interface between carbon and inorganic, provides another route of applying graphene as transparent electrode for energy conversion in future.

In chapter 2, graphene field effect transistors are fabricated to study the interaction of graphene with single stranded Deoxyribonucleic Acids (ssDNA) and gas molecules. ssDNA are found to act as negative potential gating agents that increase the hole density

in single layer graphene (SLG). Later, the molecular photodesorption and absorption from pristine and functionalized graphene are studied. The photodesorption induced current decrease in functionalized graphene by concentrated HNO_3 becomes less significant than pristine graphene layers. Our results provide a new strategy for stabilizing the electrical performance of CVD grown large-area graphene layers for applications ranging from nanoelectronics to optoelectronics.

Chapter 3 reports the synthesis of graphene on Ni thin film as well as on the Cu foils. It is found that the growth pressure is important growth kinetic on controlling the graphene uniformity and quality using Cu-catalyst. Sheet resistance of graphene thin film decreases by 30% using lay by lay transfer approach. Highly concentrated HNO_3 improves the conductivity and surface wettability of graphene layers. The fabricated organic solar cell based on graphene anode shows relatively low PCE compared with ITO-based photovoltaic cell. And two approaches of improving PCE of graphene-based solar cell are suggested.

The studies on the graphene hybrid nanostructures begin with chapter 4, which demonstrates the synthesis of pillar graphene nanostructures comprising vertically aligned MWCNTs on graphene by in situ one-step growth by CVD approach. Also the potential application of these unique graphene hybrid nanostructures in energy storage is investigated. It shows high specific capacitance and high energy density.

Chapter 5 demonstrates the synthesis and characterization of three dimensional heterostructures graphene nanostructures (HGN) comprising continuous large area graphene layers and ZnO nanostructures, fabricated via chemical vapor deposition. The

material characterization exhibits the highly crystalline ZnO nanostructures synthesized on few layer graphene CVD film. Also electronic devices from graphene/ZnO nanostructures/graphene show excellent electrical and photoelectrical properties. A combination of electrical and optical properties of graphene and ZnO building blocks in ZnO based HGN provides unique characteristics for opportunities in future optoelectronic devices.

Chapter 2 Graphene Field Effect Transistors for Studying the Interactions Between Graphene and Bio/gas Molecules

Reprinted in part with permission from [Jian Lin, Desalegne Teweldebrhan, Khalid Ashraf, Guanxiong Liu, Xiaoye Jing, Zhong Yan, Rong Li, Mihri Ozkan, Roger K. Lake, Alexander A. Balandin, Cengiz S. Ozkan. “Gating of Single Layer Graphene Using Single-Stranded Deoxyribonucleic Acids”, *Small*, 2010, 6(10): 1150-1155]. Copyright Wiley. Reproduced with permission.

Abstract

In this chapter, we will present the study of the interaction of graphene with single stranded Deoxyribonucleic Acids (ssDNA) as well as gas molecules by using graphene field effect transistor (FET). In case of interaction between graphene and ssDNA, ssDNA are found to act as negative potential gating agents that increase the hole density in single layer graphene (SLG). Current-voltage measurement of the hybrid ssDNA/graphene system indicates a shift in the Dirac point and “intrinsic” conductance after ssDNA is patterned. The effect of ssDNA is to increase the hole density in the graphene layer, which is calculated to be on the order of $1.8 \times 10^{12} \text{ cm}^{-2}$. This increased density is consistent with the Raman frequency shifts in the G-peak and 2D band positions and the corresponding changes in the G-peak full-width half maximum. Ab-initio calculations using the density functional theory (DFT) rule out significant charge transfer or modification of the graphene bandstructure in the presence of ssDNA fragments.

In case of studying the gas molecular photodesorption and absorption from pristine and functionalized graphene layers made by CVD, we figure out that when graphene layers are treated with concentrated HNO_3 , the photodesorption induced current decrease becomes less significant than that of pristine graphene layers. We suggest this is due to the passivation of oxygen-bearing functionalities to CVD grown graphene structural defects by HNO_3 functionalization, which prevents the further absorption of gas molecules. The substantial understanding of interaction of graphene sheet with the bio-molecules and gas molecules will enable the capability of improving the applications of graphene in bio-sensor and chemical sensor.

2.1 DNA Negative Gating Effect in Single Layer Graphene

2.1.1 Introduction

Because of the two dimensional nanostructure and tunable surface chemistry, graphene layers are sensitive to the environment and chemical agents, which could provide ways to modulate its electrical properties through surface modification. To date, several different methods have been employed including electrochemical modification[114] and chemical molecule decoration[115-118] to modify the electrical properties of graphene layers. Deoxyribonucleic acid (DNA) and peptide nucleic acids (PNAs) which have base sequences that offer specificity are attractive assembly linkers for bottom-up nanofabrication. Engineered ssDNA sequences are employed in the nanoarchitectures of end-functionalized single walled carbon nanotubes for device applications including resonant tunneling diodes, field effect transistors and biochemical sensors[119-123]. A thorough understanding of electrical transport through the interface between biological molecules such as DNA and graphene layers is still in its infancy[43]. In this work, we investigate the modulation of carrier transport through graphene layers with overlaying ssDNA fragments via electrostatic interaction. We discovered that the role of ssDNA on the surface of graphene is analogous to applying a negative gate potential in conventional silicon CMOS architectures. Raman spectroscopy has been used in monitoring the doping of graphene layers. We observed a well defined shift in both the G-peak and the 2D band in the Raman spectra after the graphene layer is patterned with ssDNA fragments.

2.1.2 Materials and Experimental Methods

Material Preparation: The graphene samples used in this study were extracted from highly oriented pyrolytic graphite (HOPG) slabs via mechanical exfoliation. The ssDNA sequence employed in this work is CGGGAGCTCAGCGGATAGGTGGGC. The engineered oligonucleotides (Sigma Genosys) were diluted in distilled water to obtain the stock solution. Concentration of the ssDNA solution was calculated to be 28.86mg/ml. After the current-voltage measurements (I_{ds} - V_{gs}) of as-fabricated SLG transistors were measured in vacuum (1.0×10^{-3} Torr) at 300K, a 0.5 μ l droplet of ssDNA solution was patterned over the active part of the device, followed by incubation for 30 minutes in ambient environment and nitrogen drying. Then the current-voltage measurement of SLG transistors with patterned ssDNA was operated under vacuum (1.0×10^{-3} Torr) at 300K.

Fabrication of Graphene Field Effect Transistor (FET): The graphene samples were deposited on p-type degenerately doped Si (100) wafers (p++) covered with 300nm thick thermally grown SiO₂. For device fabrication, we patterned source and drain contacts using electron beam lithography followed by the deposition of source and drain metal consisting of 10nm thick Cr and 100nm thick Au layers (Temescal BJD-1800 electron beam evaporator). To ensure that the graphene layer was intact after device fabrication, we kept the samples under vacuum until ready for analytical characterization.

Experimental Methods: The Raman microscopy was used to identify the single layer graphene as well as the the Raman peak position shift before and after patterning the ssDNA on the top of the SLG. The Raman microscopy was carried out using the

Renishaw instrument. The spectra were excited by the 488 nm visible laser. A Leica optical microscope with 50x objective was used to collect the backscattered light from the graphene samples. The Rayleigh light was rejected by the holographic notch filter with a 160 cm^{-1} cut off frequency for 488 nm excitation. The spectra were recorded with the 1800 lines/mm grating. A special precaution was taken to avoid the local heating of the samples by the excitation laser. In order to achieve this, all measurements were carried out at low excitation power, below 2 mW on the sample surface. The power density on the sample surface was verified with an Orion power meter. The spectral resolution of the instrument determined by the hardware was $\sim 1\text{ cm}^{-1}$. The spectral resolution enhanced by the software processing of the peak positions was below 0.5 cm^{-1} . The enhanced resolution of the instrument was sufficient to accurately resolve the shifts in peak positions in the conditions of the experiments through Lorentzian peak fitting. The spatial resolution was defined by the diffraction limit and estimated to be around $0.5\text{ }\mu\text{m}$.

2.1.3 Material and Electrical Characterizations

Single layer graphene (SLG) flakes were selected with the help of micro-Raman spectroscopy using the 2D band deconvolution and comparison of the intensities of the G-peak and 2D bands [124, 125]. This approach has proven to be reliable for identification of the number of layers in graphene flakes and quality control. The absence of the disorder D band confirmed the high quality of the SLG used in this study as shown

in Figure 2.1[126]. Micro-Raman measurements were carried out in the backscattering geometry under 488nm laser excitation [124-127].

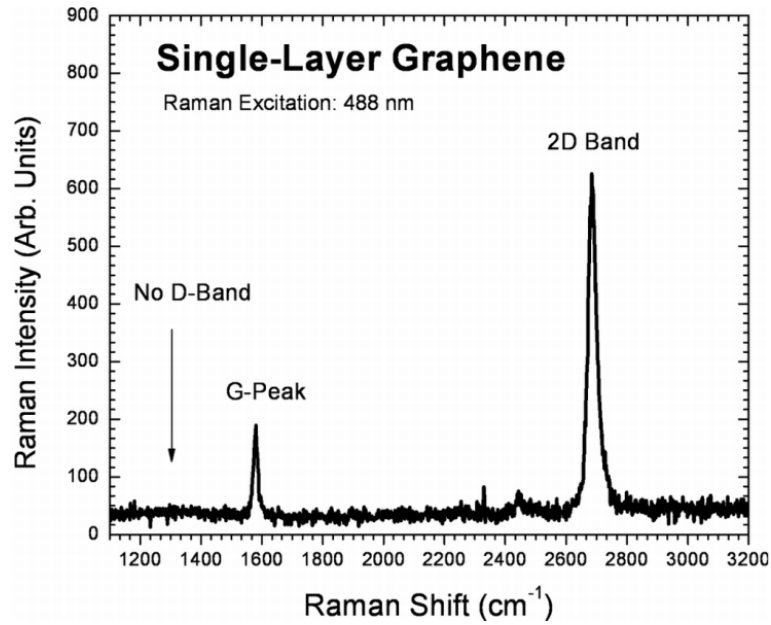


Figure 2.1 Raman spectrum collected from the SLG between two contacts after device fabrication showing the typical features. The absence of the D-band indicates that no substantial damage was caused during the fabrication process and electrical measurements.

A statistical study based on atomic force microscopy (AFM) imaging of the SLG layer before and after ssDNA patterning is shown in Figure 2.2. The average thickness of the SLG layer increased from ~1.0nm to ~1.8nm, indicating the formation of a thin layer of ssDNA on top of the SLG surface. From the AFM images, we observe the increased roughness of both the SiO₂ substrate and the SLG surface, which could be due to nonspecific and irregular binding of ssDNA fragments.

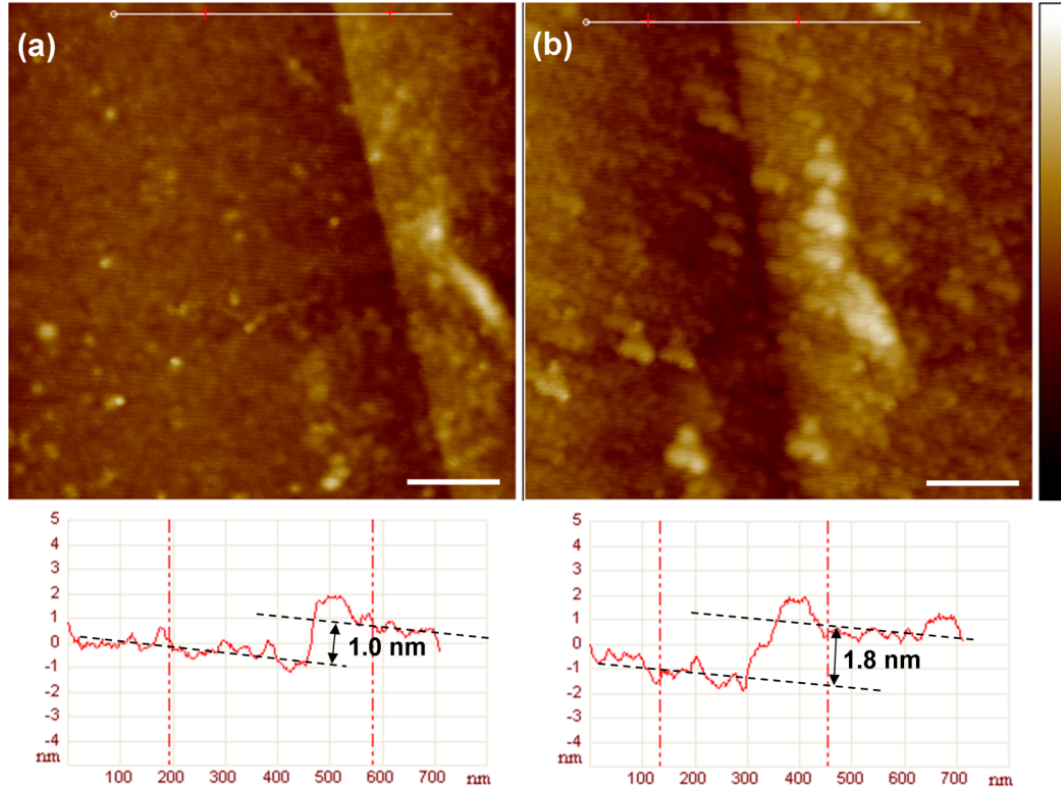


Figure 2.2 (a), (b) AFM images (1.1 $\mu\text{m} \times 1.1 \mu\text{m}$, Z-range 15nm) and accordingly cross sectional profiles of SLG before (a) and after (b) patterning with ssDNA. The measured thickness of SLG increases from $\sim 1.0\text{nm}$ to $\sim 1.8\text{nm}$ after ssDNA patterning. And the increased roughness (shown in two squares in image (a) and (b)) is due to the nonspecific and irregular binding of ssDNA to the SLG. The scale bar is 200nm. Color bars are 10nm.

Current-voltage measurements on the SLG transistor are conducted in vacuum (1.0×10^{-3} Torr) before and after ssDNA deposition to determine the modulation of electrical characteristics. Employing a simple MOSFET model [128], the carrier mobility was calculated using the following equation,

$$\mu = \left(\frac{\Delta I_{ds}}{\Delta V_{gs}} \right) / \left(\frac{C_g W V_{ds}}{L} \right) \quad (2.1)$$

where I_{ds} and V_{ds} are the source-drain current and voltage, V_{gs} is the back-gate source voltage, L and w are the effective channel length and width respectively, and C_g is the gate capacitance of the SLG device. Based on the data shown in Figure 2.3, the carrier mobility of the SLG transistor at the room temperature before ssDNA patterning was calculated to be $\sim 1303 \text{ cm}^2/(\text{V}\cdot\text{s})$, which is relatively low as compared to the reported values from about $2000 \text{ cm}^2/\text{vs}$ to $10^4 \text{ cm}^2/\text{vs}$ or even higher [17, 18]. This low carrier mobility could be due to the contact resistance or the surface impurities [129, 130]. However the mobility of this graphene is enough to interfacing the ssDNA and exhibiting the affect of ssDNA on tuning the electrical property of graphene. From the two curve plots, we deduce that hole mobility of graphene before and after ssDNA deposition is kept almost constant.

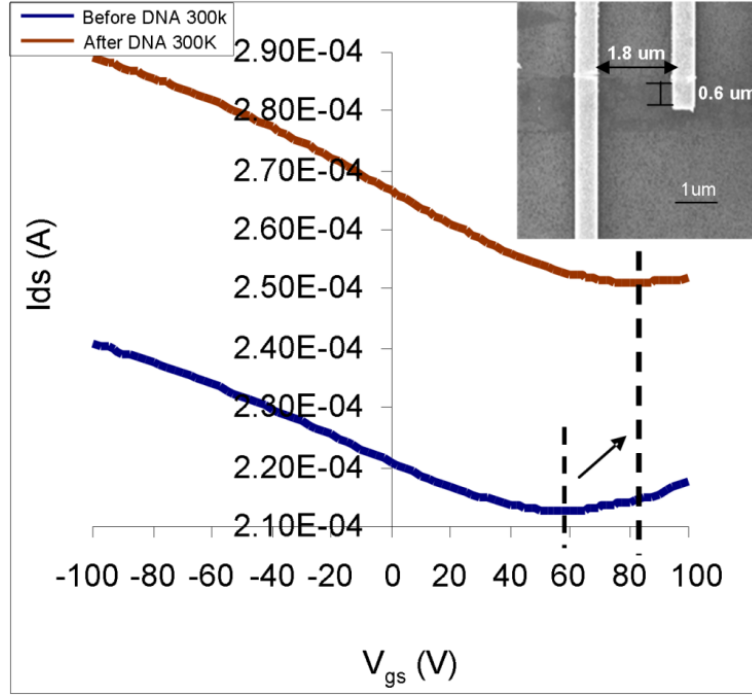


Figure 2.3 I_{ds} - V_{gs} characteristics of SLG before (black) and after (red) ssDNA patterning of SLG devices at $T=300K$. Source-drain bias voltage is 100mV. The dotted lines correspond to the Dirac point (Minimum conductance point). From the current-voltage measurements, it shows: (1) the gate voltage when minimum conductance point reaches shifts from 60V to 80V; (2) overall conductance shifts up. The top inset is the SEM image of the SLG device used in the measurements. The device channel length and effective width are 1.8 μm and 0.6 μm respectively.

From Figure 2.3, we observe the minimum conductance point (when the Fermi level is at the Dirac point) and the corresponding finite offset gate voltage which depends on the charge impurity [131]. After ssDNA is patterned on the SLG devices, a parallel shift in the minimum conductance point (MCP) is noticed, which may originate from the creation of more charge impurities. In other words, when negatively charged ssDNA attaches to graphene, we need to apply more positive voltage to compensate for this additional charge [132]. In a control experiment, we placed a droplet of DI water on the

SLG devices. Then after drying via nitrogen flow, electrical measurement under the vacuum was conducted, and no such shift in the MCP was observed. The increase in the offset of the Dirac point gate voltage is around 25V. The conductance of the SLG transistor is also increased; the increased hole density induced via ssDNA patterning was calculated to be $3.45 \times 10^{12} \text{ cm}^{-2}$ using the Drude model,

$$\Delta p = \left(R_2^{-1} - R_1^{-1} \right) / \left(\mu_p q \left(\frac{W}{L} \right) \right) \quad (2.2)$$

Where R_2 , R_1 are the resistances of the SLG device before and after ssDNA patterning. This increase in the hole density could be attributed to the following reason: ssDNA molecules with negative charge could act to induce a negative electric field effect (EFE) on the SLG [43]. This EFE could effectively induce the injection of extra holes in the graphene layer, hence the conductivity changes.

The change in the hole density is also calculated from a parallel plate capacitor model based on the shift in the gate voltage of the minimum conductance point (MCP),

$$\Delta p = \frac{C_g}{q} (V_{mcp2} - V_{mcp1}) \quad (2.3)$$

where V_{mcp2} and V_{mcp1} are the offset gate voltage in the minimum conductance point before and after ssDNA patterning. The excess hole density calculated from Eq. (2.3) is $1.8 \times 10^{12} / \text{cm}^2$ which is comparable to the value calculated with the Drude model.

2.1.4 Raman Spectroscopy Characterization

Raman spectroscopy has been intensively used for identifying the number of layers[133] and monitoring the doping of graphene layers. The major Raman spectra features for graphene are the G band (optical phonon at long wavelengths) at $\sim 1584\text{cm}^{-1}$, and the 2D band (associated with a two-phonon state) at $\sim 2700\text{cm}^{-1}$ in pristine SLG. However, in doped graphene, the G band and 2D band frequencies as well as the full width at half maximum (FWHM) value in the G peak are changed [72, 134, 135][136, 137].

To validate that ssDNA acting as a negative potential gating agent on top of SLG can induce additional holes, we measured the Raman spectrum on pristine SLG samples without device fabrication which may induce some contaminants and residue on the surface [138]. Next we patterned the same concentration of ssDNA on top of the SLG samples. Then the same Raman measurement was operated on the SLG samples with patterned ssDNA. The constant laser power below 2mW was employed to avoid the flakes and the patterned ssDNA layer are not damaged and to rule out the local heating effects [3, 71]. In Figure 2.4, we present the Raman spectra for which the main feature is the shift in the G and the 2D band positions as well as their FWHM. After ssDNA patterning, the average position of the G peak shifts from 1580cm^{-1} to 1582cm^{-1} . According to measurements by Ferrari et al.[72], a shift of $\sim 2\text{cm}^{-1}$ corresponds to a hole concentration of approximately $2.0 \times 10^{12} / \text{cm}^2$, which is comparable to the value based on electrical measurements. The reduction of the FWHM of the G peak after negative ssDNA gating is similar to the previously reported results for conventional electrostatic

gating [72, 134-137]. A detailed explanation for the decrease in the phonon G-peak FWHM value with an increase in carrier concentration has been previously provided [72, 134, 135].

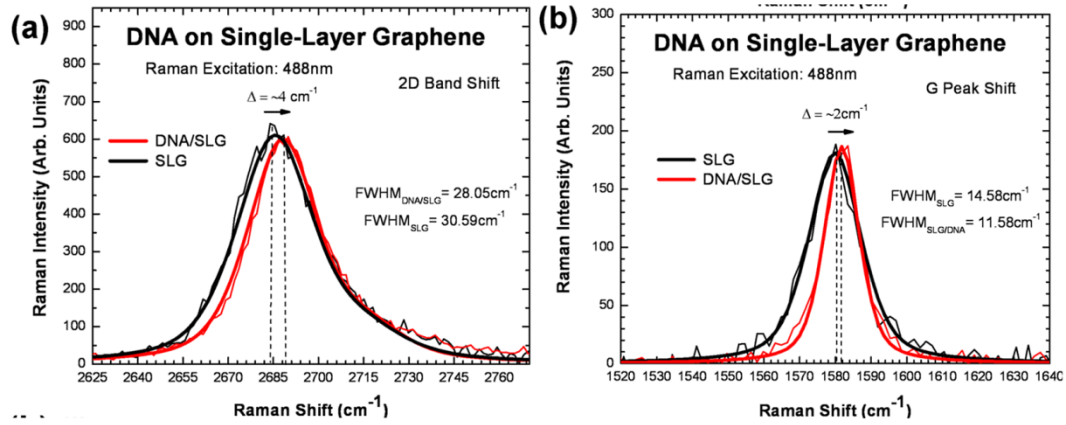


Figure 2.4 Micro-Raman spectroscopy of the signature G-peak and the 2D band for pristine SLG and the ssDNA/SLG system. In (a) the G-peak is centered at 1580cm^{-1} , observed at 488nm excitation wavelength, shifts an average 2cm^{-1} after ssDNA patterning. (b) Second order 2D band shifts by $\sim 4\text{cm}^{-1}$ as a result of ssDNA patterning. Both signature peaks also show relative shortening of their respective full width half max (FWHM) values.

Apart from the interpretation of the G peak, the 2D peak originates from a second-order, double-resonant (DR) Raman scattering mechanism [136]. We measured the shift of the 2D peak position after ssDNA patterning. In our measurements, the 2D band line is averagely centered at 2685cm^{-1} before ssDNA patterning and shifted to 2689cm^{-1} after ssDNA patterning, which is in agreement with the previously obtained results [134, 137]. The observed decrease in the FWHM in the 2D band could be due to the fact that the

electrostatic interaction between DNA and SLG could further modify the 2D band behavior.

The behavior of the G peak shows that ssDNA fragments could provide a negative electric field gating effect on graphene layers. The effect of ssDNA is that, as a negative potential gating agent, ssDNA can modulate the Fermi level by inducing excess hole carriers. This shift of the Fermi level results in the expansion of the equilibrium crystal lattice parameter with consequent stiffening of phonons and the onset of effects beyond the adiabatic Born–Oppenheimer approximation [72, 139].

2.1.5 Modeling and Theoretic Investigation

The experimental data indicates that patterning of ssDNA causes an effective p-doping of the SLG. This could be the result of negative charges associated with ssDNA. However, there are two other hypotheses that one could investigate on: (1) p-doping of the SLG could result from charge transfer between the SLG and the ssDNA. (2) The shift in the current versus gate-voltage curves could result from a modification of the SLG band structure due to an interaction with the ssDNA. Hypothetically, we found negative results for both of these hypotheses.

In order to investigate the above two possibilities, we performed ab-initio density functional theory (DFT) calculations of adenine and guanine bases physisorbed on a SLG. We focus on the bases since any charge transfer should occur in the frontier orbital, and the frontier orbital of ssDNA lies on its bases. Furthermore, any interaction that might modify the band structure of the SLG would likely be mediated by the π -orbital of the

bases interacting with the π -orbitals of the SLG. This is analogous to the interaction of ssDNA bases with carbon nanotubes that has been observed; ssDNA has been found to wrap around SWNTs and form helices [121, 122] with the bases physisorbing on the graphitic SWNT surface [140].

The graphene supercell used in the calculations consists of 16 atomic layers in the zigzag direction and 12 atomic layers in the armchair direction. A single nucleoside is placed above the graphene sheet. Both adenine and guanine nucleosides were simulated. The initial structure of the base on the graphene layer was taken following the results of Meng et al. where the structural properties of ssDNA physisorbed on SWNTs were determined using directional optical absorbance and ab-initio time dependent DFT methods [140].

Calculations are performed using the DFT implemented by the ab-initio tight-binding molecular dynamics code FIREBALL [141-143]. The BLYP exchange correlation functional is used with a double numeric sp^3 localized orbital FIREBALL basis. In the self-consistent field calculation, a Fermi smearing temperature of 50K and a self-consistent convergence factor of 10^{-5} are used. The 2-D Brillouin zone is sampled with 6 k-points in each direction during optimization. Structures are relaxed until all Cartesian forces on the atoms are $< 0.05 \text{ eV } \text{\AA}^{-1}$. The relaxed structure of SLG with the physisorbed adenine nucleoside is shown in Figure 2.5(a). The distance between the SLG plane and the adenine base is approximately 3.35 \AA .

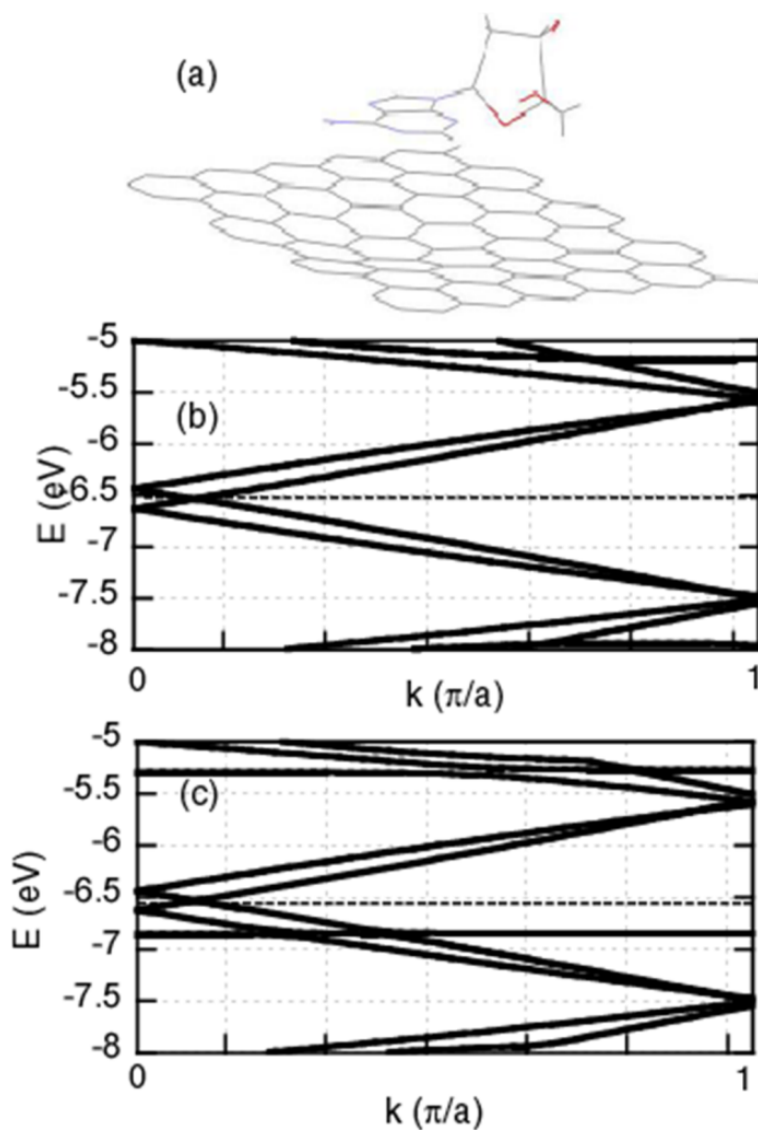


Figure 2.5 (a) An adenine nucleoside on the graphene supercell. (b) Energy versus k relation of a pristine graphene sheet along the armchair direction. A supercell is used for repeat unit that contains 16 layers in the zigzag direction and 12 layers in the armchair direction. The dotted line shows the charge neutral Fermi level of the system. (c) Energy versus k relation of a graphene sheet with physisorbed adenine nucleoside. The dimensions of the graphene supercell is identical to the one used for (b). The dotted line shows the charge neutral Fermi level of the system.

The calculated charge transfer from the SLG to adenine is 0.02 electrons, and the charge transfer from the SLG to guanine is 0.09 electrons. Both values are very small. This is expected from a consideration of the energy levels. The ionization potentials of adenine and guanine are 8.5eV and 7.85eV, respectively [144]. The electron affinities of adenine and guanine are of the order of 0.95 and 1.51eV, respectively [145]. The work function of SLG is 4.5 eV [146]. The occupied energy levels of the bases lie well below the Fermi level of SLG and the unoccupied levels are well above the Fermi level. Hence, the weak interaction through the π -orbital should not cause charge transfer from SLG to the bases since the HOMO levels are already filled. To achieve an effective hole doping of $\sim 2.0 \times 10^{12} / \text{cm}^2$, assuming an average charge transfer of 0.05 electrons per base, would require an areal density of base monomers of $4.0 \times 10^{13} / \text{cm}^2$. This value is more than an order of magnitude higher than the density that is estimated. Therefore, it is unlikely that this charge transfer is responsible for the apparent hole doping that is observed.

The energy versus wavevector relation for pristine SLG is shown in Figure 2.5(b), and the energy versus wavevector relation for SLG with adenine nucleoside is shown in Figure 2.5(c). The SLG band structure is unaffected by the adenine base. Most importantly, the band crossings at the Dirac point are left unchanged. Therefore, we cannot attribute the shift in the current versus gate voltage curves to a change in the band structure of the SLG.

2.1.6 Conclusion

We demonstrated that ssDNA fragments act as negative potential gating agents resulting in an increase in the hole density in graphene layers. By using current-voltage measurements, we computed an increase in the hole density with a value of about $1.8 \times 10^{12} \text{ cm}^{-2}$ based on both the change in resistance and the shift in the voltage of the minimum conductance point. This value is consistent with the peak-position shift of the G band and the 2D band of the Raman spectra. We ruled out changes due to charge transfer or modification of the SLG bandstructure due to the presence of ssDNA. Furthermore, we discussed the relationships between the gating effect induced by the ssDNA fragments and the change in the phonon frequency, and demonstrated that patterning of biomolecules on graphene layers could provide new avenues to modulate their electrical properties.

2.2 Gas Molecular Absorption and Photodesorption in Pristine and Functionalized Large-area Graphene Layers

2.2.1 Introduction

Graphene, isolated in 2004[11], has been demonstrated as a major potential candidate for a variety of applications including chemical-[33, 39] and bio-sensors[43] owing to its extremely sensitive planar structure, which readily absorbs the molecules acting as donors or acceptors. Since then, a number of theoretical [34-36] and experimental [33, 37-41, 147, 148] studies have investigated the molecular absorption and desorption behavior of mechanically exfoliated or chemically derived graphene and graphene oxide layers. Recently, the utilization of chemical vapor deposition (CVD) in the synthesis of uniform large-scale graphene layers provides a promising route of meeting the industrial needs for processing on large substrates [52-54]. However, only a few experimental studies so far have investigated the molecular photodesorption and absorption behavior of CVD grown graphene layers and their functionalized counterparts.

Here, we describe recent research on molecular photo-induced desorption of pristine and nitric acid (HNO_3) treated CVD grown graphene field effect devices under ultraviolet (UV) light illumination in the presence of oxygen and ammonia. Electrical characterization including time evolution of conductivity, transfer characteristics, and sheet resistance show the photodesorption of gas molecules from pristine graphene layers. The presence of HNO_3 weakens the photodesorption induced current reduction behavior in functionalized CVD grown graphene layers. The potential mechanism was

determined by comparison of electrical measurements in absorption and desorption processes of pristine and HNO₃-treated graphene layers.

2.2.2 Materials and Experimental Methods

Synthesis of Graphene by CVD: In the CVD growth process, graphene films were synthesized on nickel thin films at 900°C using a highly diluted methane gas source under ambient pressure conditions in a hot wall furnace. 200nm thick Ni catalyst films were deposited by electron beam evaporation on Si/SiO₂ substrates. Nickel deposited substrates were heated to 900°C in an Ar/H₂ (300:300 standard cubic centimeter per minute- sccm) atmosphere and annealed for 30 minutes in order to increase the nickel grain size. After flowing methane (30sccm) mixed with Ar/H₂ at 900°C under ambient pressure for 1 minute, the furnace was cooled down to 25°C at a medium/fast cooling rate of 10°C/s. After that, the residual Ni layer underneath was etched in a mild 3% HCl aqueous solution.

FET Device Fabrication: Each graphene film was transferred onto a Si/SiO₂ substrate with highly doped Si back-gate electrode and 300nm thermal oxide gate dielectric. The few-layer graphene film was patterned into rectangular shapes 2μm-wide and 20μm-long by photolithography and reactive ion etching (RIE). Next, four-terminal devices were fabricated by photolithography followed by electron beam evaporation of Ti/Au (8nm/80nm) which forms Ohmic contacts to graphene. Before electrical measurements were performed, all of the devices were annealed under flow of 200sccm Ar and 200sccm H₂ at 400°C for 1 hour to remove any organic residues. For the

comparison experiments: after all the electrical measurements were completed, the same graphene field effect (GFET) devices were treated in 67wt% HNO_3 for 5 minutes and rinsed with DI water followed by N_2 blow-drying.

Experimental Methods: A Renishaw Raman microscope with a 514nm laser source was used to characterize the doping process by HNO_3 functionalization. The backscattered light from graphene samples was collected with a 50x objective lens. To avoid the local heating effects by the excited laser, a low excitation power with 2mW on the graphene surface was used. The spectral resolution of the instrument determined by the hardware was $\sim 1 \text{ cm}^{-1}$. The spectral resolution enhanced by the software processing of the peak positions was below 0.5 cm^{-1} .

For photodesorption measurements, UV illumination with a wavelength of 365 nm and power intensity of $4\text{W}/\text{cm}^2$ was employed and kept at a distance of 10cm from the graphene samples. For the electrical measurements, all of the samples were placed inside a vacuum chamber connected to gas purging system. All of the electrical measurements were conducted under room temperature using a programmable Agilent 4155C unit interfaced to a computer. For the $I_{\text{ds}}\text{-}V_{\text{gs}}$ transfer characteristics, a constant 10mV source-drain voltage was applied to the samples while the source-drain current I_{ds} was recorded as a function of the sweeping gate bias V_{gs} . For the photodesorption and absorption measurements, we kept the source-drain voltage constant of 10mV and monitored the I_{ds} varying with time. In data analysis, we normalized the measured conductivity values by the initial conductivity. For absorption and desorption process measurements, initially all of the devices were fully degassed by UV illumination and applied current flow under

vacuum. Next, the devices were exposed to dry air and anhydrous NH_3 (99.995%, $\text{HO}_2 < 1\text{ppm}$) and the electrical conductivity was measured over time while the chamber pressure was varied by controlling the amount of gas in the vacuum chamber.

2.2.3 Molecular Absorption and Photodesorption of Pristine Graphene

From the Raman spectra shown in figure 2.6, we can see that CVD grown graphene films are generally composed of single layer region as well as partial few layer region (less than 5 layers)[113]. Unlike the mechanically exfoliated graphene, although there generally exist defects or vacancies along the catalyst boundaries generated during growth in CVD graphene, the small ratio of G peak to D peak from the Raman spectra of SLG (single layer graphene) and FLG (few layer graphene) indicates the relative low defect density states. The photoelectrical characterization of pristine graphene field effect transistor (GFET) devices was carried out in the ambient environment under UV light. The fabricated GFETs are shown in the inset of Figure 2.6b. Also we can see that upon exposure to the UV light, the graphene layer conductivity (G) decreased and then slowly recover to a certain level when the UV light is turned off. This decreased conductivity was thought to be caused by oxygen photodesorption from the carbon material [37, 41, 149-151].

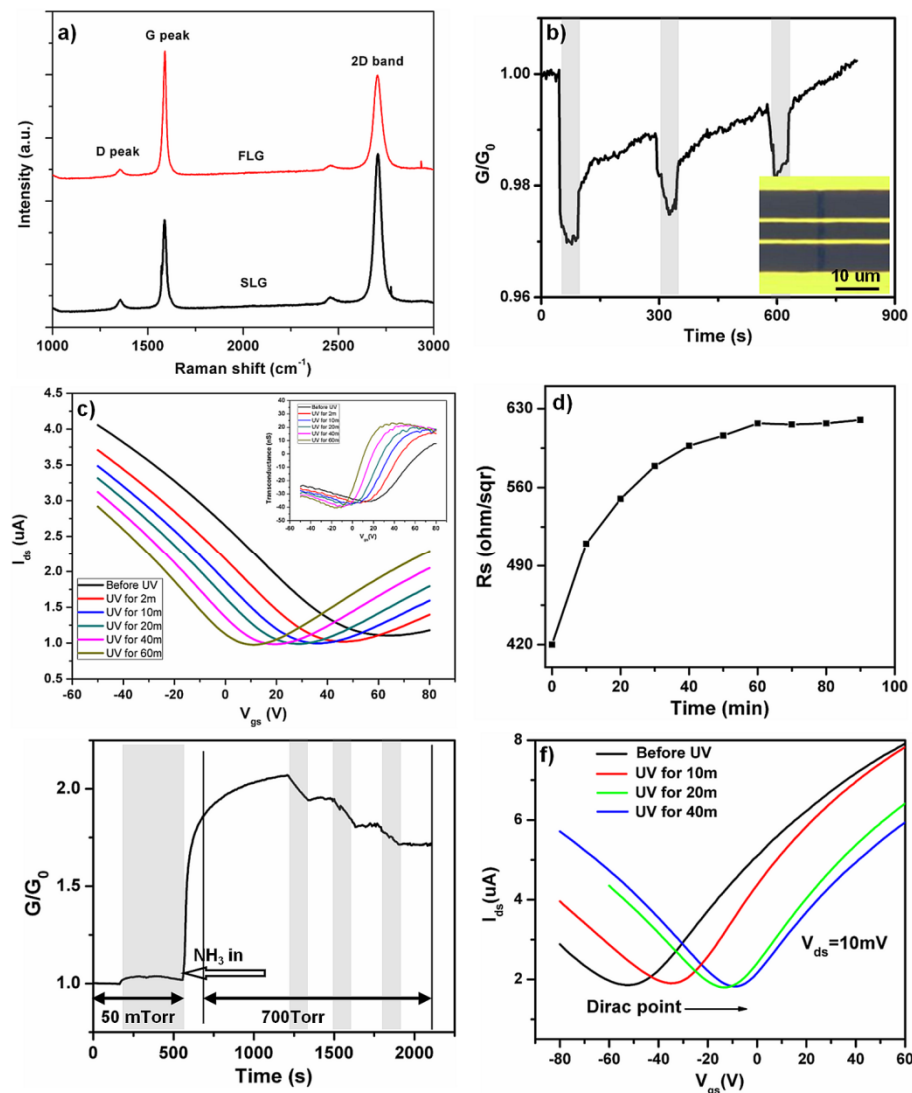


Figure 2.6 Molecular photodesorption of CVD grown graphene layers before HNO_3 treatment. (a) Raman spectra of CVD grown graphene indicating single layer and few-layer graphene region. (b) Normalized conductivity G/G_i [initial conductivity: $G_i = (4\text{k}\Omega)^{-1}$] of a GFET vs time during UV illumination cycles in ambient air. Shaded and unshaded regions represent the UV-on and -off periods respectively. The inset is the optical image of a four-contact GFET device. (c) Transfer characteristics of GFET under continuous UV illumination in vacuum ($p=10\text{mTorr}$). Inset: Correspondingly extracted transconductance of the same device. (d) Sheet resistance changes with time under UV illumination. (e) Normalized conductivity [initial conductivity: $G_i = (4.4\text{k}\Omega)^{-1}$] of GFET devices during NH_3 absorption and photo-desorption cycles. Shaded regions represent the UV-on periods. The samples were degassed before NH_3 absorption and photo-desorption. (f) Transfer characteristics of NH_3 absorbed GFET under continuous UV illumination in vacuum ($p = 10 \text{ mTorr}$).

The transfer characteristics of graphene based devices under exposure to continuous UV light at different time durations are demonstrated in Figure 2.6c. From the I_{ds} - V_{gs} characteristics the hole and electron mobility of graphene can be estimated. Using the equation in reference[152] we estimated the carriers mobility of graphene to be about $1560 \text{ cm}^2/(\text{V}\cdot\text{s})$ for holes and around $1300 \text{ cm}^2/(\text{V}\cdot\text{s})$ for electrons. And carriers mobility of all the devices used for study is in the range of $1050\sim 1740 \text{ cm}^2/(\text{V}\cdot\text{s})$ for holes and in the range of $950\sim 2780 \text{ cm}^2/(\text{V}\cdot\text{s})$ for electrons. Besides, from figure 2.6c it can be seen that the Dirac point of the graphene device was initially at $\sim 70\text{V}$, indicating the usual p-type doping effect in graphene layers [37, 151]. A negative shift of the Dirac point to $\sim 5\text{V}$ (close to the intrinsic) after 60 minutes of exposure to UV light demonstrates the UV de-doping effect, which was consistent with the result that the UV light induced the desorption of oxygen from the graphene layers[37]. The extracted transconductance (inserted in figure 2.6c) of graphene device under continuous UV illumination for 60 minutes keeps almost constant in the whole voltage sweep range, even has slight increase for the p-channel conductance. This indicates that mobility of graphene layers does not degrade as the continuous UV illumination, which shows that UV illumination does not induce external defects to the graphene layers. To see the effect of UV on the graphene layers, we measure the sheet resistance which is increased from 470 ohm/sqr to 620 ohm/sqr after 1 hour UV illumination (see figure 2.6d). As the previously stated that the carrier mobility of graphene layers does not change with UV illumination the decrease of conductivity $\sigma = \frac{1}{\rho} = n\mu e$ (ρ resistivity, n carrier concentration, μ mobility) indicates

the decrease of carrier concentration. Assuming that carrier mobility equals $1500 \text{ cm}^2/(\text{V}\cdot\text{s})$, the decreased carrier concentration is estimated to be $2.2 \times 10^{12} \text{ cm}^{-2}$. The reason of the increased sheet resistance (or decreased conductivity) of graphene after the photodesorption of oxygen, we believe, is that oxygen molecules which act as electron acceptors in graphene are desorbed from graphene layers by UV illumination[33, 37, 41, 151].

In order to investigate the photodesorption behavior in pristine CVD graphene layers, NH_3 (ammonia) was flown into the vacuum chamber (at 10mTorr), and then the pressure was maintained at 10 Torr after GFET were degassed upon UV illumination. From Figure 2.6e, the constant conductivity upon UV illumination before introducing NH_3 indicates that the samples are fully degassed. Similar to previous observations in carbon nanotubes [149], the conductivity of graphene layers increases due to the n-type doping[41, 153] when NH_3 molecules are absorbed onto the graphene layers, and then decreases upon UV illumination (in figure 2.6e). However unlike NH_3 photodesorption and adsorption to CNT in the repeated UV -on and -off cycles [149], no repeated adsorption of NH_3 is noticed for graphene layers when the UV light is off. Similar to observations in CNTs [149], non-recovery and downward shift of conductivity appears due to the remaining co-adsorbed oxygen in the chamber. Figure 2.6f exhibits the transfer characteristics of NH_3 -doped GFET device under the illumination of UV light for different time durations. The shift of the Dirac point from -60V to -5V after 40 minutes of UV illumination indicates the photodesorption effect of NH_3 .

2.2.4 Molecular Absorption and Photodesorption of Functionalized Graphene

Recently, highly concentrated nitric acid (HNO_3) has been employed to increase the conductivity in CVD grown graphene layers for the application in optoelectronic devices [51]. It would be interesting to investigate the photoelectrical respond in HNO_3 treated CVD grown graphene layers. The Raman spectra collected from the same single graphene layer range before and after HNO_3 treatment is shown in Figure 2.7a. The large blue shift of the G peak ($\Delta = 8.5 \text{ cm}^{-1}$) indicates that the graphene layer is strongly p-type doped [72, 152]. Inset is the Raman spectrum of single layer graphene region chose for comparison experiments. Transfer characteristics of CVD GFETs before and after HNO_3 treatment are shown in Figure 2.7b. The positive shift of the Dirac point after HNO_3 treatment can be clearly observed. It verifies that HNO_3 is effectively providing p-doping in graphene layers.

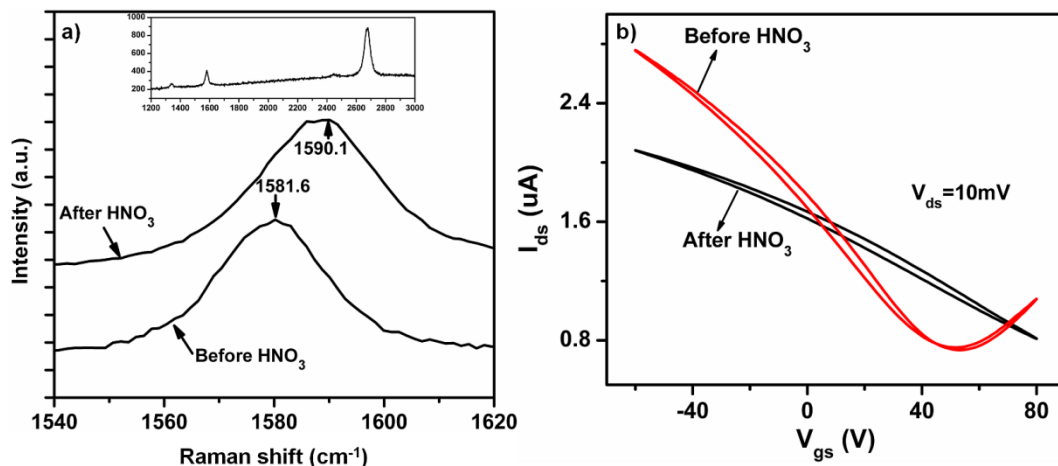


Figure 2.7 (a) Raman spectra of pristine and HNO₃ treated CVD grown single-layer graphene region. About 8.5cm⁻¹ of a blue shift for the G peak is observed in the spectra, showing the strong p-type doping effect of HNO₃. Inset is the Raman spectrum of single layer graphene region chose for comparison before and after HNO₃ treatment. (b) Transfer characteristics (I_{ds} - V_{gs}) of GFET measured under vacuum ($p=10\text{mTorr}$) before and after HNO₃ functionalization.

To investigate the effect of HNO₃ on the molecular photodesorption behavior of graphene, time-dependent photodesorption experiments were conducted on pristine and HNO₃ treated GFETs. Here we present comparison data from the same devices where consistent and similar results were obtained in more than 10 devices which were fabricated from the same CVD grown large-area graphene film. Upon continuous UV illumination, the conductivity of pristine graphene layers decreased by 52%, while the conductivity of HNO₃ treated transistors decreased only by 21% (Figure 2.8).

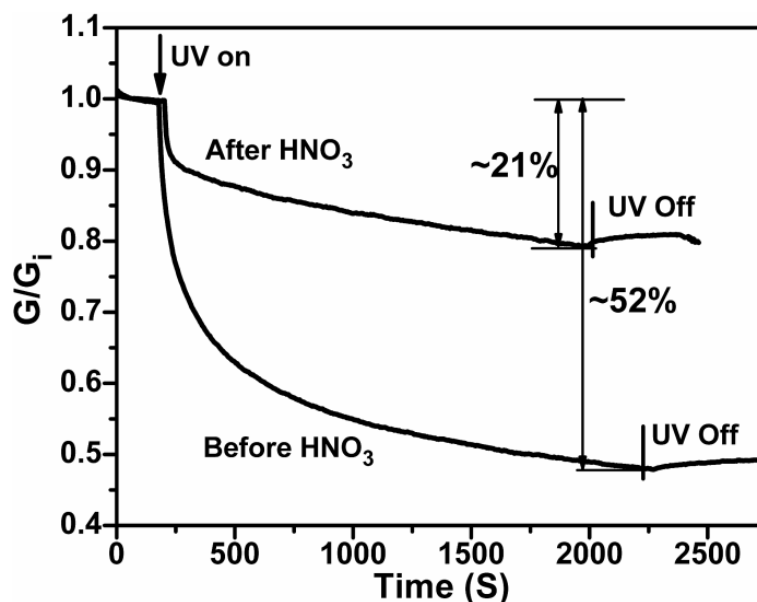


Figure 2.8 Normalized conductivity G/G_i [initial conductivity $G_i = (3.1\text{k}\Omega)^{-1}$] of CVD grown graphene layers before and after HNO_3 functionalization vs time in vacuum ($p = 10\text{ mTorr}$).

In a previous study on photodesorption on the surface of a metal oxide layer, it was shown that the amount of desorbed gas molecules in the photodesorption process was related to the states of the defects [154]. It is well known that, unlike mechanically exfoliated graphene layers, in CVD grown graphene layers, there generally exist dangling bond (DB) defects or vacancies along the catalyst boundaries generated during growth [52, 112, 113]. Although the gas molecules can be absorbed on the graphene surface [41], the structural defects may play an important role in molecular absorption in graphene layers and CNTs [36, 155]. Treatment with HNO_3 for a short time is not destructive to the graphene surface structure[51] but it is enough for the DB defects to be reactively bonded with oxygen-bearing functionalities induced by the HNO_3 [156]. Hence, such

functionalization readily passivates the structural defects with oxygen-bearing functionalities, thus reducing the absorption effects in graphene layers.

To further elucidate the effect of HNO_3 on the molecular photodesorption behavior of graphene layers, we compared the real-time absorption and desorption processes of pristine and functionalized GFETs under varying ambient pressure. We discovered that the conductivity of pristine graphene layers increased by 30% (in absorbing oxygen) while for functionalized layers it kept almost constant, as shown in Figures 2.9a and 2.9b. Similarly, Figures 2.9c and d indicate that the increase in conductivity for pristine GFETs was much more than the functionalized GFETs when absorbing NH_3 (84% to 16%). As shown in Figure 2.9d, a decrease in conductivity is observed initially when NH_3 was introduced into the vacuum chamber, because NH_3 donates electrons to the p-type doped graphene layers (by HNO_3 functionalization). This absorption phenomenon indicates that a prior HNO_3 treatment greatly changes the electrical properties of CVD grown graphene layers in their molecular absorption behavior. Comparing the results in Figures 2.9c and 2.9d for desorption process under NH_3 , the reduction in conductivity (84%) of graphene layers before HNO_3 functionalization is much more than the case after functionalization (11%). Comparing the desorption processes in air and HN_3 , we find that O_2 cannot be desorbed from the graphene layers while NH_3 can be desorbed almost fully to restore the original state by decreasing the chamber pressure (comparison of Figures 2.9a with 2.9c, and 2.9b with 2.9d). This could be due to the fact that O_2 has a greater absorption energy [36].

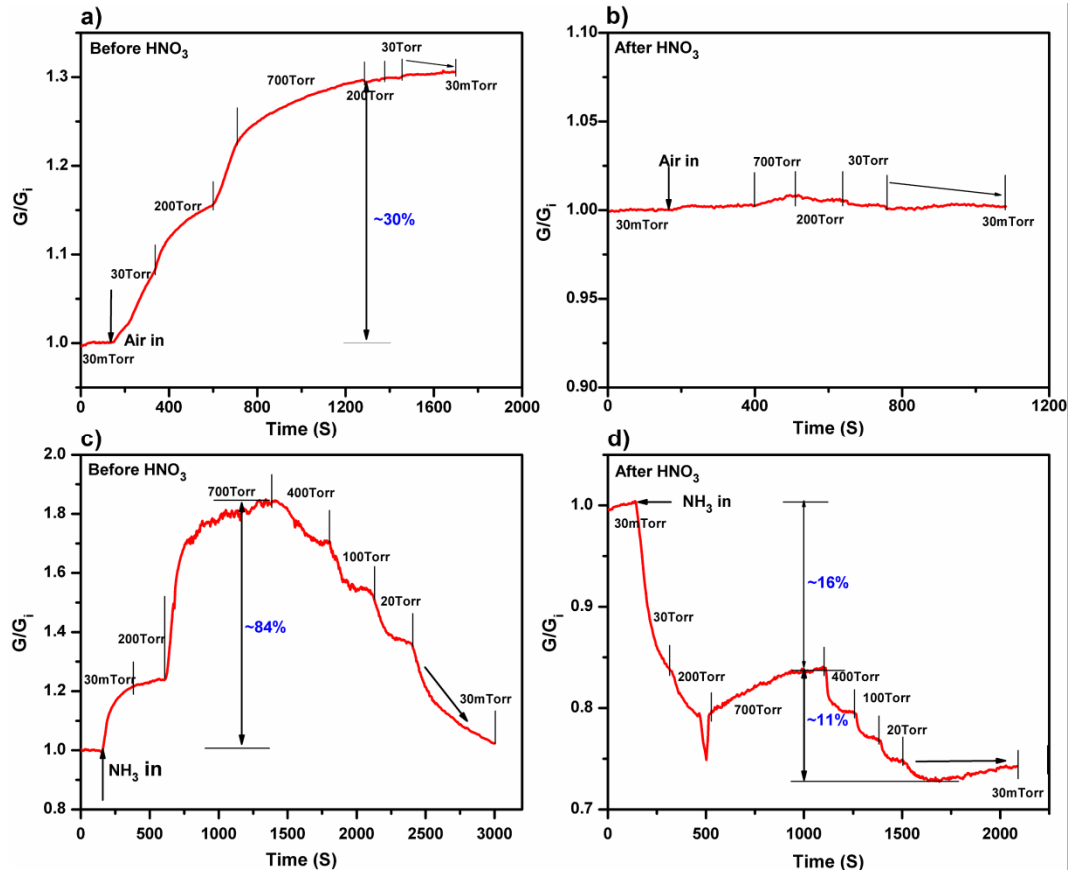


Figure 2.9 Molecular absorption and desorption of CVD grown graphene layers before and after HNO_3 functionalization under different pressures. (a) Normalized conductivity G/G_i [$G_i = (4.6\text{k}\Omega)^{-1}$] of graphene layers before functionalization in air under different pressures. (b) Normalized conductivity [$G_i = (3.9\text{k}\Omega)^{-1}$] of graphene layers after functionalization in air under different pressures. (c) Normalized conductivity [$G_i = (4.2\text{k}\Omega)^{-1}$] of graphene layers before functionalization in NH_3 under different pressures. (d) Normalized conductivity [$G_i = (5\text{k}\Omega)^{-1}$] of graphene layers after functionalization in NH_3 under different pressures. All of samples were degassed under UV illumination and voltage annealing under vacuum prior to electrical measurements.

2.2.5 Conclusion

Electrical characterization of pristine CVD grown graphene layers indicates that the decrease in conductivity under UV illumination is mainly attributable to the photodesorption of O_2 or NH_3 . The existing structural defects in CVD grown graphene layers may play an important role in the absorption of gas molecules, which will be the subject of future research. HNO_3 functionalization may readily passivate the structural defects with oxygen-bearing functionalities, thus reducing the absorption effects in CVD graphene. Our research provides a significant contribution to understanding the photo-induced molecular desorption process in graphene layers. Future research in graphene electronics is aimed at achieving the heterogeneous integration of large area graphene layers to CMOS architectures for two major purposes: (a) providing novel interconnects that could surpass the known performance metrics of copper interconnects, (b) providing simultaneous thermal spreading for effective near junction thermal transport. The development of a new doping methodology for graphene layers will provide the means to achieve these goals.

2.3 Conclusion

In this chapter, graphene field effect transistors are fabricated to study the interaction graphene between single stranded Deoxyribonucleic Acids (ssDNA) and gas molecules. ssDNA are found to act as negative potential gating agents that increase the hole density in single layer graphene (SLG). Later, the molecular photodesorption and absorption from pristine and functionalized graphene fabricated by CVD process is studied. The photodesorption induced current decrease in functionalized graphene by concentrated HNO_3 becomes less significant than pristine graphene layers (from 52% to 21%). Our results provide a new strategy for stabilizing the electrical performance of CVD grown large-area graphene layers for applications ranging from nanoelectronics to optoelectronics. Overall, the substantial understanding of interaction of graphene sheet with the bio-molecules and gas molecules will enable the capability of improving the applications of graphene in bio-sensor and chemical sensor.

Chapter 3 Graphene Synthesis by Chemical Vapor Deposition and Its Application in Organic Solar Cell

Abstract

The graphene layers are synthesized both on nickel thin film and copper foil by CVD process. It is more difficult to control the uniformity of graphene films grown from Ni thin film than the one grown from copper foils. Material characterizations indicate that the number of graphene layers synthesized on Nickel thin film is between 1-5 layers. While, the number of graphene layers synthesized on copper foil can be tunable, from 95% of layer with uniform single layer to non-uniform above ten layers depending on the growth conditions. Readily, the defect states exist in CVD graphene layers. The carrier mobility of graphene grown by CVD process is comparable to the mechanically exfoliated graphene layers.

To lower the sheet resistance of graphene films as transparent electrodes, the layer by layer transferred method is employed by utilizing uniform single layer graphene grown from copper foil. The effect of the chemical functionalization using highly concentrated HNO_3 in the graphene is to improve the conductivity and surface wettability. Lastly, compared with ITO-based organic photovoltaic solar cell, the fabricated graphene based solar cell exhibits relatively lower power conversion efficiency (PCE). To improve PCE of graphene-based organic solar cell, some approaches like synthesizing the uniform few-layer graphene film with high quality using Cu catalysts by controlling the growth conditions (growth pressure and the cooling rate) and improving the surface wettability by interfacial chemical engineering are suggested.

3.1 Introduction

Currently, widely applied transparent electrodes in optoelectronics are indium tin oxide (ITO) and fluorine tin oxide (FTO). However, these metal oxides show some drawbacks: high cost because of the rare element-indium, the low mechanical flexibility, limited optical transmittance at the near or infrared region, and the instability when exposed to acid or some chemicals. Therefore, substitution of these metal oxides in optoelectronics with other cost-effective and higher quality materials becomes important research topic. Recently, newly explored atomic layer material-graphene has drawn dramatic attentions as transparent electrodes because of potential low-cost, chemical alertness, broad optical transmittance region[48, 49]. However, it has not entered the industrial applications because of the limitation of synthesis methods like mechanical exfoliation or liquid exfoliation until the recent advance of chemical vapor deposition (CVD) in synthesizing continuous and wafer-size single layer graphene films with high quality[51, 53]. It provides the pave of substituting the ITO or FTO with transparent and conductive graphene film in optoelectronics.

Herein, we report the synthesis of large-area graphene films from nickel thin films and the copper foils using CVD approach. Usually, the uniformity of graphene films grown from Ni is more difficult to control than the one grown from copper foils. While under low pressure the uniform single layer graphene can be achieved from Cu-catalyst. The organic solar cells are fabricated using four-layer graphene films as anode by lay-to-layer transfer technique. HNO_3 improves the conductivity and the surface wettability of graphene in the application of anode in photovoltaic cells.

3.2 Material Synthesis and Experimental Methods

3.2.1 Material Synthesis

In the CVD growth process, graphene films were synthesized on nickel thin films at 900°C using a highly diluted methane gas source under ambient pressure conditions in a hot wall furnace. 200nm thick Ni catalyst films were deposited by electron beam evaporation on Si/SiO₂ substrates. Nickel deposited substrates were heated to 900°C in an Ar/H₂ (300:300 standard cubic centimeter per minute- sccm) atmosphere and annealed for 30 minutes in order to increase the nickel grain size. After flowing methane (30sccm) mixed with Ar/H₂ at 900°C under ambient pressure for 1 minute, the furnace was cooled down to 25°C at a medium/fast cooling rate of 10°C/s. After that, the residual Ni layer underneath was etched in a mild 3% HCl aqueous solution.

In case of synthesizing graphene on copper foil, the single-layer or few-layer graphene films were grown on 25 um thick copper foils (purchased from Alfa Aesar, 99.8%) at 1000 °C through chemical vapor deposition. In the first step of synthesis, the copper foil was inserted in the middle of heating zone of the quartz tube. Then the foil was heated to 1000 °C with flowing 30 sccm H₂ at various pressure (from 0.5 Torr to 40 Torr, shown in table 1), and annealed for 30 minutes under the same flow rate and pressure to increase the Cu grain size. After flowing the gas mixture of CH₄ and H₂ with flow rate of 60 sccm and 30 sccm respectively for 20 minutes, the temperature was cooled down to room temperature at medium/fast cooling rate of 100°C/min with flowing 200sccm H₂ at constant pressure as growth pressure (shown in table 1). After the growth, we spun coated the top of the copper foil with poly (methyl methacrylate) (PMMA) at

speed of 1000 RPM for 30 seconds and then baked at 140°C for 5 minutes. Subsequently oxygen plasma (STS Reactive Ion Etcher (RIE)) was employed to remove the graphene grown on the rear side of the copper foil. Then graphene films, on top side of Cu foil protected by PMMA were released by etching the Cu foil in 1M FeCl₃ solution, followed by subsequent cleaning in mild HCl aqueous solution (5%) and DI water. After the graphene films were transferred to Si/SiO₂ or quartz substrates the PMMA was resolved using acetone followed by Isopropyl alcohol (IPA). The whole synthesis procedures are indicated in the following schematic (figure 3.1).

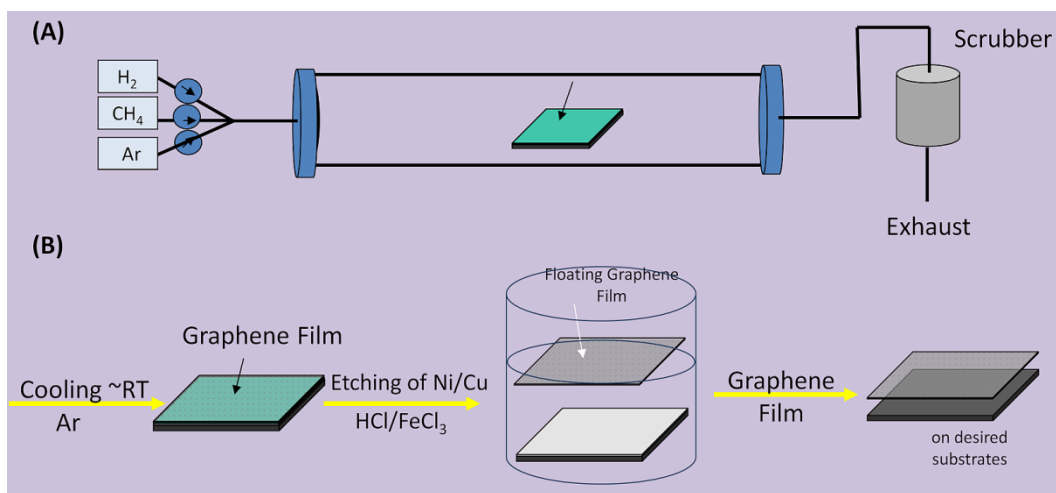


Figure 3.1 Schematic of synthesis of large-area graphene films by chemical vapor deposition (CVD). (A) Schematic of vacuum tube furnace. (B) Synthesis and transfer procedure of graphene by CVD.

3.2.2 Graphene FET and Solar Cell Devices Fabrication

Next, each graphene film was transferred onto a Si/SiO₂ substrate with highly doped Si back-gate electrode and 300nm thermal oxide gate dielectric. The few-layer graphene film was patterned into rectangular shapes 2μm-wide and 20μm-long by photolithography and reactive ion etching (RIE). Next, four-terminal devices were fabricated by photolithography followed by electron beam evaporation of Ti/Au (8nm/80nm) which forms Ohmic contacts to graphene. Before electrical measurements were performed, all of the devices were annealed under flow of 200sccm Ar and 200sccm H₂ at 400°C for 1 hour to remove any organic residues.

To fabricate the solar cell devices, first of all, four layer graphene films with transmittance of 90% were transferred to glasses by layer-to-layer transferred methods described in paper[51]. Then highly concentrated nitric acid was employ to dope the graphene layers as well as to improve the surface wettability which improved the adhesion between graphene and the polymer. After that metal contacts (Ni/Au:30/100nm) was E-Beam evaporated on the edges of the graphene films. The whole solar cell devices fabrication process was done in the nitrogen environment chamber. Firstly, poly-3,4-ethylene-dioxy-thiophene:polystyrene sulfonate (PEDOT:PSS - Baytron PTM) was spincoated (2000 rpm) from aqueous solution (after passing through a 0.45 μm filter), and then baked at 150°C for 10 min. The active-layer was subsequently deposited by spin-coating a mixture of P3HT (1.0 wt%) and PCBM (1.0wt%) dissolved in ODCB at 700 rpm for 50 s, then annealing the cell on hot plate at 120 °C for 30 minutes. LiF/aluminum

(1nm/80nm) cathodes were finally thermally evaporated on top of the solar cell through a shadow mask with 4mm×4mm square openings.

3.2.3 Experimental Methods

Raman characterization: A Renishaw Raman microscope with a 514nm laser source was used to characterize the quality of graphene. The backscattered light from graphene samples was collected with a 50x objective lens. To avoid the local heating effects by the excited laser, a low excitation power with 2mW on the graphene surface was used. The spectral resolution of the instrument determined by the hardware was $\sim 1 \text{ cm}^{-1}$. The spectral resolution enhanced by the software processing of the peak positions was below 0.5 cm^{-1} .

Electrical and Solar Cell characterization: For the electrical measurements, all of the samples were placed inside a vacuum chamber connected to gas purging system. All of the electrical measurements were conducted under room temperature using a programmable Agilent 4155C unit interfaced to a computer. For the I_{ds} - V_{gs} transfer characteristics, a constant 10mV source-drain voltage was applied to the samples while the source-drain current I_{ds} was recorded as a function of the sweeping gate bias V_{gs} . The solar cell measurement was done using a Xe lamp (Newport Inc.:AM 1.5 G filter – 1.3 suns) and Agilent 4155 Semiconductor Parameter Analyzer.

3.3 Results and Discussion

3.3.1 Growth Kinetic of CVD Graphene Synthesized on Ni Thin Films and Cu Foils

Optical microscopy inserted in the figure 3.2 shows the single, bi-layer and few-layer graphene regions from Ni thin film, which are proved in the Raman spectra exhibited in figure 3.2. Usually, the grown graphene on Ni thin film shows non-uniform different layers of graphene because of the large carbon solubility in nickel.

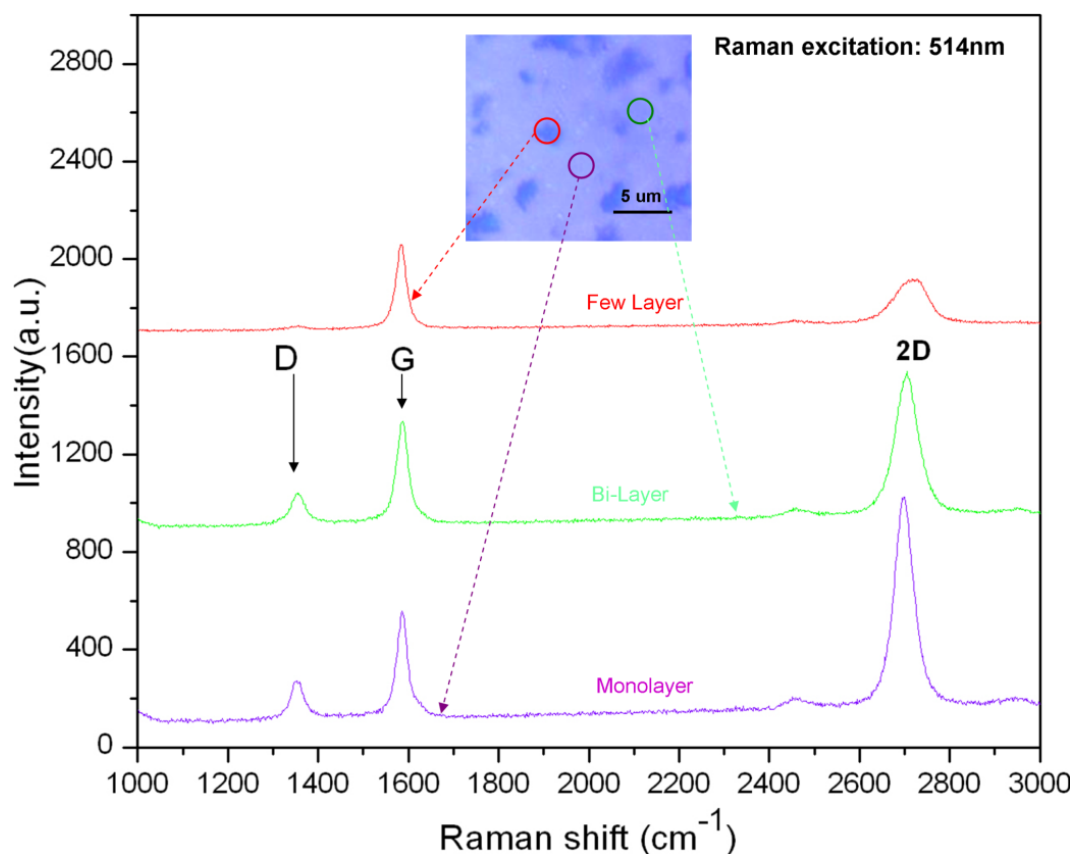


Figure 3.2 Raman spectrums of monolayer, bi-layer and few-layer CVD grown graphene on Ni thin film. Individual spectra correspond to spots indicated on the graphene layer (inset optical micrograph), in which the darker spots represent thicker graphene layers. Excitation wavelength is 514 nm.

The typical morphology of graphene layer is shown in TEM and AFM images (see figure 3.3). The variance in film thickness is indicated with AFM imaging. The height of section extracted from the AFM image along the layer edge indicates that the thickness of the graphene layer is around 1.5nm corresponding to few layer graphene. Electron pattern inserted in the TEM image proves few-layer graphene region.

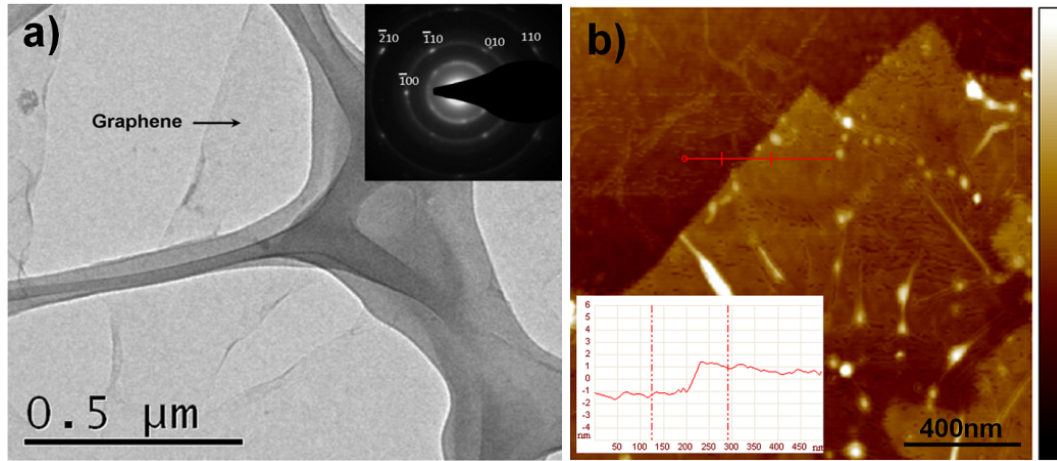


Figure 3.3 (a) Transmission electron micrograph of a few-layer graphene area grown from nickel thin film and the corresponding electron diffraction pattern. (b) AFM image of a selected few-layer graphene region, color scale bar is 10nm. The inset figure shows the height measurement on the position indicated by the red line. The measured height is around 1.5nm indicating the presence of less than 5 graphene layers.

Other than synthesizing graphene on Nickel thin film, we synthesized graphene films using copper foils as the catalysts. To investigate the growth kinetic in CVD synthesis of uniform large-area graphene layers on copper foils, we employed different growth pressures while keeping other factors the constant. The detailed experimental methods are described in the synthesis section and in the following table 1. The quality

and thickness uniformity of graphene were characterized with optical microscopy and Raman spectroscopy exhibited in figure 3.4. Comparing the optical images from a to f, we can see that graphene synthesized at the high pressure (160 Torr) shows large-area multilayer region with over 10 layers (figure 3.4a). When the growth pressure decreases, multilayer region becomes smaller and the single layer domain increases (from figure 3.4b to 3.4d). By further lowering the growth pressure to 2 Torr, the single layer graphene up to 95% of the whole surface was achieved (figure 3.4f). These results indicate that graphene growth using Cu catalysts is not purely self-limiting as reported in the reference[53]. As we know, of the entire growth kinetics cooling rate is also very important fact. Researchers successfully synthesized the uniform bi-layer graphene by controlling the cooling rate[157]. The fact that that thickness or quality of the graphene layers grown from Cu foil highly depends on the growth pressure implies that by further controlling the growth pressure and the cooling rate the uniform few-layer (3-10 layers) graphene films with high quality could be achievable.

Table 1 Graphene samples synthesized using copper foil at various pressures under constant growth temperature and constant gas composition.

	Annealing Pressure (Torr)	Growth Pressure (Torr)
S1	40	160
S2	20	80
S3	10	40
S4	2.5	10
S5	0.5	2.0

***Note:** In all of the experiments, annealing temperature and growth temperature are 1000 °C. Gas composition of H₂ and CH₄ is 1:2 (30:60 sccm).

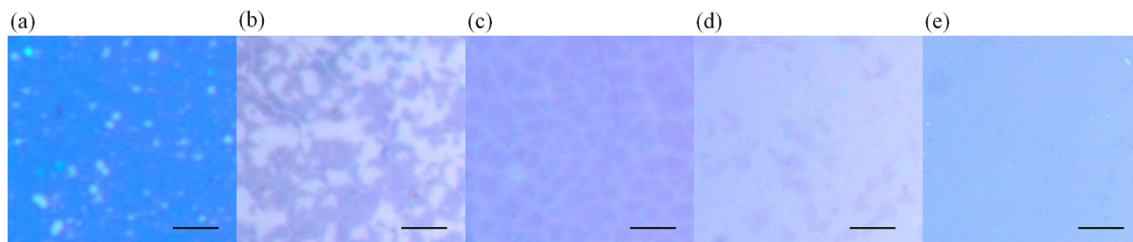


Figure 3.4 Optical images and the corresponding Raman spectra of transferred graphene (from copper) on 300 nm SiO₂ synthesized under different growth pressures (shown in table 1) using Cu as a catalyst at the same methane gas compositions and growth temperature: (a)S1; (b)S2; (c)S3; (d)S4; (e)S5. Scale bars: 10 μ m.

Raman analysis on the graphene layer grown under different growth pressure was performed to study the defect states or quality of graphene layer. The Raman spectra shown in figure 3.5a and 3.5b were collected from multilayer domains (sample S1 and S2). The convolution of G and 2D peak proves that they were multilayer graphene. As the growth pressure decreased, the defect states (see D peak) decrease (see figure 3.5c, d, e), which indicates that the growth pressure plays important kinetic in the quality of graphene. And the shape of 2D peak and the ratio of 2D to G peak show that the graphene grown under S5 condition readily shows single layer graphene which composes the 95% of the total area.

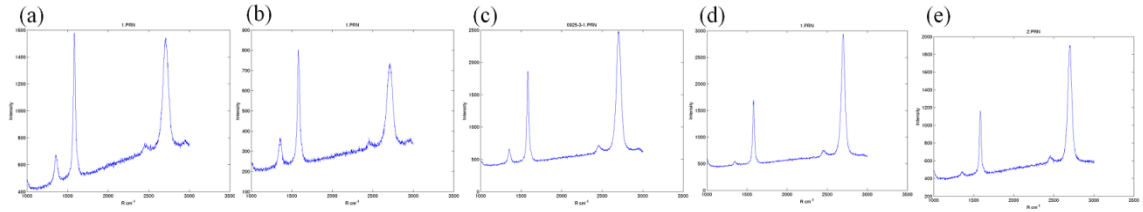


Figure 3.5 The corresponding Raman spectra of transferred graphene (from copper) on 300 nm SiO₂ synthesized under different growth pressure (shown in table 1) using Cu as catalyst at the same methane gas compositions and growth temperature: (a)S1; (b)S2; (c)S3; (d)S4; (e)S5. Excitation: 514 nm.

Using the same developed method as the sample S5, 95% monolayer graphene film with high quality can be synthesized (shown in figure 3.6a). By stacking the single layer graphene films to form few layer graphene films the sheet resistance can be decreased. For the industrial application of graphene as transparent electrode the sheet resistance has to be less than 100 ohm/sqr with at 90% optical transmittance. The evolving optical transmittance spectra of graphene layer films that are transferred using layer to layer stacking are shown in figure 3.6b. The optical transmittance of single layer graphene is around 97.9%. The transmittance decreases around 2.1%~2.3 % with one additional layer[4]. With four stacking layers the optical transmittance is around 90%.

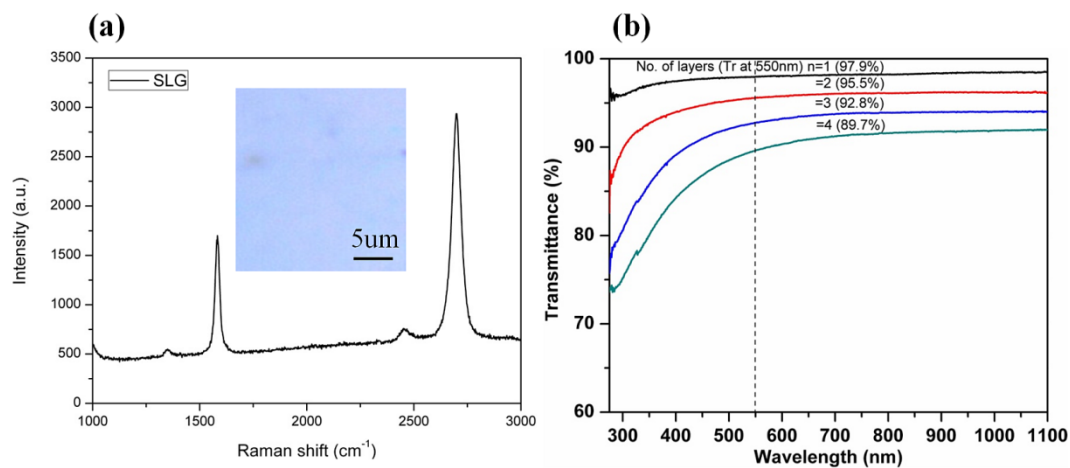


Figure 3.6 (a) Raman spectra indicating single layer graphene grown on copper foil by CVD process using the same conditions as S5. Excitation laser: 514 nm. Inset is the optical image of monolayer graphene on Si substrate with 300nm SiO₂. (b) Optical transmittance of layer by layer transferred graphene films on quartz substrates.

3.3.2 Organic Solar Cell Based on Few-layer Graphene

The sheet resistance with 90% optical transmittance and the surface wettability of graphene thin films are critical in application as transparent electrodes in organic solar cell. Usually sheet resistance of single layer graphene film with size of 1 inch developed in our group is around 1.5K ohm/sqr. By employing the layer to layer transfer technique adding one more layer of graphene the sheet resistance will decrease by around 25% (see figure 3.7a). With four-layer pristine graphene the sheet resistance is around 800 ohm/sqr. Employing different chemicals like HNO_3 [51] or AuCl_3 [55] can dope the graphene films. Here we employed highly concentrated HNO_3 to decrease the sheet resistance of graphene films (shown in figure 3.7a). After HNO_3 treatment the sheet resistance of 1-4 layer graphene respectively decreases by 30%. Other than that, we found out that the contact angles of 1-4 layer graphene films respectively decrease (see figure 3.7b), which indicated that the surface energy of graphene decrease after HNO_3 treatment. HNO_3 treatment improves the surface wettability of graphene layers. The hydrophilic interface may improve the adhesion between the organic polymer and the graphene[47].

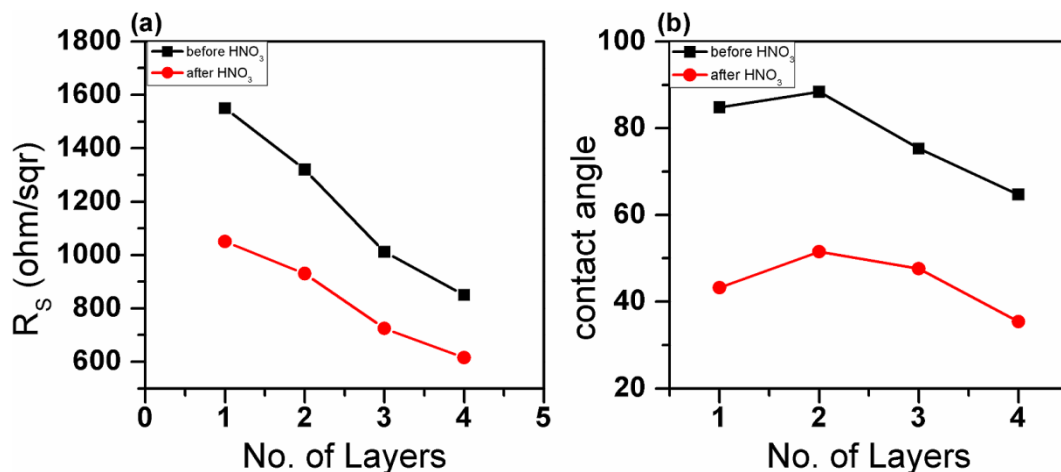


Figure 3.7 The effect of highly concentrated HNO₃ on the sheet resistance and surface energy of graphene films with different number of layers. (a) Sheet resistance R_s of graphene films before and after HNO₃ treatment. (b) Contact angle of graphene films before and after HNO₃ treatment.

Figure 3.8a shows the device structure of organic solar cell based on graphene anode. From the energy diagram exhibited in figure 3.8b we can see that with light illumination the hole/electron pairs that are excited from active bulk-heterojunctions of P3HT and PCBM are separated. Then electrons diffuse to Li/Al electrode and the holes diffuse to graphene anode. And the buffer layer PEDOT:PSS with work function of 5.0eV lowers the hole-injection barrier between graphene anode (4.5eV) and P3HT (5.0eV), which enhances the holes collection in graphene anode. I-V characteristic of the photovoltaic cell based on graphene anode is shown in figure 3.8c. The solar cell had open-circuit voltage (V_{oc}) of 0.62V, a short-circuit current density (J_{sc}) of 0.11mA/cm² and a filling factor (FF) of 28%. The overall PCE was around 0.12%. From the I-V characteristics (shown in the inset of figure 3.8c) of ITO-based organic solar cell the PCE usually could

reach higher than 3.5%. The lower PCE in graphene-based organic photovoltaic cell can be attributed to major two reasons: relatively higher sheet resistance and the lower surface wettability of graphene. The four layer graphene films employed for the anode had resistance have sheet resistance of around 650 ohm/sqr after HNO₃ treatment. Although after HNO₃ treatment the surface wettability improved, still it showed high surface energy state based on the contact angle measurement. In order to improve the PCE of graphene-based solar cell, we suggest improving the conductivity of graphene films by optimizing the growth conditions (growth pressure and cooling rate) to synthesize uniform few-layer graphene and the surface wettability using other interfacial engineering like functionalization with other chemicals[47, 158].

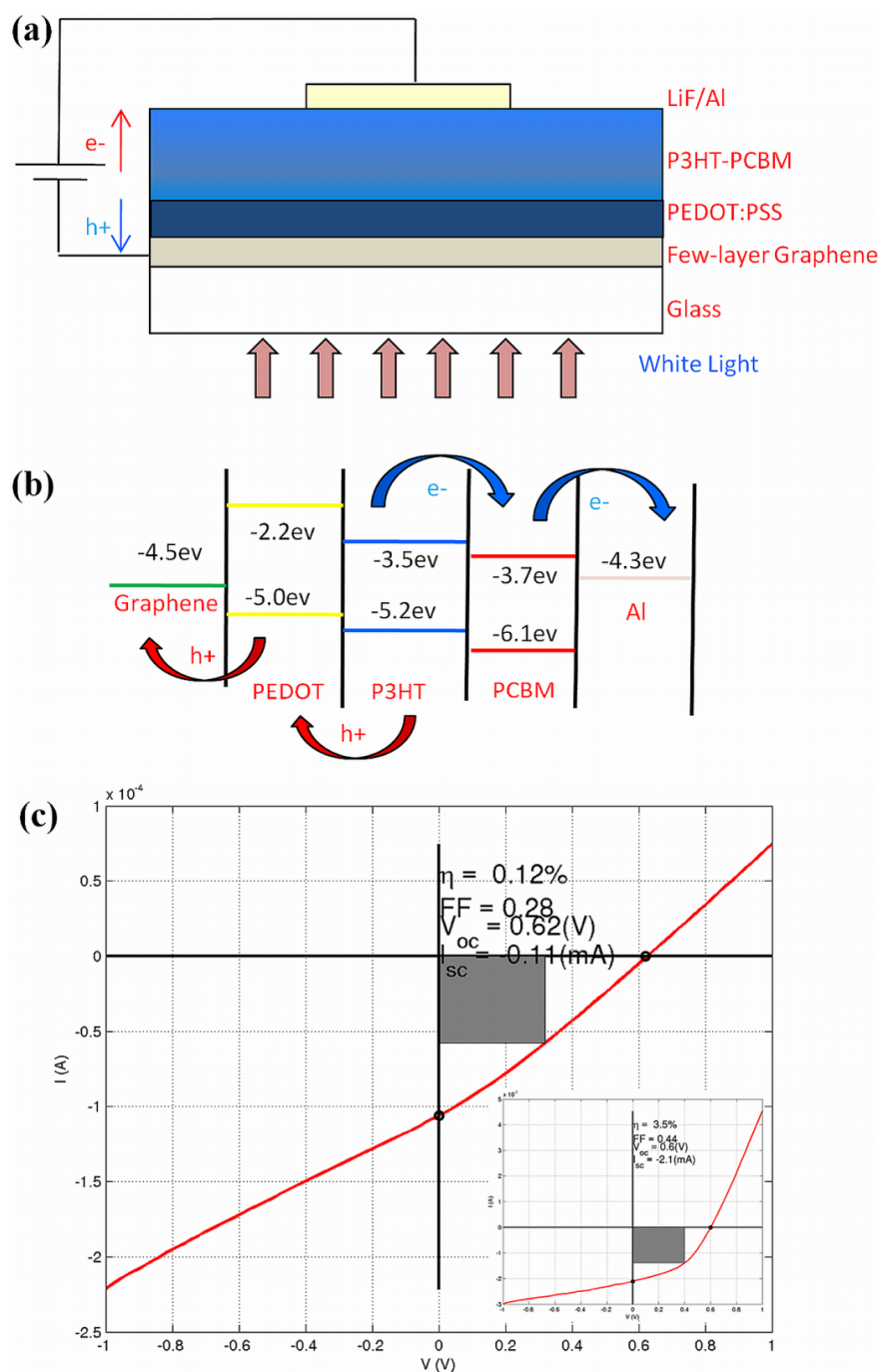


Figure 3.8 (a) Schematic of organic solar cell with four-layer graphene films as transparent and conductive electrode. (b) Energy diagram of the solar cell device with structure: graphene/PEDOT:PSS/P3HT:PCBM/LiF/Al. (c) I-V characteristic of four-layer graphene film based organic solar cell. Inset is the I-V characteristic of organic solar cell using ITO as electrode.

3.4 Conclusion

The graphene layers are synthesized both on Ni thin film as well as on Copper foil by CVD process. The uniformity of graphene films grown from Ni is more difficult to control than the one grown from copper foils. Material characterizations indicate that the number of graphene layers synthesized on Nickel thin film is between 1-5 layers. While, under low pressure growth pressure graphene film with 95% coverage of single layer is achieved. Further by controlling the growth pressure 1-10 layers graphene could be synthesized, which suggests that this process is not purely self-limiting as reported in the reference. The fact that that thickness or quality of the graphene layers grown from Cu foil highly depend on the growth pressure implies that by further controlling the growth pressure and the cooling rate the uniform few-layer (3-10 layers) graphene films with high quality could be achievable.

Sheet resistance and surface wettability play very important roles in the PCE of organic solar cell. Compared with ITO-based organic photovoltaic solar cell, the fabricated graphene based solar cell exhibits relatively lower power conversion efficiency (PCE). To improve the PCE of graphene-based organic solar cell, we suggest some approaches like synthesizing the uniform few-layer graphene film with high quality using Cu catalysts by controlling the growth conditions (growth pressure and the cooling rate) and improving the surface wettability by interfacial chemical engineering. This chapter demonstrates that graphene provides the promising application in optoelectronics.

Chapter 4 Synthesis of Pillar Graphene Nanostructures and its Application in Supercapacitor

Reprinted in part with permission from [Rajat Kanti Paul, Maziar Ghazinejad, Miroslav Penchev, Jian Lin, Mihrimah Ozkan, Cengiz Sinan Ozkan. “Synthesis of pillared graphene nanostructure: a counterpart of three dimensional carbon architecture”, Small, 2010, 6(20): 2309-2013]. Copyright Wiley. Reproduced with permission.

Abstract

In this chapter, we report the fabrication of high conductive and large surface-area 3D pillar graphene nanostructures (PGN) films from assembly of vertically aligned CNT pillars on flexible copper foils and directly employed for the application in EDLC supercapacitor. The PGN films which are one-step synthesized on flexible copper foil (25 μm) by CVD process exhibit high conductivity with sheet resistance as low as 1.6 ohm per square and high mechanical flexibility. Further, Raman spectra indicate the multi wall carbon nanotubes (MWCNTs). The morphology of MWCNTs can be controlled by growth conditions. In addition, we find out that nitric acid treatment can significantly increase the capacitance due to the increase of surface wettability. The fabricated EDLC supercapacitor based on high surface-area PGN electrodes ($563\text{m}^2/\text{g}$) shows high performance with high specific capacitance of 330F/g extracted from CV curve at scanning rate of 100mV/s. The energy density is as high as 45.8Wh/kg. All of these make this 3D graphene/CNTs hybrid carbon nanostructures highly attractive material for high performance supercapacitor and other energy storage material.

4.1 Introduction

Ultra or supercapacitor based on electrochemical double layer capacitor (EDLC), consisting of the porous electrodes in the electrolyte solution that stores or releases the energy among the electrode/electrolyte interface, has been widely explored in the past 30 years[56]. Since then, active carbon materials with high surface area are employed as electrodes[159]. At the nanoscale, as one type of the carbon materials, carbon nanotubes (CNTs) have been widely applied in electrochemical energy storage[160-165]. The newly discovered 2D carbon material, graphene, has individually intrigued dramatic attentions for the various applications in biosensor[152], transparent electrode for solar cell[49, 50], and supercapacitor[57, 58, 61]. Recently, assembling 1D CNTs and 2D graphene to form 2D or 3D hybrid carbon nanostructures has been theoretically[166]and experimentally[102, 111, 167-169] reported. Owing to the unique crystal structures, the low contact resistance between graphene and CNTs, high surface areas, remarkable chemical stability these graphene/CNTs hybrid carbon nanostructures show promising applications for supercapacitor[102]. However, this reported supercapacitor's electrodes are fabricated from spincoating of CNTs on graphene surface, which may reduce the total surface areas and conductivity of graphene/CNT hybrid nanostructures at the same weight scale. Among these peers' great works in this research field our group recently has demonstrated the successful synthesis of controlled 3D pillar graphene nanostructures (PGN) comprising vertically aligned CNT pillars on large-area graphene layers[112]. These unique nanostructures are one-step synthesized on copper catalyst thin film by chemical vapor deposition (CVD).

4.2 Material Synthesis and Experimental Methods

4.2.1 Material Synthesis

PGN were synthesized directly on 25 μm copper foils (Alfa Aesar, 99.8%) by chemical vapor deposition. The experiment began with thermal annealing of copper foil at 900 $^{\circ}\text{C}$ in flowing Argon of 100 sccm and H_2 of 100sccm for 30minuts to crease the grain sizes, followed by evaporation of 4 nm thick Fe catalysts on copper foils using an e-beam evaporator (Temescal, BJD-1800). Then the copper foils with catalysts were loaded in the center of furnace tube and heated to 750 $^{\circ}\text{C}$ with flowing of 150sccm Ar and 150 sccm H_2 under the ambient pressure. Once the temperature was stabilized at 750 $^{\circ}\text{C}$, 30-50 sccm C_2H_2 is introduced into the tube for 20 minutes to synthesize PGN. After the synthesis C_2H_2 was turned off and the furnace was slowly cooled to room temperature. For the transferring process the PGN layer was etched in 1M $\text{Fe}(\text{NO}_3)_3$ solution, followed by cleaning in 5% HCl solution and DI water, then was transferred to different substrates like SiO_2/Si and PDMS for further characterizations. Photolithography was performed using a patterned mask having circular window patterns to define the location of Fe catalyst, followed by mild O_2 -plasma etching to remove any residual resist, and 5 nm thick Fe deposition by electron-beam evaporation. Then the PGN were grown following the previous stated method.

4.2.2 Experimental Methods

Material characterizations. The morphology of synthesized PGN was characterized with scanning electron microscopy (SEM; Leo, 1550) and a field emission source and

transmission electron microscopy (TEM; Philips, CM300, Japan) with a LaB6 cathode operated at 300kV and equipped with an X-ray energy-dispersive spectroscopy (EDS) module. To measure the sheet resistance of CNT pillars, four Ni/Au (20/80 nm) tiny circle contacts with size of 100um were deposited on top of CNT pillars by using e-beam evaporator (Temescal, BJD-1800). The weight of PGN films was measured by weighing the difference of copper foils before and after growth of PGN films per 1cm^2 with microbalance of Thermogravimetric Analyzer (TGA, Q500, TA instrument). The BET surface area was measured using Micromeritics 2020. The change of sheet resistance of PGN films were measured by bending the PGN films transferred to PET substrates. The electrical measurements were conducted in programmable Agilent 4155C. A Renishaw DXR Raman Microscope with a 532nm laser source was used to characterize PGN. The backscattered light from graphene samples was collected through optical microscopy with 100x objective lenses. The excitation power employed was 8mW. And Kruss Easy drop (FM 40) was employed to measure the contact angle of PGN films.

Double layer supercapacitor fabrication and electrochemical measurement. Two electrode test cell was fabricated in the following way. Two PGN films on 25 um copper (99.8%) are attached onto glass slides. Coppers act as current collectors and PGN films act as active electrodes. The active areas overlapped the PGN electrodes is 1 cm^2 . Before the test cell assembly the two electrodes were functionalized by HNO_3 /IPA solution (67% HNO_3 : IPA=1:4). Then both glass slides with PGN film electrodes attached were assembled with a separator (Celgard 3501) sandwiched in between. The separator was soaked with 2M aqueous Li_2SO_4 . Then they are assembled with parafilm wrapped around.

The extended current collectors were connected to an electrochemistry cell (Gamry reference 600) for the CV measurement. And the cell assembly and all the measurement were implemented in Ar filled glove box (VAC Omni lab, oxygen and water contents below 1ppm and 1 ppm respectively) under the room temperature. CV curves were scanned at voltage ramp rates of 100mV/s, 200mV/s with range of 0-1 V.

4.3 Results and Discussion

4.3.1 Material Characterizations of PGN

Figure 4.1a is the optical micrograph of one PGN film grown on copper foil. The PGN films were grown on the portion of the copper foil where 4nm Fe thin film was evaporated (indicated in the dark black part). Figure 4.1b shows the large-area PGN films floating in $\text{Fe}(\text{NO}_3)_3$ solution after detachment from copper foil. The transparent graphene layers and the dark black PGN film are clearly distinguishable. In addition, during etching and transferring process no noticeable bulk crack or defects were observed indicating that the PGN films are highly flexible. Further the structure morphology of PGN films were characterized with scanning electron microscopy (SEM). Figure 4.1c is the top view of SEM image of PGN, which shows the tangled and spaghetti-like CNTs network feature. The diameters of CNT pillars are ranging from 5nm to 15nm, which indicates the formation of multi-wall carbon nanotubes (MWCNTs) (shown in the inset of figure 4.1c). The 45° side view of PGN is shown in figure 4.1d, from which we can clearly observe the vertical aligned CNT pillars with uniform morphology over graphene layers. What's more, CNT pillars are so high-densely packed that the inter-tube gap can

be not observed. The height of CNT pillars is around 20 μm , which can be easily controlled by controlling the duration of growth and the flow rate of source gases (C_2H_2). The weight of typical PGN films with 20 μm thick is measured to be around 90 $\mu\text{g}/\text{cm}^2$. The Brunauer – Emmett – Teller (BET) surface area, determined by N_2 absorption isotherms, is estimated to be 563 m^2/g . This value is comparable to the reported ones in CNTs (400 m^2/g [170]) or reduced graphene flakes (320 m^2/g [58] and 705 m^2/g [57]).

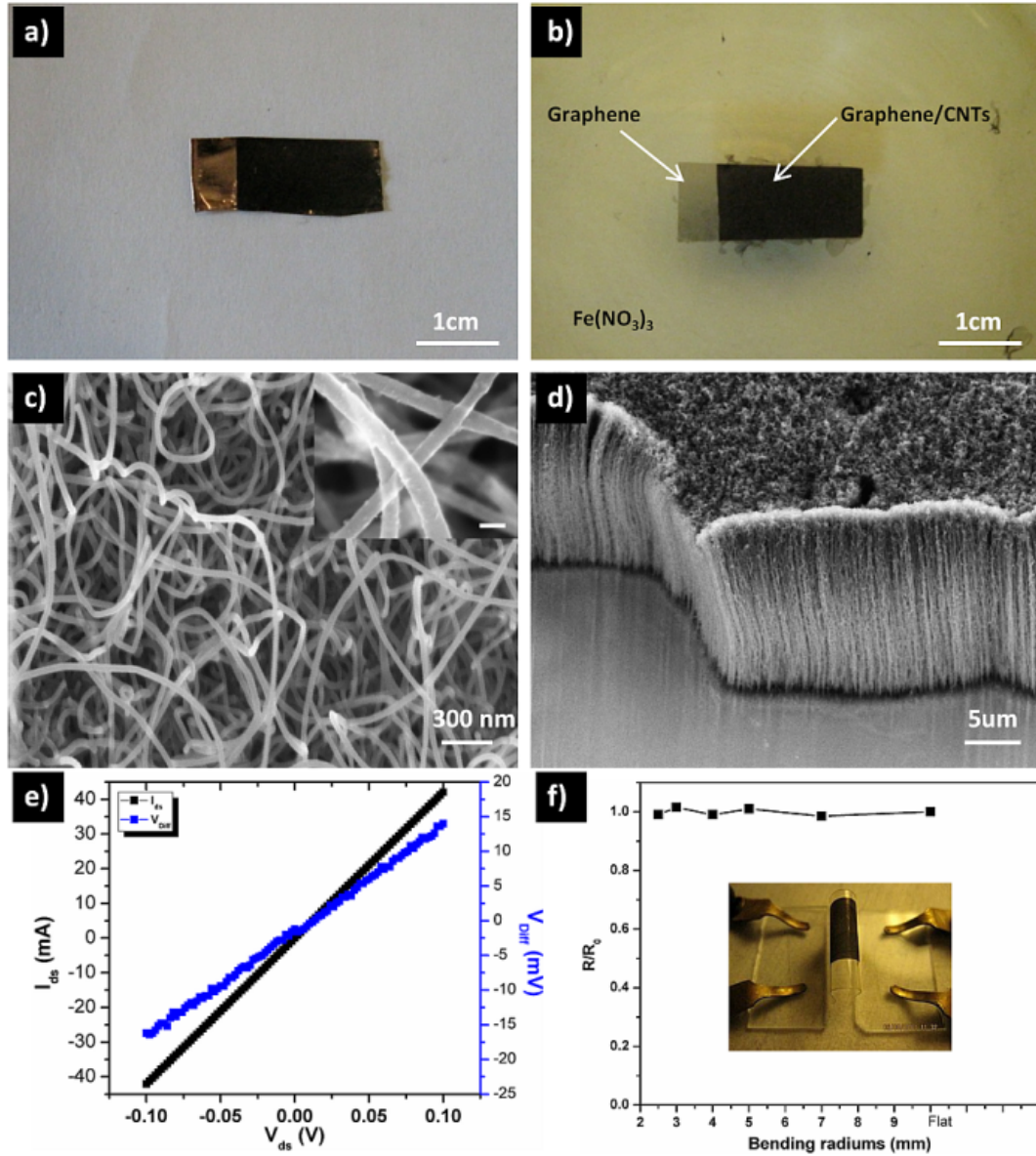


Figure 4.1 (a) Optical micrograph of PGN grown over copper foil. (b) Optical micrograph of PGN film floating in the aqueous $\text{Fe}(\text{NO}_3)_3$ solution. (c) Top-view SEM image of PGN film. Inset is the top-view high magnification SEM of PGN (scale bar: 10 nm). (d) 45° side-view SEM image of PGN film. (e) Two probe and four probe I-V characteristic of PGN film. Sheet resistance: $R_s = (\pi / \ln 2) \times (V_{diff} / I_{ds})$. (f) Sheet resistance change of PGN film transferred on PET substrate under various bending radius. Inset shows the bending experiment setup.

Overall, these morphologies of CNT pillars having tangled network on the surface and vertical bundles underneath can significantly reduce the sheet resistance of PGN films, which is proved from sheet resistance measurement by Van der Pauw method. The measured sheet resistance reaches as low as 1.6 ohm/sqr from I-V curve shown in figure 4.1e. It is well known that CNTs or graphene films have excellent mechanical flexibility, respectively[52, 164]. Here we measured the variance of sheet resistance by bending the PGN film transferred to polyethylene terephthalate (PET) substrate coated with a thin layer of poly-dimethylsiloxane (PDMS). The resistance shows little variance when bending radius is up to 2.5 mm (shown in figure 4.1f). This excellent mechanical flexibility can satisfy the requirement for the application in energy storage devices.

Furthermore, our developed technique allows the controlled growth of CNT pillars and graphene at particular locations and with desired geometries simply depending on the design of the catalyst (such as Cu and Fe) patterning. Figure 4.2a demonstrates the direct CVD growth of a patterned PGN using a pre-patterned 5nm thick Fe catalyst dot array on Cu film. Figure 4.2b shows SEM micrographs of patterned PGN grown at 750°C for 5min. This is a significant addition to the capabilities for PGN device fabrication and integration. For example, in the case of O₂ plasma-sensitive substrates, PGN devices can be patterned using the approach described in material synthesis method. The height of the CNT pillars was about 5μm with a 5 min growth time. Figure 4.2 (c, d) shows large-area patterned PGN on quartz and SiO₂/Si using a similar procedure to transfer large-area PGN.

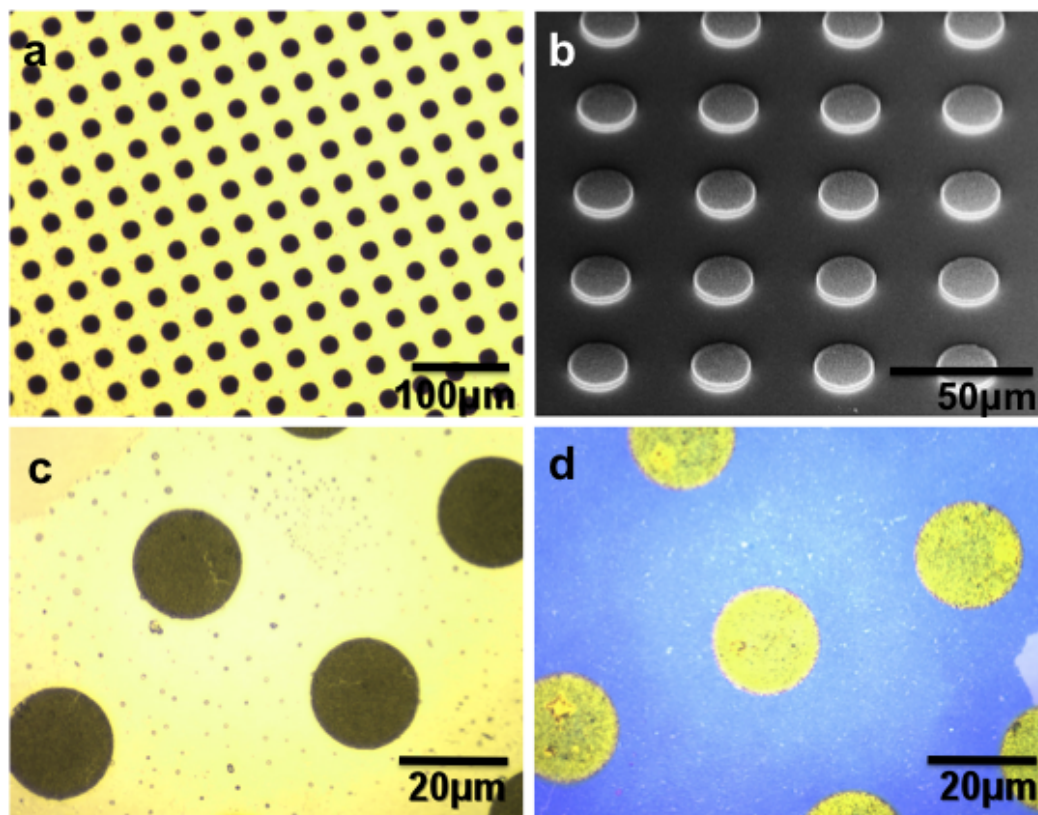


Figure 4.2 (a) Optical micrograph of micropatterned large-area PGN grown at 750°C for 5min. (b) SEM micrograph of PGN showing highly aligned CNT pillars on graphene film. (c, d) Optical micrographs micropatterned PGN in (a), transferred on quartz and SiO₂/Si, respectively.

Raman spectroscopy was employed to characterize the different positions of the PGN films. Figure 4.3a is the Raman spectra recorded from the transparent graphene region (see from the figure 4.1b). The presence of D band at 1360 cm⁻¹, G peak at 1581 cm⁻¹, G' peak at 2709 cm⁻¹ and the ratio between G peak and G' peak shows the typical Raman characteristics for few-layer graphene (FLG), which is similar to the reported CVD graphene[52, 54, 113]. The Raman spectra shown in figure 4.2b were collected from the

dark area representing the CNT pillars. Unlike the splitting G+ and G- for the single wall carbon nanotubes (SWCNT) the predominant G peak located at 1582 cm^{-1} is usual the result of MWCNTs with large and various diameters[171]. And absence of RMB Raman feature associated with small diameter tube (less than 2nm) further confirms that the grown CNT pillars are dominantly MWCNTs. The appearance of D band is associated with the defects of MWCNTs.

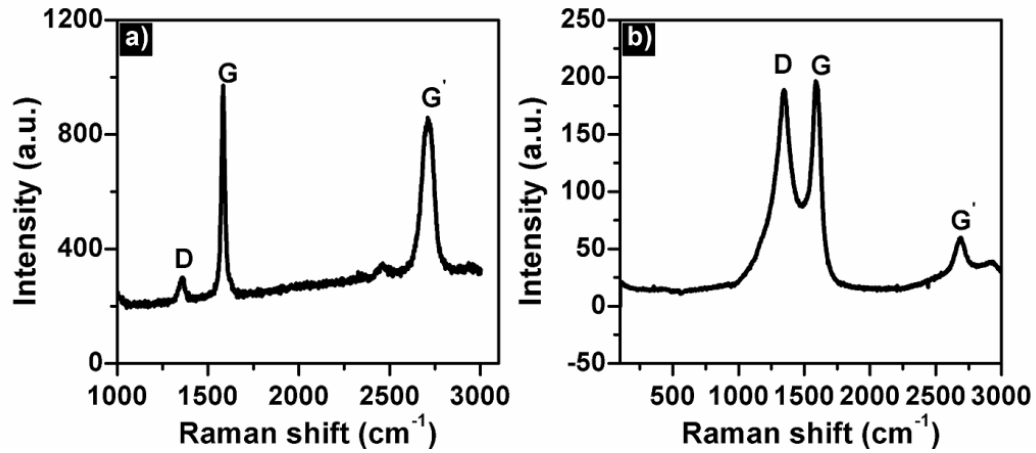


Figure 4.3 (a) Raman spectra of few-layer graphene region. (b) Raman spectra of PGN film from CNT pillars region. The excitation laser: 532 nm.

In order to understand the detailed material structure and morphology of PGN films, we implemented material characterization with TEM. Figure 4.4a shows TEM micrograph of bottom view of patterned PGN suspended on lacey carbon supported TEM Cu grid. The patterned PGN is clearly visible on the graphene surface. However, wrinkles and bulk defects (as shown with arrowheads) were appeared on the graphene film due to the thermal expansion coefficient mismatch between Cu and graphene, and the hollow

structure of the Cu TEM grid. Figure 4.4b shows enlarged TEM micrograph of the bottom view of the PGN. This is a significant observation of the interface between CNT pillars and graphene of the PGN. The individual CNT's root is directly connected to the graphene surface. The circular hollow patterns in the interface of a CNT and graphene layer are clearly visible as shown with the dashed circles in Figure 4.4b. The inset electron diffraction pattern in Figure 4.4b consists of concentric rings which are expected since multiwalled carbon nanotubes are concentric tubes of cylindrically rolled graphene layers. The embedded typical six-fold symmetrical spots are made possible due to the mono- or bi-layer graphene film. Figure 4.4c shows HRTEM micrograph of the interface between a CNT and graphene. The clear lattice fringe on the interface confirmed seamless crystalline interface between the two carbon allotropes. This observation could lead PGN to be directly utilized in several applications especially in interconnects, electrodes for super-capacitor and field-emitting device technology. The inset EDS spectrum in Figure 4.4d taken from Fe catalyst particle on the tip of a CNT (dashed circle) confirms the existence of C, Fe and Cu elements. The Cu peak appears due to the TEM Cu grid used for holding the PGN. TEM observations also reveal the growth mechanism of CNT pillars on the graphene layer through a vapor-liquid-solid mechanism.

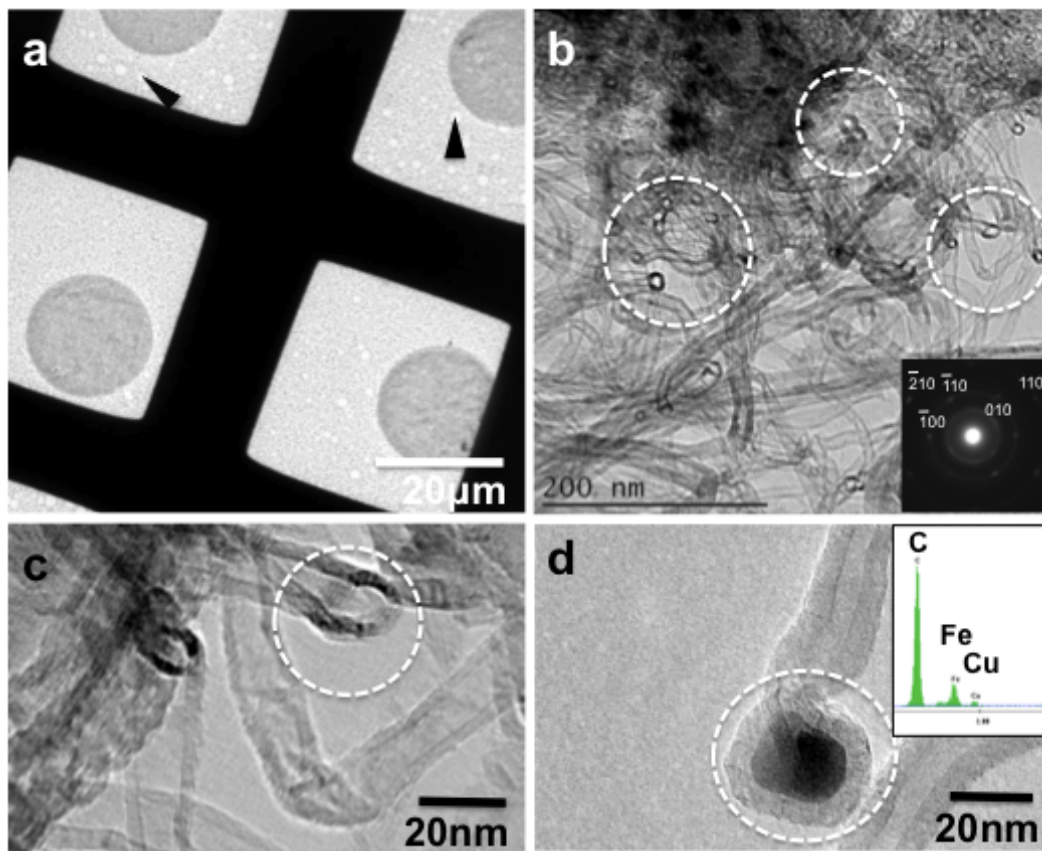


Figure 4.4 (a) Low magnification TEM micrograph of micropatterned large-area PGN suspended on lacy carbon supported TEM Cu grid. (b) TEM micrograph of PGN (bottom view) showing crystalline integrity of individual CNT's root (dashed circles) with the surface of the graphene film. HRTEM micrographs of suspended PGN taken from (b), showing individual CNT's root (c) and tip (d) regions.

4.3.2 Supercapacitor Based on Flexible Pillar Graphene Nanostructures

PGN films with high surface area and high conductivity are potential candidate as electrodes for supercapacitor. The electrode-electrolyte interaction is an important topic supercapacitor. The electrolyte adsorption to electrode pores, especially the organic electrolyte with bigger molecular weight, is highly affected by the surface wettability of electrodes[63]. Researchers employed varied functional groups to enhance surface wettability to increase the specific capacitance through improved electrolyte access to pores and greater surface utilization[172]. To study the effect of surface wettability to the specific capacitance we used HNO₃/IPA solution (67% HNO₃: IPA=1:4) to functionalize the PGN surface. After the acid treatment the contact angle is decreased by 54.2° (see figure 4.5a and 4.5b), which indicates the surface wettability is enhanced. As shown in the insets of figure 4.5a and 4.5b, the functionalization does not result in any visibly buck defects or amorphous carbon. The fabricated test cell comprising two copper foils with PGN films covered and separator is exhibited in figure 4.5c. Base on the cyclic voltammetry (CV) curves shown in figure 4.5d, the specific capacitance of PGN films after functionalization increases from 111F/g to 330F/g at scanning rate of 100mV/s, calculated from the CV curves using equation (4.1):

$$C_s = \frac{\int idV}{2 \times m \times \Delta V \times S} \quad (4.1)$$

Where C_s is the specific capacitance (expressed per gram, F/g), $\int idV$ is the integrated area of CV curve, m is the weight of one PGN film electrode (expressed g/cm²), ΔV is potential range, and S is the scanning rate. We believe that the increase of specific

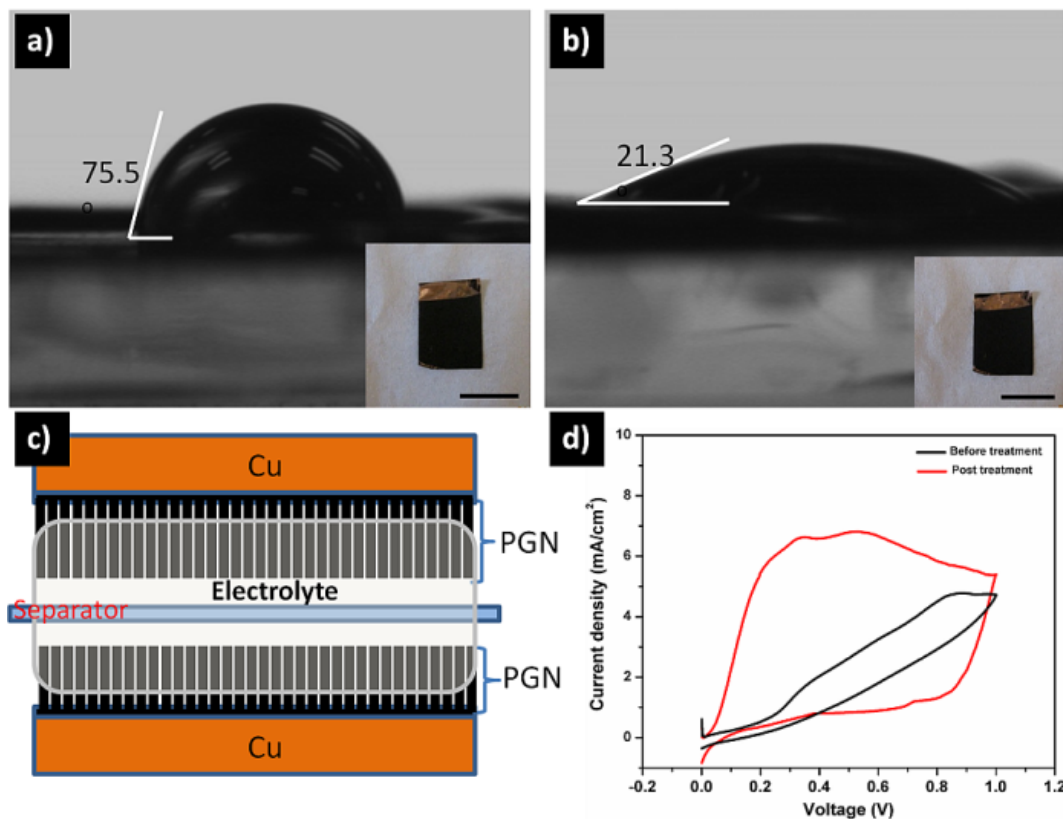


Figure 4.5 (a) Contact angle of PGN film before acid treatment. (b) Contact angle PGN film after acid treatment. Insets in a) and b) are the comparison optical micrographs of PGN films before and after acid treatment. (c) Schematic of test cell assembly. (d) CV curves of supercapacitor based on PGN films without and with acid treatment. The scanning rate is 100mV/s. The weight of one PGN film is 90ug/cm².

capacitance is due to two facts: nitric acid enhances the surface wettability of PGN[173], also increases the surface area by means of end-tip opening of MWCNTs through etching Fe catalysts. This makes the electrolyte easily access the pores, which may decrease the internal resistance[170, 174]. The conversion of oblique angle CV curve to near rectangle shape results from the decrease of internal resistance[163]. And the reason of relatively higher specific capacitance than 2D graphene/CNTs film made from spincoating of CNTs

on reduced graphene oxide[102] or the graphene flakes based supercapacitor[57, 58, 61] is that the vertically uniformly-spacing aligned CNTs have unique mesoporosity which provides more effective surface area for electrolyte access into the pores[170]. Base on the specific capacitance the energy density of supercapacitor is calculated to be 45.8 Wh/kg using the equation (4.2):

$$E = \frac{1}{2} C_s (\Delta V)^2 \quad (4.2)$$

Where E is the energy density, C_s is the specific capacitance ($C_s = 330\text{F/g}$), ΔV is potential range ($\Delta V = 1\text{V}$).

To further characterize the performance of PGN films-based super capacitor we implemented CV measurement on supercapacitor based on copper foils, CVD grown graphene layers on copper foils and PGN films on copper foils respectively. As expected, the major material part in PGN architectures contributing to the energy storage is MWCNTs. The capacitance of copper foils and graphene layers on copper foils is negligible compared with PGN based supercapacitor (see from figure 4.6a). The reason of low capacitance from graphene layers based capacitor is that the surface area of graphene films grown by CVD method is very low compared with reduced graphene flakes. The role of graphene in the PGN architectures, we believe, is that graphene acts as buffer electrode connected to copper foils. As stated, the ion diffusion length plays important role in the sensitivity to the varying scan rate[57]. In figure 4.6b, as the scan rate increases from 100mV/s to 200mV/s, the specific capacitance of PGN supercapacitor is decreased, which indicates long diffusion path length of ions in the electrolyte due to

electrolyte penetrating into the spacing of vertical aligned MWCNTs. This ion diffusion into the interiors of MWCNTs would result in various diffusion lengths and the obstacle of ion movement at high scanning rate.

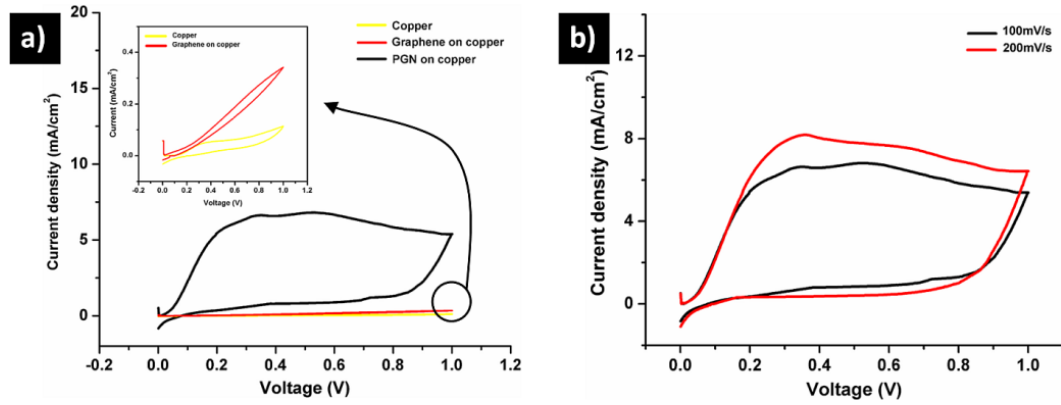


Figure 4.6 (a) comparison CV curves of capacitors based on copper foils, graphene layers on copper foils and PGN films on copper foils. Scanning rate: 100mV/s. inset is the zoom-in CV curves of capacitors based on copper foils and graphene layers on copper foils. (b) CV curves of supercapacitor based on PGN films at scanning rate of 100mV/s and 200mV/s.

4.4 Conclusion

A novel three dimensional architecture named pillar graphene nanostructures consisting of high dense and vertical aligned MWCNTs on large-area graphene layer are synthesized on flexible copper foil. Optical microscopy (OM), scanning electron microscopy (SEM), transmission electron microscopy (TEM) and high-resolution transmission microscopy (HRTEM) techniques show that high quality PGN films. The excellent mechanical flexibility and electrical property make PGN a potential candidate for the application in energy storage. The fabricated supercapacitor based on PGN electrodes shows high energy storage capability with high specific capacitance (330F/g) and high power density (45.8 Wh/kg). This unique 3D architecture for supercapacitor electrodes would provide new pathway of achieving high energy storage technology.

Chapter 5 Synthesis of Heterogeneous Graphene/ZnO Hybrid Nanostructures and Studies on Their Electrical and Photoelectrical Properties

Reprinted in part with permission from [Jian Lin, Miroslav Penchev, Guoping Wang, Rajat K Paul, Jiebin Zhong, Xiaoye Jing, Mihri Ozkan, Cengiz S. Ozkan. “Heterogeneous Graphene Nanostructures (HGN): ZnO Nanostructures Grown on Large Area Graphene Layers”, *Small*, 2010, 6(21): 2448-2452]. Copyright Wiley. Reproduced with permission.

Abstract

In this chapter, we report the synthesis and characterization of three dimensional heterostructures graphene nanostructures (HGN) comprising continuous large area graphene layers and ZnO nanostructures, fabricated via chemical vapor deposition. Characterization of large area HGN demonstrates that it consists of 1-5 layers of graphene, and exhibits high optical transmittance and enhanced electrical conductivity. Electron microscopy investigation shows that the morphology of ZnO nanostructures is highly dependent on the growth temperature. It is observed that ordered crystalline ZnO nanostructures are preferably grown along the $\langle 0001 \rangle$ direction. Ultraviolet spectroscopy and photoluminescence spectroscopy indicate that the CVD grown HGN layers has excellent optical properties. A combination of electrical and optical properties of graphene and ZnO building blocks in ZnO based HGN provides unique characteristics for opportunities in future optoelectronic devices.

Besides that, we also investigate the electrical and photoconductive properties of graphene/ZnO/graphene heterostructure. Current-voltage (I-V) measurements reveal that

most of the graphene/ZnO/graphene devices exhibit the expected linear I-V characteristics, while several of devices show Schottky characteristics. The observed relatively small photo-current gain and decreasing conductance upon the ultra violet (UV) illumination on graphene/ZnO/graphene devices can be attributed to the effect of graphene due to its high absorption in UV region and photodesorption of gas molecules. Electrical conductance of graphene/ZnO/graphene highly depends on temperature. These results provide insights into the electrical and photoconductive properties of this novel heterostructure and lay the foundations for its future utilization in device applications such as photo-detector and solar cell.

5.1 Introduction

Recently graphene based hybrid nanostructures with inorganic nanomaterials have been attracting more attention since the integrated inorganic nanomaterials provide additional functionality onto graphene layers in applications of electronics and optoelectronics[104, 168, 175-177]. Despite the recent progress made in graphene hybrid nanostructures, still only a few studies were performed at the large scale due to the limitations of graphene synthesis methods such as mechanical exfoliation [69], liquid-phase exfoliation[75], oxidation of graphite[178] and thermal decomposition of SiC[179]. Compared to these methods, chemical vapor deposition provides a promising route to synthesize uniform large-area graphene layers meeting industrial requirement[52-54, 180]. With a direct band gap of 3.37eV and a large binding energy of 60 meV as well as the piezoelectric effect, Zinc Oxide nanostructures are important one-dimensional architectures and building blocks for nano-electronics[181], optoelectronics[181-183], and nanogenerators[184, 185]. Vapor-liquid-solid mechanism has been employed to synthesize well-controlled and single crystalline ZnO nanostructures on various substrates including indium tin oxide (ITO)[182, 186], GaN[187] and AlN[188] for versatile applications. Accordingly, the growth of semiconductor ZnO nanostructures on large area graphene layers would allow the unique properties of the heterostructures to be exploited in optoelectronic device applications. Here we demonstrate the synthesis and of three dimensional heterostructures comprising large area graphene layers and Zinc oxide nanostructures. The pathway to achieve such structures is to first synthesize large-area

graphene layers via CVD, followed by the growth of ZnO nanostructures via the self-catalyzed vapor solid mechanism.

Further to promote the application of the heterogeneous nanostructures in optoelectronics, the electrical characteristics and the photoconductivity are investigated. Based on this objective, we report the fabrication of graphene/ZnO NWs/graphene heterostructure, consisting of ZnO NWs vertically grown on the top of graphene as bottom electrode and covered by the other top graphene electrode. Current-voltage characteristic in dark shows Ohmic electrical contact characteristics for majority of devices tested, with a small fraction of devices exhibiting Schottky rectifying behavior. The photoconductive property of graphene/ZnO/graphene devices is also investigated by the illumination of UV to evaluate their potential in optoelectronic application. Lastly, the conductance highly depends on the temperature, which was shown by measuring the I-V characteristics at different temperature from 300K to 400K.

5.2 Synthesis of Graphene/ZnO Hybrid Nanostructures

5.2.1 Material Synthesis and Experimental Methods

Material Synthesis by CVD: In the CVD process, few-layer large area graphene layers were grown on thin Ni catalyst films using highly diluted methane gas source at 900°C under ambient pressure conditions in a tube furnace. 250nm thick Ni catalyst films were deposited on Si/SiO₂ substrates using electron beam evaporation. Ni deposited samples were heated to 900°C in a Ar/H₂ (600:500 standard cubic centimeter per minute-sccm) atmosphere and annealed for 30 minutes in order to form a polycrystalline Ni film with large average grain size[54]. After flowing methane (30sccm) mixed with Ar/H₂ at 900°C under ambient pressure for 1 minute, the furnace was cooled down to 25°C at a medium/fast cooling rate of 10°C/s. Next, the residual Ni layer underneath was etched in mild HCl aqueous solution (3%). Then the graphene layer was transferred onto a Si/SiO₂ substrate or quartz plate for further characterization and processing. Next, Single crystal ZnO nanostructures were synthesized on these graphene layers in a different tube furnace. Zinc powder (Sigma-Aldrich, purity 99.9%) was placed inside a small quartz tube from which the SiO₂/Si substrates or quartz plates with overlying graphene layers were placed nearly 10cm away in the down-stream direction. With an Ar flow of 600sccm, the furnace was heated to the desired growth temperature (450°C/550°C/650 °C) at 50 °C/min, followed by oxygen flow at 3sccm for 30 minutes. Under such a highly diluted oxygen environment, the graphene would not be oxidized[176]. During the whole growth process, the chamber was kept under ambient pressure conditions. Afterwards, the tube was cooled down to 25°C.

Graphene Field Effect Transistor Device Fabrication: After graphene layers were transferred on top of Si/SiO₂ substrate, the graphene layers were patterned into rectangular shapes using photolithography and reactive ion etching (RIE). Next, four terminal devices with Ni/Au (8nm/80nm) electrodes were fabricated. Before electrical characterization, the devices were annealed in Ar/H₂ atmosphere at 400°C for 1 hour to remove any organic contaminants and possible photoresist residues from the graphene layer.

Synthesis of ZnO by Hydrothermal and Fabrication of Graphene/ZnO/Graphene Devices: Before the synthesis of ZnO nanowires one metal electrode (Ni/Au, 20/80nm) was deposited by electron beam evaporator (Temescal BJD 1800 system) on graphene bottom electrode. Then single crystal ZnO NWs were synthesized on these graphene films by hydrothermal method. The seeded ZnO solution made of Zinc acetate dehydrate (Zn(CH₃COO)₂·2H₂O, 5mM) in 100mL pure ethanol was spun coated on top of graphene electrode at 1000 RPM for 60s. After baking the graphene samples with seeded ZnO on hot plate at 100 °C for 10 minutes, they were put into the mixture solution of 25mM zinc nitrate hexahydrate (Zn(NO₃)₂·6H₂O) and 25mM hexamethylenetetramine at 90 °C for 2 hours to grow the vertical ZnO NWs. After the synthesis of ZnO NWs the mild HCl (5%) was used to clean metal electrode and the area which was not covered by graphene. After that another graphene film was transferred to the top of ZnO NWs, followed by electron beam deposition of Ni/Au on the top graphene electrode.

5.2.2 Material Characterizations of Graphene/ZnO Hybrid Nanostructures

The morphology of graphene layers were characterized with SEM. The morphology of the large area graphene layers was shown in Figure 5.1a, indicating regions of monolayer and few-layers. The inset AFM phase image shows that there are usually ripple boundary structures where multi-layer graphene is grown. Such boundary structures of graphene layers enhanced the growth of dense array of ZnO nanostructures, observed as bright regions shown in figure 5.1b[176]. The appearance of disorder-induced D band in the Raman spectrum (see figure 3.2) also indicates the existence of these sub-domain boundaries in the graphene layer.

Electrical characterization of the ZnO-Graphene heterostructures was conducted via four-probe measurements, using the device structure shown in the inset of Figure 5.1c. Before the growth of the ZnO nanostructures the measured minimum sheet resistance of the graphene layer was 430Ω per square. From Figure 5.1c we can see that after the synthesis of ZnO nanostructures on the CVD graphene the conductivity of the graphene heterogeneous nanostructures (HGN) dramatically increases. From the am-bipolar I_{ds} - V_{gs} curve in figure 5.1d, the extracted electron and holes mobility before the synthesis of ZnO nanostructures using back-gate measurements are $464\text{cm}^2/\text{V.s}$ and $948\text{cm}^2/\text{V.s}$, respectively. However the ZnO-graphene structures had metallic behavior rather than semimetal one from the I_{ds} - V_{gs} characteristics of the inset of figure 5.1d. This metallic behavior could be due to the highly doping of ZnO to graphene or the highly conductive ZnO nanowires with high doping level or the non-oxidized Zn film on the top of graphene, which needs further investigation. And this enhanced electrical conductivity

makes this ZnO-graphene heterogeneous nanostructures better candidate for the application in optoelectronics.

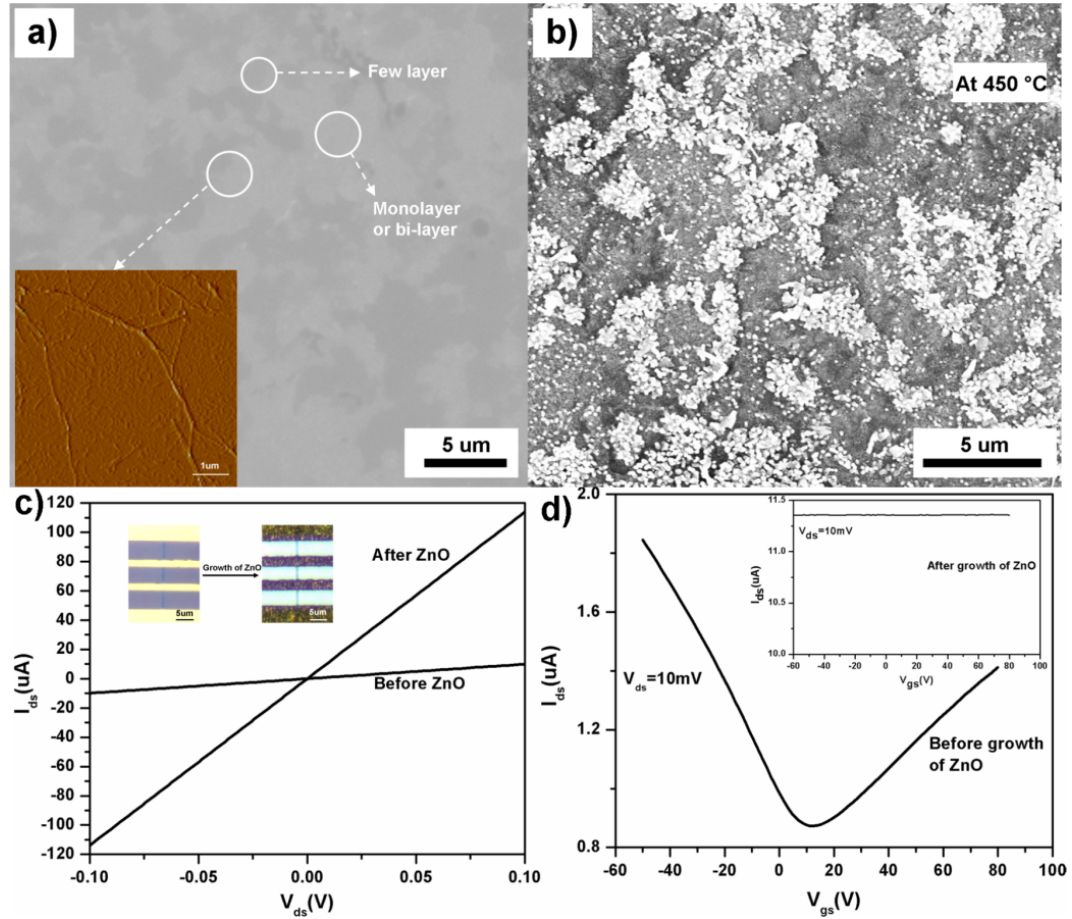


Figure 5.1 (a) SEM image of a CVD grown graphene layer on a SiO₂/Si substrate. The Inset AFM phase image shows the ripples formed on the graphene surface. (b) SEM image of ZnO nanostructures grown on the same CVD-graphene film at 450°C. The bright boundary regions indicate the enhanced growth of ZnO nanostructures. (c) I_{ds} - V_{ds} characteristics of CVD graphene layers before and after the synthesis of ZnO nanostructures. The inset is the four probe device structures before and after synthesis of the ZnO nanostructures. (d) I_{ds} - V_{gs} characteristics of CVD graphene layer before the growth of ZnO nanostructures. The inset shows the metallic behavior of ZnO-graphene heterogeneous nanostructures.

The general morphology of the grown ZnO nanowires is shown in the SEM images in Figure 5.2. From the low magnification image in Figure 5.2a, we observe that the ZnO nanostructures with very large density were more preferably growing over the graphene layer compared to that of the bare SiO₂/Si substrate. The Energy Dispersive X-ray Spectroscopy (EDS) spectrum shown in Figure 5.2b confirms the existence of Zn atoms in these nanostructures, while the carbon peak is from the graphene layer.

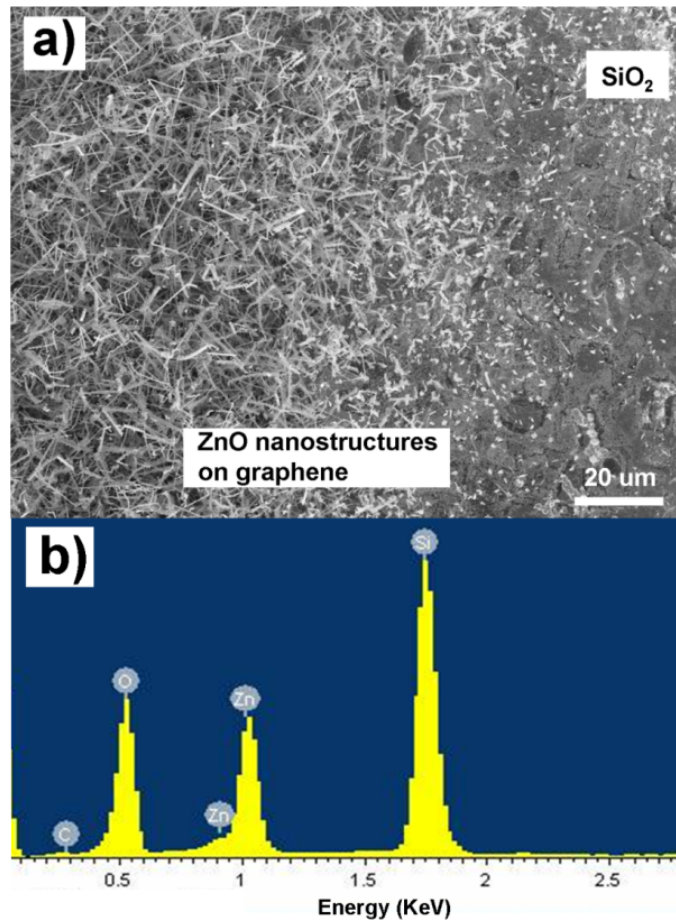


Figure 5.2 (a) Low magnification SEM image of ZnO nanostructures grown on CVD-graphene layer. (b) EDS pattern of ZnO nanostructures on graphene/SiO₂/Si.

Furthermore, the surface morphology of the ZnO nanostructures grown over the graphene layer had strong dependence on the growth temperature. The SEM images in Figure 5.3 show the typical morphology of ZnO nanostructures grown on CVD graphene at 450°C, 550°C and 650°C for 30 minutes. At the lower growth temperature of 450°C, the ZnO nanostructures formed hexagonal cone-shaped nanorods and had average length and diameter of 200 ± 50 nm and 50 ± 10 nm respectively, with a high density of $5\cdot 10^9\text{cm}^{-2}$ which was close to the density of ZnO nanoneedles grown on mechanically exfoliated graphene layers[176]. At the medium growth temperature of 550°C, the ZnO nanostructures had a larger mean diameter of 100 ± 20 nm and length of several hundreds of nanometers with an average areal density of $5\cdot 10^8\text{cm}^{-2}$. When the growth temperature was increased to 650°C, the ZnO nanostructures tend to aggregate together at the root and form the shape of nanoneedles, and the density continued to decrease to $2\cdot 10^8\text{cm}^{-2}$ while the length of the nanoneedles increased to over 1 μm . As noted before for growth along the graphene boundaries, the overall density of nanostructures was higher compared to growth over the flat regions. The decreasing density and higher aspect ratio of ZnO nanostructures on graphene with an increase in growth temperature indicates that the higher temperatures are likely to suppress the nucleation rate of ZnO nanostructures and increase the overall surface diffusion length so that the absorbed atoms migrate more easily over the graphene surface and attach to the end of the nanostructures.

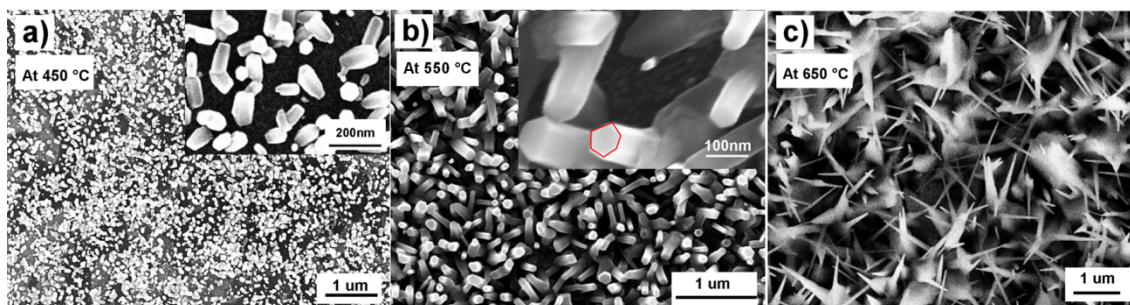


Figure 5.3 SEM images of ZnO nanostructures grown on CVD-graphene layers. (a) At 450°C, the formation of fine ZnO nanorods is observed; (b) coarser nanorods are observed at the 550°C growth temperature; (c) ZnO nanoneedles are grown at 650°C.

Interestingly, when grown using 60 nm diameter gold nanoparticle catalysts at 550°C for 30 minutes, long and dense ZnO nanowires with varying diameter from 20 nm to 100 nm and 10 μm length form out of the roots of short hexagonal cone shaped nanorods (see figure 5.4). These long nanowires aggregated and overlapped to form a “floating web” above a layer of hexagonal cone shaped nanorods. This could be due to the fact that the catalyst nanoparticles enhance the growth rate of ZnO nanostructures.

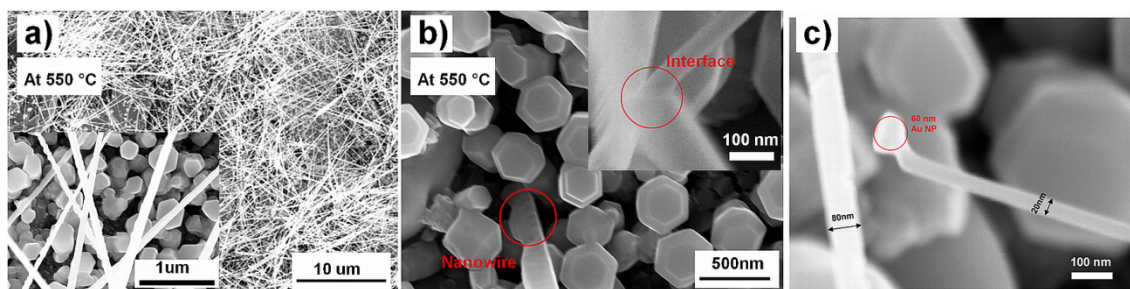


Figure 5.4 SEM images of ZnO nanostructures grown on a graphene layer at 550°C using 60nm gold catalyst nanoparticles. (a) SEM image of entangled long and dense nanowires floating over a layer of short hexagonal cone-shaped nanorods. Inset provides a higher magnification micrograph. (b) SEM image showing the interface between the long nanowires and short nanorods. (c) SEM image showing the gold catalyst nanoparticles and nanowires 20nm and 80 nm in diameter.

X-ray Diffraction (XRD) was employed to characterize the crystal structure of the ZnO nanostructures grown on graphene layers. The consistent XRD pattern of all samples shown in figure 5.5 indicates that the ZnO nanostructures are highly crystalline. The diffraction peaks are indexed to the ZnO hexagonal Wurtzite structure with the lattice constants of $a=0.325\text{nm}$ and $c=0.521\text{nm}$ [181]. The main peak at 34.4° indicates the ZnO nanostructures are preferentially grown along the $\langle 0001 \rangle$ direction. The sharp diffraction peak indicates that the ZnO nanostructures are highly crystalline.

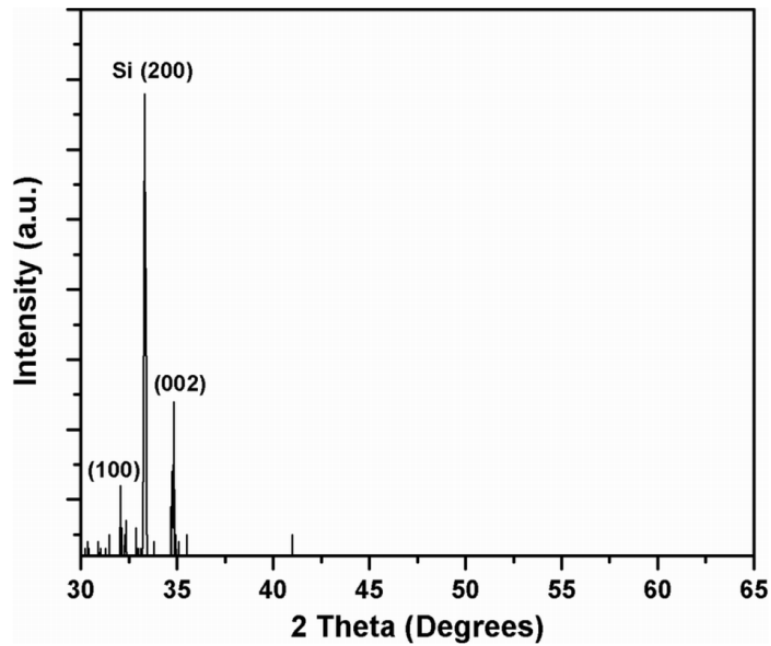


Figure 5.5 XRD pattern of ZnO nanostructures on graphene/SiO₂/Si substrate

5.2.3 Optical Properties of Graphene/ZnO Hybrid Nanostructures

To investigate the optical properties of the heterogeneous graphene nanostructures (HGN), UV spectrometry and photoluminescence spectroscopy were employed. From Figure 5.6a, we can see that the optical transmittance of the 2.5 nm thick graphene layer is nearly 89% before the growth of ZnO nanostructures, which confirms the average number of layers to be less than five[4]. After the growth of the nanostructures, the total transmittance is still maintained at nearly 83%. The photoluminescence spectrum shows the sharp near-band-edge emission peak at around 378nm which originates from the excitonic recombination between the conduction band and the valence band. The suppression of deep-level or trap-state emission at around 540nm indicates the low level of structural defects or impurities[189-191]. From the absorption spectrum shown in the inset of figure 5.6b, the sharp absorption onset from 350nm to 375nm (peak at 370nm) is inspected, which is mainly attributed to the presence of good crystalline and impurity-suppressed ZnO nanostructures. This is consistent with the results of XRD and photoluminescence spectroscopy. From these results, the bandgap of the ZnO nanostructures was estimated to be nearly 3.354 eV, which is also suggested via direct bandgap approximations[192].

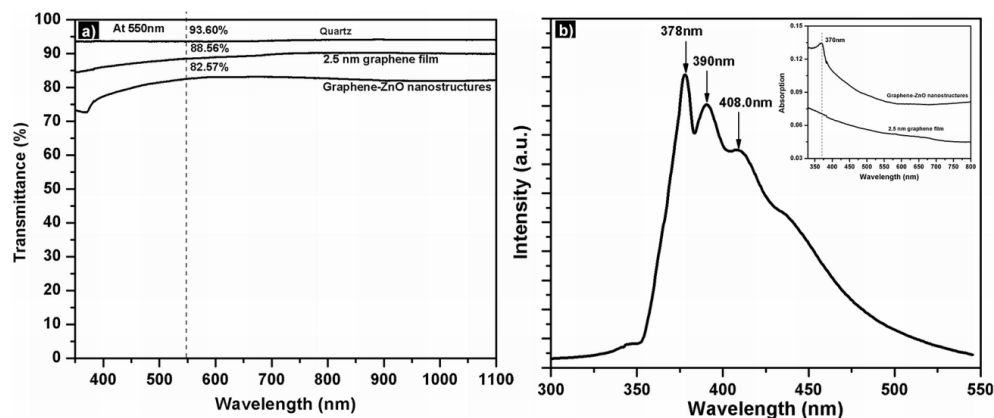


Figure 5.6 (a) Optical transmittance of CVD graphene film with an average thickness of 2.5 nm on a quartz plate, before and after the growth of ZnO nanostructures. (b) Photoluminescence spectrum of ZnO nanostructures grown on a graphene layer. The inset is the UV absorption spectrum of a CVD-graphene layer with an average thickness of 2.5 nm on a quartz plate before and after growth of ZnO nanostructures.

5.2.4 Growth Mechanism

The growth of ZnO nanostructures on CVD grown graphene layers could be explained with a two-step self-catalyzed vapor solid mechanism[193, 194]. At the first step, Zinc atoms from the powder source were vaporized above the melting temperature ($T_m=413^\circ\text{C}$) and then easily deposited on the surface of graphene under Ar atmosphere. This provides two important features: 1) the formed Zinc droplets act as a buffer layer; 2) The coverage of Zinc further prevented the oxidation of graphene by the presence of Oxygen, which could be the reason why the ZnO-graphene structures had much higher conductivity than graphene itself. At the second step, the directed Oxygen caused the oxidation of Zinc atoms. The ZnO seeds precipitated out from the liquidized Zinc because of the very low solubility. Furthermore, the ZnO molecules were preferably arranged along the $\langle 0001 \rangle$ direction in order to lower the surface energy.

5.3 Studies on Electrical and Photoelectrical Properties of Graphene/ZnO/Graphene Hybrid Nanostructures

5.3.1 Material Characterizations

The synthesis procedure of graphene/ZnO/graphene heterostructure is stated in the following steps. First of all, the few-layer graphene films (around 9 layers) were synthesized on copper foil by chemical vapor deposition (CVD) and then transferred to Si/SiO₂ substrate as bottom electrode, shown in figure 5.7a. The transmittance of graphene film at 550nm wavelength from the ultraviolet (UV) spectrum shown in the inset of Fig. 1a indicates that the graphene film consists of around 9 layers[4]. Furthermore, the characterization by Raman spectroscopy confirms few layer graphene film shown in figure 5.7b. Secondly, high density vertical ZnO NWs were synthesized on the graphene (figure 5.7c). The diameters of ZnO NWs are from 40nm to 100nm, which is shown by the higher magnification SEM image inserted in figure 5.7c. Lastly the other graphene film was transferred on the top of ZnO NWs as the top electrode (see figure 5.7d). From the upper-right inset of figure 5.7d it is clear distinguished that ZnO NWs are underneath the transferred graphene film. The Energy Dispersive X-ray Spectroscopy (EDS) spectrum shown in the bottom-left inset of figure 5.7d confirms the existence of Zn atoms in heterostructure, while the carbon peak originates from the graphene layer.

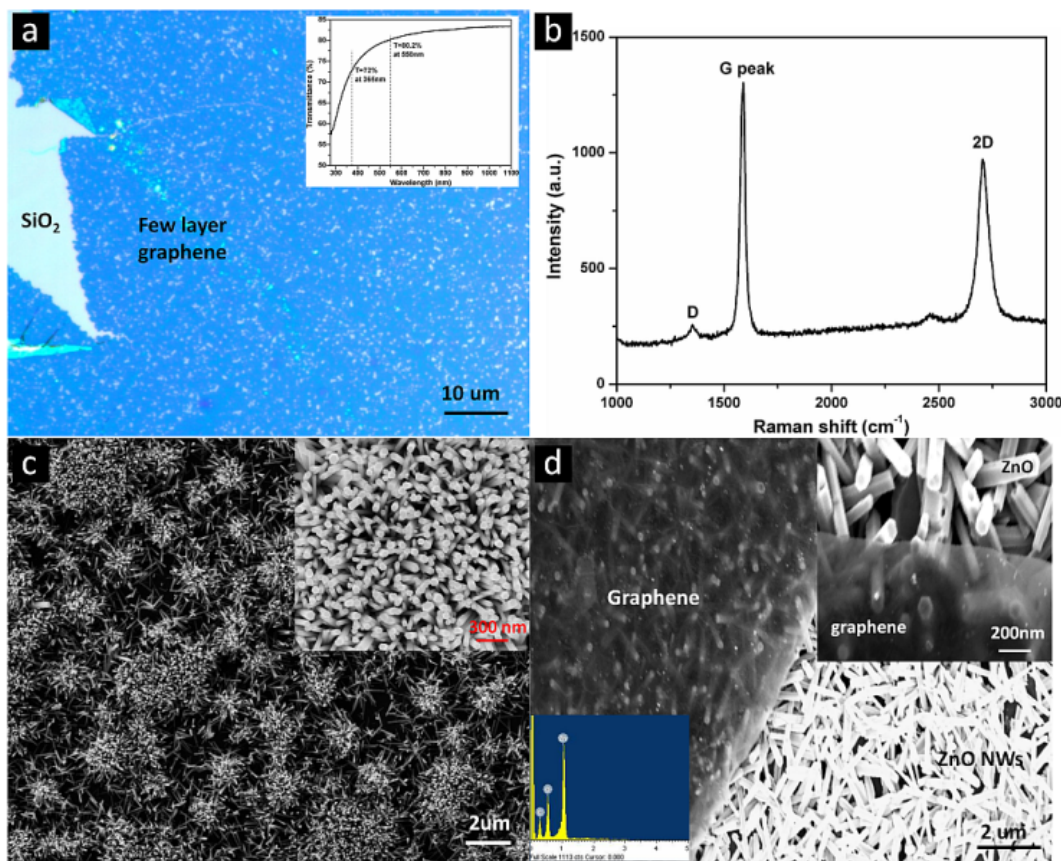


Figure 5.7 (a) Optical image of FLG film transferred on Si substrate with 300nm SiO₂. The inset shows UV-vis spectrum of few layer graphene transferred on quartz substrate. (b) Raman spectrum of FLG film. Raman excitation: 514nm. (c) Top-view SEM image of ZnO nanowires grown on top of CVD graphene at low magnification. Inset is high magnification SEM image of ZnO nanowires grown on graphene. (d) Top view of graphene/ZnO/graphene heterostructure at low magnification. The right-up inset is high magnification SEM image of graphene/ZnO/graphene heterostructure. Left-down inset is the EDS spectrum of graphene/ZnO/graphene heterostructure.

5.3.2 Electrical Properties of Graphene/ZnO/Graphene Hybrid Nanostructures

In order to study the electrical property of graphene/ZnO NWs/graphene, two bi-layer metal electrodes of Ni/Au (20nm/80nm) were deposited by electron beam evaporator (Temescal BJD 1800 system) on the bottom and top graphene electrodes. It is well known that this metal-graphene junction forms Ohmic contact[113]. The schematic of graphene/ZnO NWs/graphene devices with Ni/Au contacts on graphene is illustrated in figure 5.8a. All of the electrical measurements were conducted by using a programmable Agilent 4155C. Figure 5.8b shows the energy-band profile of graphene and ZnO NWs from previously reported values[110]. From the equilibrium energy band diagram of graphene-ZnO junction, shown in figure 5.8c, we can expect that graphene and ZnO NWs forms Ohmic contact. Out of the measured twenty devices, 70% exhibit perfectly linear I-V characteristics as the applied bias voltage is scanned from -1V to 1V (shown in figure 5.8d), indicating the typical Ohmic behavior of the graphene/ZnO/graphene heterostructure. However, we found that there existed four devices out of twenty exhibiting non-linear I-V characteristics (shown in inset of figure 5.8d). It is well known that the work function of graphene can be increased through external species [44, 51, 55], and the Fermi level of n-type ZnO NWs can be altered depending on the doping level. As combined results it could cause work function of graphene greater than that of ZnO NWs. This difference could lead to formation of a potential barrier between the graphene and ZnO NWs when they are in thermal equilibrium, which is indicated in figure 5.8e. This assumption is confirmed by the measured I-V characteristics of two devices (out of twenty) behaving like Schottky diode

with a small potential barrier (shown in figure 5.8f) with turn-on voltage of 0.1-0.2V for forward bias and a reverse bias break-down voltage of -0.2V. If we look into the leakage current between -0.1V and 0.1V (shown in the inset of figure 5.8f) it exhibits the almost linear characteristics from the measured I-V curve, which indicates that this leakage current comes from Ohmic junction between some of ZnO NWs to graphene. Nevertheless, majority of the ZnO NWs form Ohmic contact to graphene although some of them show non-linear characteristics. This result suggests the promising application of graphene/ZnO in solar cell.

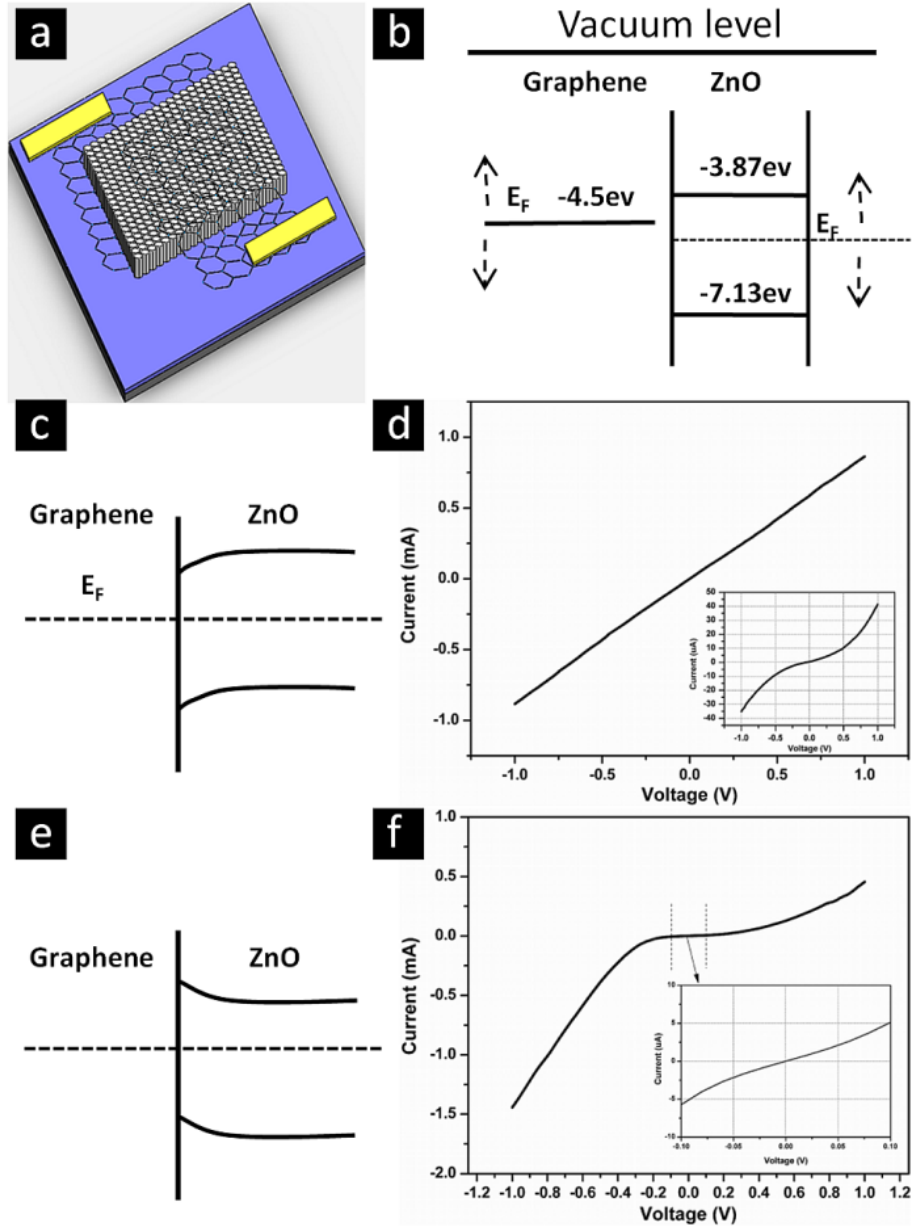


Figure 5.8 (a) Schematic of graphene/ZnO graphene device with Ni/Au contacts on graphene. (b) Energy band profile of metallic graphene and semiconducting ZnO nanowires. The arrows indicate the possible shifts of work function of graphene and the Fermi level of ZnO depending on the doping level. (c) Energy band diagram of graphene and ZnO nanowires junction when $\Phi_{\text{ZnO}} > \Phi_{\text{graphene}}$ (Ohmic contact). (d) I-V characteristic of graphene/ZnO NWs/graphene device showing linear behavior. Inset is the non-linear I-V curve. (e) Energy band diagram of graphene and ZnO nanowires junction when $\Phi_{\text{ZnO}} < \Phi_{\text{graphene}}$ (Schottky contact). (f) I-V characteristic of graphene/ZnO NWs/graphene device showing Schottky behavior. Inset is enlarged I-V curve as voltage from -0.1V to 0.1V.

The electronic transport property of graphene/ZnO/graphene heterostructure was investigated under various temperatures. Since in the practical application for sensor or photo-electronic devices they are operated at room temperature, we focus on the measurement from 300K to 400K at the pressure of 10 mTorr by using MMR's Variable Temperature Micro Probe Systems. The temperatures dependent I-V curve is depicted in figure 5.9. As the temperature increases from 300K to 400K, the current at 1.0V increases to twice the original value at 300K. The poorly fitted curve resulted from logarithm current via reciprocal of temperature based on the thermal excitation mechanism, exhibited in the inset of figure 5.9, shows that the increased conductance cannot simply be explained by thermal excitation of charge carriers from ZnO NWs across the energy band gap. We believe that the graphene electrodes-ZnO NWs junction, as well as desorption of gas molecules from ZnO NWs and graphene might play important roles in the electron transport properties of this heterostructure.

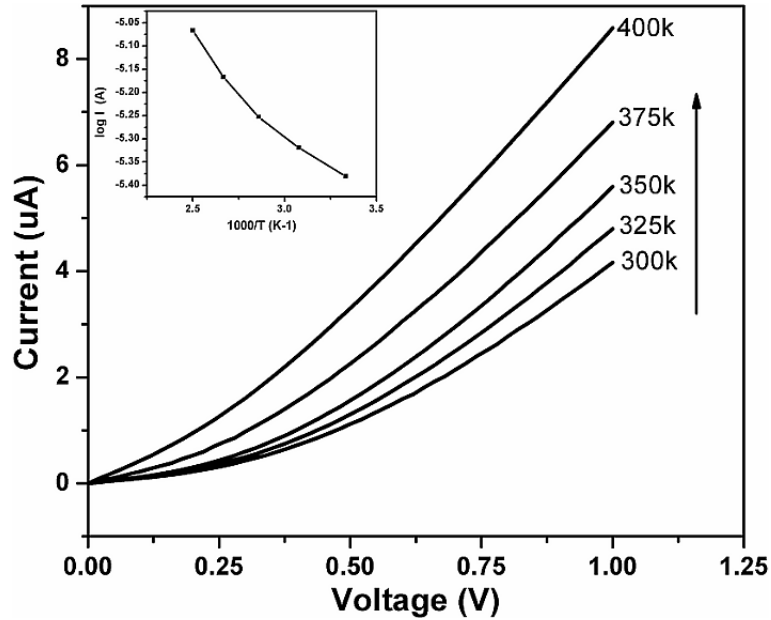


Figure 5.9 I-V curve of graphene/ZnO/graphene device at various temperatures. Inset is the logarithm of the current at 1.0V via the reciprocal temperature.

5.3.3 Photoelectrical Properties of Graphene/ZnO/Graphene Hybrid Nanostructures

To investigate the photoconductivity of graphene/ZnO/graphene, we conducted current-voltage measurement in the ambient environment and compared the current-voltage characteristics both in the dark and upon the illumination of UV light (wavelength: 365nm, power intensity: 4W/cm²). The distance from the UV light to the samples was kept at 10 cm. From I-V curves measured in the dark and upon UV illumination, we can see that conductance pronouncedly increases over the entire voltage bias range for devices with both linear and non-linear I-V characteristics, respectively shown in figure 5.10a and figure 5.10b. However the increase is less than the previously reported values[195, 196], which can be due to the high absorption of graphene at

wavelength of 365nm (see the inset of the figure 5.10a). Figure 5.10c shows the real-time change of conductance upon the UV illumination, represented by the ratio of G/G_0 . It is clearly seen that upon the illumination of UV light the conductance instantaneously increases by four times and recovers to initial conductance when the UV is off. Interestingly, rather than remaining constant[195], the conductance decreases slowly during the UV illumination process. This continuing reduced conductance, we believe, is attributed to the photodesorption effect of gas molecules from top graphene electrode upon the illumination of UV light[37, 42].

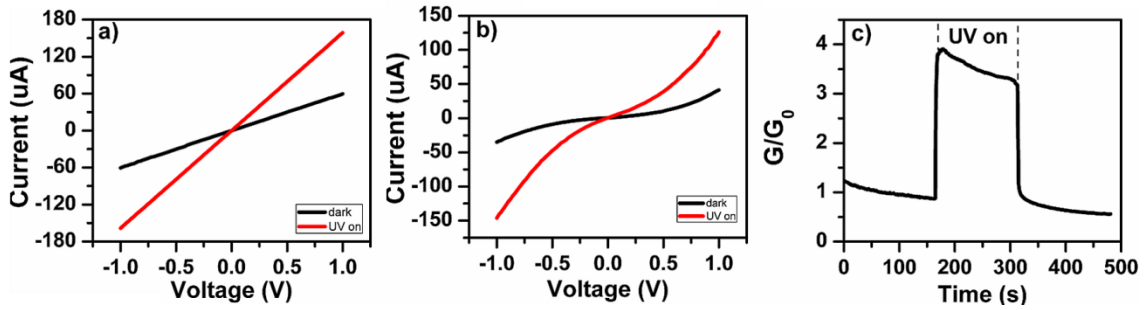


Figure 5.10 Photoconductivity of graphene/ZnO/graphene heterostructure device. (a) I-V characteristic of devices with linear I-V behavior in dark (black) and under 365nm UV illumination (red). (b) I-V characteristic of devices with non-linear I-V behavior in dark (black) and under 365nm UV illumination. (c) Normalized conductance (G/G_0) versus time as the UV illumination is switched on and off. G_0 is the initial conductance.

5.4 Conclusion

Three dimensional heterostructures of CVD grown graphene layers and ZnO nanostructures have been successfully synthesized. The number of graphene layers was under five with low sheet resistance and high optical transmittance. Compared with CVD graphene ZnO-graphene heterogeneous nanostructures had higher electrical conductivity. The surface morphology and dimensions of the ZnO nanostructures highly depend on the growth temperature. Because of the dangling bonds along the graphene boundaries and the disorder among the uniform graphene layers, higher density of ZnO nanostructures were obtained along these boundaries. XRD showed that the highly crystalline ZnO nanostructures were mainly grown along the $\langle 0001 \rangle$ direction. Photoluminescence and UV absorption spectra indicated high optical transmittance and low level of structural defects or impurities.

Graphene/ZnO/graphene heterostructure devices were fabricated to investigate their electrical and photoconductive properties. I-V characteristics of devices in the dark show the good Ohmic contact between ZnO NWs to graphene in majority of devices. UV illumination resulted in the increase of electrical conductance. The further electrical and photoconductive characterization of graphene/ZnO/graphene heterostructure shows graphene has significant effect on the electrical properties of the heterostructure devices. Ultimately, ZnO based HGN could provide building blocks with unique thermal, electrical and optical properties for large-scale applications in high-power UV lasers, optical waveguides, light emitting diodes and solar cells.

Chapter 6 Conclusions

This thesis explores the synthesis of graphene and its hybrid nanostructures as well as their applications in bio-chemical sensors, energy conversion and storage. There are three major contributions of this thesis. The first one is to promote the application of graphene in bio and chemical sensors through investigating the interactions between graphene and bio/gas molecules. The second contribution is to synthesize unique graphene and its three-dimensional hybrid carbon nanostructures (PGN), and the studies on their physical/chemical properties suggest their capabilities in energy conversion/storage applications. Last but not the least; chemical vapor deposition is employed to synthesize the heterogeneous graphene-ZnO nanostructures, the material characterizations and studies on electrical/photoelectrical properties illustrate the potential applications in solar cell and optoelectronics.

Chapter 1 provides the overall review on the 2D graphene and its hybrid nanostructures from the properties, synthesis to applications. It begins with discussion on the graphene crystal and band structure, followed by the brief review in current and potential applications of graphene, including sensors, transparent electrode and energy storage which are relevant to the experimental results presented in chapter 2-5. Then graphene synthesis methods are reviewed to provide overall idea about our experimental work in chapter 3. Lastly, the synthesis and applications of graphene hybrid nanostructures are discussed to understand the state-of-art research directions, which provide basic concepts for the work shown in chapter 4-5.

The experimental work starts with chapter 2, in which graphene field effect transistors are fabricated to study the interaction graphene between single stranded Deoxyribonucleic Acids (ssDNA) and gas molecules. ssDNA are found to act as negative potential gating agents that increase the hole density in single layer graphene (SLG). Later, the molecular photodesorption and absorption from pristine and functionalized graphene fabricated by CVD process is studied. The photodesorption induced current decrease in functionalized graphene by concentrated HNO_3 becomes less significant than pristine graphene layers. Our results provide a new strategy for stabilizing the electrical performance of CVD grown large-area graphene layers for applications ranging from nanoelectronics to optoelectronics.

Experimental studies in synthesis of graphene and its hybrid nanostructures as well as energy applications begin in chapter 3, in which we report the graphene synthesis fabricated CVD process and its application as transparent electrode in organic solar cell. Material and device characterizations show the high electrical conductivity and transmittance of the graphene thin films fabricated by layer to layer transfer. The fabricated organic solar cell based on graphene film as transparent conductive electrode shows potential of graphene to substitute the ITO or FTO in optoelectronics.

In chapter 4, we focus on describing the synthesis of pillar graphene nanostructures comprising vertically aligned MWCNTs on graphene by in situ one-step growth by CVD approach and investigate the application of the unique three-dimensional carbon nanostructures in supercapacitor. Material characterizations illustrate PGN with high surface area, high conductivity and mechanical flexibility. The CV measurement

illustrates excellent specific capacitance and high energy density. The results show the potential application of PGN in energy storage.

Chapter 5 demonstrates the synthesis and characterizations of three dimensional heterostructures graphene nanostructures (HGN) comprising continuous large area graphene layers and ZnO nanostructures, fabricated via chemical vapor deposition. The material characterizations exhibit the highly crystalline ZnO nanostructures synthesized on few-layer graphene films. And Grpahene/ZnO illustrates excellent optical properties. The electrical study on the graphene/ZnO/graphene devices suggests that graphene readily form Ohmic contact to ZnO, although rarely Shockley may exist. The electron transport properties highly depend on the temperature. Devices show photoconductive effect under UV illumination. A combination of electrical and optical properties of graphene and ZnO building blocks in ZnO based HGN provides unique characteristics for opportunities in future optoelectronic devices.

Reference

1. Geim, A. K. and K. S. Novoselov. *The rise of graphene*. Nature Materials, 2007. **6**(3): p. 183-191.
2. Du, X., et al. *Approaching ballistic transport in suspended graphene*. Nature Nanotechnology, 2008. **3**(8): p. 491-495.
3. Balandin, A. A., et al. *Superior thermal conductivity of single-layer graphene*. Nano Letters, 2008. **8**(3): p. 902-907.
4. Nair, R. R., et al. *Fine structure constant defines visual transparency of graphene*. Science, 2008. **320**(5881): p. 1308-1308.
5. Lee, C., et al. *Measurement of the elastic properties and intrinsic strength of monolayer graphene*. Science, 2008. **321**(5887): p. 385-388.
6. Mouras, S., et al. *Synthesis of first stage graphite intercalation compounds with fluorides*. Revue de Chimie Minerale 1987. **24**: p. 572-582.
7. Saito, R., et al. *Electronic-Structure of Graphene Tubules Based on C-60*. Physical Review B, 1992. **46**(3): p. 1804-1811.
8. Forbeaux, I., et al. *Heteroepitaxial graphite on 6H-SiC(0001): Interface formation through conduction-band electronic structure*. Physical Review B, 1998. **58**(24): p. 16396-16406.
9. Wallace, P. R. *The Band Theory of Graphite*. Physical Review, 1947. **71**(9): p. 622-634.
10. Divincenzo, D. P. and E. J. Mele. *Self-Consistent Effective-Mass Theory for Intralayer Screening in Graphite-Intercalation Compounds*. Physical Review B, 1984. **29**(4): p. 1685-1694.
11. Novoselov, K. S., et al. *Electric field effect in atomically thin carbon films*. Science, 2004. **306**(5296): p. 666-669.
12. Fasolino, A., et al. *Intrinsic ripples in graphene*. Nature Materials, 2007. **6**(11): p. 858-861.
13. Lang, B. *Leed Study of Deposition of Carbon on Platinum Crystal-Surfaces*. Surface Science, 1975. **53**(Dec): p. 317-329.

14. Oshima, C. and A. Nagashima. *Ultra-thin epitaxial films of graphite and hexagonal boron nitride on solid surfaces*. Journal of Physics-Condensed Matter, 1997. **9**(1): p. 1-20.
15. Viculis, L. M., et al. *A chemical route to carbon nanoscrolls*. Science, 2003. **299**(5611): p. 1361-1361.
16. Shioyama, H. *Cleavage of graphite to graphene*. Journal of Materials Science Letters, 2001. **20**(6): p. 499-500.
17. Novoselov, K. S., et al. *Two-dimensional gas of massless Dirac fermions in graphene*. Nature, 2005. **438**(7065): p. 197-200.
18. Zhang, Y. B., et al. *Experimental observation of the quantum Hall effect and Berry's phase in graphene*. Nature, 2005. **438**(7065): p. 201-204.
19. Kroto, H. W., et al. *C-60 - Buckminsterfullerene*. Nature, 1985. **318**(6042): p. 162-163.
20. Iijima, S. *Helical Microtubules of Graphitic Carbon*. Nature, 1991. **354**(6348): p. 56-58.
21. Johnston, D. F. *The Structure of the Pi-Band of Graphite*. Proceedings of the Royal Society of London Series a-Mathematical and Physical Sciences, 1955. **227**(1170): p. 349-358.
22. Charlier, J. C., et al. *Tight-Binding Model for the Electronic-Properties of Simple Hexagonal Graphite*. Physical Review B, 1991. **44**(24): p. 13237-13249.
23. Schwierz, F. *Graphene transistors*. Nature Nanotechnology, 2010. **5**(7): p. 487-496.
24. Morales, A. M. and C. M. Lieber. *A laser ablation method for the synthesis of crystalline semiconductor nanowires*. Science, 1998. **279**(5348): p. 208-211.
25. Cui, Y., et al. *High performance silicon nanowire field effect transistors*. Nano Letters, 2003. **3**(2): p. 149-152.
26. Ryu, K., et al. *CMOS-Analogous Wafer-Scale Nanotube-on-Insulator Approach for Submicrometer Devices and Integrated Circuits Using Aligned Nanotubes*. Nano Letters, 2009. **9**(1): p. 189-197.
27. Baughman, R. H., et al. *Carbon nanotubes - the route toward applications*. Science, 2002. **297**(5582): p. 787-792.

28. Morozov, S. V., et al. *Electron transport in graphene*. Physics-Uspekhi, 2008. **51**(7): p. 744-748.
29. Liu, G., et al. *Low-frequency electronic noise in the double-gate single-layer graphene transistors*. Applied Physics Letters, 2009. **95**(3): p. -.
30. Lin, Y. M., et al. *100-GHz Transistors from Wafer-Scale Epitaxial Graphene*. Science, 2010. **327**(5966): p. 662-662.
31. Li, X. L., et al. *Chemically derived, ultrasmooth graphene nanoribbon semiconductors*. Science, 2008. **319**(5867): p. 1229-1232.
32. Wang, X. R., et al. *Room-temperature all-semiconducting sub-10-nm graphene nanoribbon field-effect transistors*. Physical Review Letters, 2008. **100**(20): p. -.
33. Schedin, F., et al. *Detection of individual gas molecules adsorbed on graphene*. Nature Materials, 2007. **6**(9): p. 652-655.
34. Leenaerts, O., et al. *Adsorption of H₂O, NH₃, CO, NO₂, and NO on graphene: A first-principles study*. Physical Review B, 2008. **77**(12): p. -.
35. Ao, Z. M., et al. *Correlation of the applied electrical field and CO adsorption/desorption behavior on Al-doped graphene*. Solid State Communications, 2010. **150**(13-14): p. 680-683.
36. Huang, B., et al. *Adsorption of gas molecules on graphene nanoribbons and its implication for nanoscale molecule sensor*. Journal of Physical Chemistry C, 2008. **112**(35): p. 13442-13446.
37. Shi, Y. M., et al. *Photoelectrical Response in Single-Layer Graphene Transistors*. Small, 2009. **5**(17): p. 2005-2011.
38. Sundaram, R. S., et al. *Electrochemical modification of graphene*. Advanced Materials, 2008. **20**(16): p. 3050-3053.
39. Dan, Y. P., et al. *Intrinsic Response of Graphene Vapor Sensors*. Nano Letters, 2009. **9**(4): p. 1472-1475.
40. Fowler, J. D., et al. *Practical Chemical Sensors from Chemically Derived Graphene*. ACS Nano, 2009. **3**(2): p. 301-306.
41. Romero, H. E., et al. *Adsorption of ammonia on graphene*. Nanotechnology, 2009. **20**(24): p. -.

42. Lin, J., et al. *Molecular Absorption and Photodesorption in Pristine and Functionalized Large-Area Graphene Layers*. submitted, 2011. p.
43. Mohanty, N. and V. Berry. *Graphene-Based Single-Bacterium Resolution Biodevice and DNA Transistor: Interfacing Graphene Derivatives with Nanoscale and Microscale Biocomponents*. Nano Letters, 2008. **8**(12): p. 4469-4476.
44. Lin, J., et al. *Gating of Single-Layer Graphene with Single-Stranded Deoxyribonucleic Acids*. Small, 2010. **6**(10): p. 1150-1155.
45. Shan, C. S., et al. *Direct Electrochemistry of Glucose Oxidase and Biosensing for Glucose Based on Graphene*. Analytical Chemistry, 2009. **81**(6): p. 2378-2382.
46. Alwarappan, S., et al. *Probing the Electrochemical Properties of Graphene Nanosheets for Biosensing Applications*. Journal of Physical Chemistry C, 2009. **113**(20): p. 8853-8857.
47. Wang, Y., et al. *Large area, continuous, few-layered graphene as anodes in organic photovoltaic devices*. Applied Physics Letters, 2009. **95**(6): p. -.
48. Blake, P., et al. *Graphene-based liquid crystal device*. Nano Letters, 2008. **8**(6): p. 1704-1708.
49. Wang, X., et al. *Transparent, conductive graphene electrodes for dye-sensitized solar cells*. Nano Letters, 2008. **8**(1): p. 323-327.
50. De Arco, L. G., et al. *Continuous, Highly Flexible, and Transparent Graphene Films by Chemical Vapor Deposition for Organic Photovoltaics*. ACS Nano, 2010. **4**(5): p. 2865-2873.
51. Bae, S., et al. *Roll-to-roll production of 30-inch graphene films for transparent electrodes*. Nature Nanotechnology, 2010. **5**(8): p. 574-578.
52. Kim, K. S., et al. *Large-scale pattern growth of graphene films for stretchable transparent electrodes*. Nature, 2009. **457**(7230): p. 706-710.
53. Li, X. S., et al. *Large-Area Synthesis of High-Quality and Uniform Graphene Films on Copper Foils*. Science, 2009. **324**(5932): p. 1312-1314.
54. Reina, A., et al. *Layer Area, Few-Layer Graphene Films on Arbitrary Substrates by Chemical Vapor Deposition*. Nano Letters, 2009. **9**(8): p. 3087-3087.
55. Shi, Y. M., et al. *Work Function Engineering of Graphene Electrode via Chemical Doping*. ACS Nano, 2010. **4**(5): p. 2689-2694.

56. Conway, B. E. *Transition from Supercapacitor to Battery Behavior in Electrochemical Energy-Storage*. Journal of the Electrochemical Society, 1991. **138**(6): p. 1539-1548.
57. Stoller, M. D., et al. *Graphene-Based Ultracapacitors*. Nano Letters, 2008. **8**(10): p. 3498-3502.
58. Wang, Y., et al. *Supercapacitor Devices Based on Graphene Materials*. Journal of Physical Chemistry C, 2009. **113**(30): p. 13103-13107.
59. Zhu, Y. W., et al. *Microwave assisted exfoliation and reduction of graphite oxide for ultracapacitors*. Carbon, 2010. **48**(7): p. 2118-2122.
60. Zhu, Y. W., et al. *Exfoliation of Graphite Oxide in Propylene Carbonate and Thermal Reduction of the Resulting Graphene Oxide Platelets*. Acs Nano, 2010. **4**(2): p. 1227-1233.
61. Yu, A. P., et al. *Ultrathin, transparent, and flexible graphene films for supercapacitor application*. Applied Physics Letters, 2010. **96**(25): p. -.
62. Liu, C. G., et al. *Graphene-Based Supercapacitor with an Ultrahigh Energy Density*. Nano Letters, 2010. **10**(12): p. 4863-4868.
63. Pandolfo, A. G. and A. F. Hollenkamp. *Carbon properties and their role in supercapacitors*. Journal of Power Sources, 2006. **157**(1): p. 11-27.
64. Miller, J. R., et al. *Graphene Double-Layer Capacitor with ac Line-Filtering Performance*. Science, 2010. **329**(5999): p. 1637-1639.
65. Yoo, J. J., et al. *Ultrathin Planar Graphene Supercapacitors*. Nano Letters, 2011. **11**(4): p. 1423-1427.
66. Choi, W., et al. *Synthesis of Graphene and Its Applications: A Review*. Critical Reviews in Solid State and Materials Sciences, 2010. **35**(1): p. 52-71.
67. Rokuta, E., et al. *Vibrational spectra of the monolayer films of hexagonal boron nitride and graphite on faceted Ni(755)*. Surface Science, 1999. **428**: p. 97-101.
68. Nagashima, A., et al. *Electronic states of the heteroepitaxial double-layer system: Graphite/monolayer hexagonal boron nitride/Ni(111)*. Physical Review B, 1996. **54**(19): p. 13491-13494.

69. Novoselov, K. S., et al. *Two-dimensional atomic crystals*. Proceedings of the National Academy of Sciences of the United States of America, 2005. **102**(30): p. 10451-10453.
70. Viculis, L. M., et al. *Chemical route towards graphite nanoplatelets and carbon nanoscrolls*. Abstracts of Papers of the American Chemical Society, 2003. **226**: p. U761-U761.
71. Calizo, I., et al. *Temperature dependence of the Raman spectra of graphene and graphene multilayers*. Nano Letters, 2007. **7**(9): p. 2645-2649.
72. Pisana, S., et al. *Breakdown of the adiabatic Born-Oppenheimer approximation in graphene*. Nature Materials, 2007. **6**(3): p. 198-201.
73. Stankovich, S., et al. *Synthesis and exfoliation of isocyanate-treated graphene oxide nanoplatelets*. Carbon, 2006. **44**(15): p. 3342-3347.
74. Stankovich, S., et al. *Stable aqueous dispersions of graphitic nanoplatelets via the reduction of exfoliated graphite oxide in the presence of poly(sodium 4-styrenesulfonate)*. Journal of Materials Chemistry, 2006. **16**(2): p. 155-158.
75. Hernandez, Y., et al. *High-yield production of graphene by liquid-phase exfoliation of graphite*. Nature Nanotechnology, 2008. **3**(9): p. 563-568.
76. Lotya, M., et al. *Liquid Phase Production of Graphene by Exfoliation of Graphite in Surfactant/Water Solutions*. Journal of the American Chemical Society, 2009. **131**(10): p. 3611-3620.
77. Wu, X. S., et al. *Weak antilocalization in epitaxial graphene: Evidence for chiral electrons*. Physical Review Letters, 2007. **98**(13): p. -.
78. Sadowski, M. L., et al. *Landau level spectroscopy of ultrathin graphite layers*. Physical Review Letters, 2006. **97**(26): p. -.
79. Sprinkle, M., et al. *Scalable templated growth of graphene nanoribbons on SiC*. Nature Nanotechnology, 2010. **5**(10): p. 727-731.
80. Vanbommel, A. J., et al. *Leed and Auger-Electron Observations of Sic (0001) Surface*. Surface Science, 1975. **48**(2): p. 463-472.
81. Hass, J., et al. *The growth and morphology of epitaxial multilayer graphene*. Journal of Physics-Condensed Matter, 2008. **20**(32): p. -.

82. Juang, Z. Y., et al. *Synthesis of graphene on silicon carbide substrates at low temperature*. Carbon, 2009. **47**(8): p. 2026-2031.
83. Emtsev, K. V., et al. *Towards wafer-size graphene layers by atmospheric pressure graphitization of silicon carbide*. Nature Materials, 2009. **8**(3): p. 203-207.
84. Somani, P. R., et al. *Planer nano-graphenes from camphor by CVD*. Chemical Physics Letters, 2006. **430**(1-3): p. 56-59.
85. Obraztsov, A. N., et al. *Chemical vapor deposition of thin graphite films of nanometer thickness*. Carbon, 2007. **45**(10): p. 2017-2021.
86. Yu, Q. K., et al. *Graphene segregated on Ni surfaces and transferred to insulators*. Applied Physics Letters, 2008. **93**(11): p. -.
87. Wang, X. B., et al. *Large-Scale Synthesis of Few-Layered Graphene using CVD*. Chemical Vapor Deposition, 2009. **15**(1-3): p. 53-56.
88. Sutter, E., et al. *Graphene growth on polycrystalline Ru thin films*. Applied Physics Letters, 2009. **95**(13): p. -.
89. Sutter, P. W., et al. *Epitaxial graphene on ruthenium*. Nature Materials, 2008. **7**(5): p. 406-411.
90. Li, X. S., et al. *Evolution of Graphene Growth on Ni and Cu by Carbon Isotope Labeling*. Nano Letters, 2009. **9**(12): p. 4268-4272.
91. Kosynkin, D. V., et al. *Longitudinal unzipping of carbon nanotubes to form graphene nanoribbons*. Nature, 2009. **458**(7240): p. 872-U875.
92. Jiao, L. Y., et al. *Narrow graphene nanoribbons from carbon nanotubes*. Nature, 2009. **458**(7240): p. 877-880.
93. Cano-Marquez, A. G., et al. *Ex-MWNTs: Graphene Sheets and Ribbons Produced by Lithium Intercalation and Exfoliation of Carbon Nanotubes*. Nano Letters, 2009. **9**(4): p. 1527-1533.
94. Wang, J. J., et al. *Free-standing subnanometer graphite sheets*. Applied Physics Letters, 2004. **85**(7): p. 1265-1267.
95. Wang, J. J., et al. *Synthesis of carbon nanosheets by inductively coupled radio-frequency plasma enhanced chemical vapor deposition*. Carbon, 2004. **42**(14): p. 2867-2872.

96. Bai, H., et al. *Functional Composite Materials Based on Chemically Converted Graphene*. *Advanced Materials*, 2011. **23**(9): p. 1089-1115.
97. Guo, S. J., et al. *Platinum Nanoparticle Ensemble-on-Graphene Hybrid Nanosheet: One-Pot, Rapid Synthesis, and Used as New Electrode Material for Electrochemical Sensing*. *Acs Nano*, 2010. **4**(7): p. 3959-3968.
98. Scheuermann, G. M., et al. *Palladium Nanoparticles on Graphite Oxide and Its Functionalized Graphene Derivatives as Highly Active Catalysts for the Suzuki-Miyaura Coupling Reaction*. *Journal of the American Chemical Society*, 2009. **131**(23): p. 8262-8270.
99. Kamat, P. V. *Graphene-Based Nanoassemblies for Energy Conversion*. *Journal of Physical Chemistry Letters*, 2011. **2**(3): p. 242-251.
100. Lin, J., et al. *Flexible Pillar graphene nanostructures films for supercapacitor*. submitted, 2011. p.
101. Cai, D. Y., et al. *Highly conductive carbon-nanotube/graphite-oxide hybrid films*. *Advanced Materials*, 2008. **20**(9): p. 1706-+.
102. Yu, D. S. and L. M. Dai. *Self-Assembled Graphene/Carbon Nanotube Hybrid Films for Supercapacitors*. *Journal of Physical Chemistry Letters*, 2010. **1**(2): p. 467-470.
103. Yoo, E., et al. *Large reversible Li storage of graphene nanosheet families for use in rechargeable lithium ion batteries*. *Nano Letters*, 2008. **8**(8): p. 2277-2282.
104. Watcharotone, S., et al. *Graphene-silica composite thin films as transparent conductors*. *Nano Letters*, 2007. **7**(7): p. 1888-1892.
105. Choi, K. S., et al. *Fabrication of Free-Standing Multilayered Graphene and Poly(3,4-ethylenedioxythiophene) Composite Films with Enhanced Conductive and Mechanical Properties*. *Langmuir*, 2010. **26**(15): p. 12902-12908.
106. Zhao, X., et al. *Enhanced Mechanical Properties of Graphene-Based Poly(vinyl alcohol) Composites*. *Macromolecules*, 2010. **43**(5): p. 2357-2363.
107. Hong, T. K., et al. *Transparent, Flexible Conducting Hybrid Multi layer Thin Films of Multiwalled Carbon Nanotubes with Graphene Nanosheets*. *Acs Nano*, 2010. **4**(7): p. 3861-3868.
108. Kim, Y. K. and D. H. Min. *Durable Large-Area Thin Films of Graphene/Carbon Nanotube Double Layers as a Transparent Electrode*. *Langmuir*, 2009. **25**(19): p. 11302-11306.

109. Kong, B. S., et al. *Layer-by-layer assembly of graphene and gold nanoparticles by vacuum filtration and spontaneous reduction of gold ions*. Chemical Communications, 2009. (16): p. 2174-2176.
110. Hwang, J. O., et al. *Vertical ZnO nanowires/graphene hybrids for transparent and flexible field emission*. Journal of Materials Chemistry, 2010. **online publication**: p.
111. Lee, D. H., et al. *Versatile Carbon Hybrid Films Composed of Vertical Carbon Nanotubes Grown on Mechanically Compliant Graphene Films*. Advanced Materials, 2010. **22**(11): p. 1247-+.
112. Paul, R. K., et al. *Synthesis of pillared graphene nanostructure: a counterpart of three dimensional carbon architecture*. Small, 2010. **6**(20): p. 2309-2313.
113. Lin, J., et al. *Heterogeneous Graphene Nanostructures: ZnO Nanostructures Grown on Large-Area Graphene Layers*. Small, 2010. **6**(21): p. 2448-2452.
114. Sundaram, R. S., et al. *Electrochemical modification of graphene*. Advanced Materials, 2008. **20**(16): p. 3050-3053.
115. D. C. Elias, R. R. N., 1* T. M. G. Mohiuddin, 1 S. V. Morozov, 2 P. Blake, 3 M. P. Halsall, 1 A. C. Ferrari, 4 D. W. Boukhvalov, 5 M. I. Katsnelson, 5 A. K. Geim, 1, 3 K. S. Novoselov 1{dagger} *Control of Graphene's Properties by Reversible Hydrogenation: Evidence for Graphane*. Science, 2009. **323**: p.
116. Dong, X. C., et al. *Symmetry Breaking of Graphene Monolayers by Molecular Decoration*. Physical Review Letters, 2009. **102**(13): p. -.
117. Chen, W., et al. *Surface transfer p-type doping of epitaxial graphene*. Journal of the American Chemical Society, 2007. **129**(34): p. 10418-10422.
118. Dong, X. C., et al. *Doping Single-Layer Graphene with Aromatic Molecules*. Small, 2009. **5**(12): p. 1422-1426.
119. Xu, Y., et al. *Double-stranded DNA single-walled carbon nanotube hybrids for optical hydrogen peroxide and glucose sensing*. Journal of Physical Chemistry C, 2007. **111**(24): p. 8638-8643.
120. Johnson, R. R., et al. *Probing the structure of DNA-carbon nanotube hybrids with molecular dynamics*. Nano Letters, 2008. **8**(1): p. 69-75.
121. Zheng, M., et al. *DNA-assisted dispersion and separation of carbon nanotubes*. Nature Materials, 2003. **2**(5): p. 338-342.

122. Zheng, M., et al. *Structure-based carbon nanotube sorting by sequence-dependent DNA assembly*. Science, 2003. **302**(5650): p. 1545-1548.
123. Wang, X., et al. *Carbon Nanotube-DNA nanoarchitectures and electronic functionality*. Small, 2006. **2**(11): p. 1356-1365.
124. Calizo, I., et al. *The effect of substrates on the Raman spectrum of graphene: Graphene-on-sapphire and graphene-on-glass*. Applied Physics Letters, 2007. **91**(20): p. 201904.
125. Calizo, I., et al. *Variable temperature Raman microscopy as a nanometrology tool for graphene layers and graphene-based devices*. Applied Physics Letters, 2007. **91**(7): p. 071913.
126. Parvizi, F., et al. *Properties of graphene produced by the high pressure-high temperature growth process*. Micro & Nano Letters, 2008. **3**(1): p. 29-34.
127. Teweldebrhan, D. and A. A. Balandin. *Modification of graphene properties due to electron-beam irradiation*. Applied Physics Letters, 2009. **94**(1): p. 013101.
128. Adam, S., et al. *A self-consistent theory for graphene transport*. Proceedings of the National Academy of Sciences of the United States of America, 2007. **104**(47): p. 18392-18397.
129. Krstic, V., et al. *Graphene-metal interface: Two-terminal resistance of low-mobility graphene in high magnetic fields*. Nano Letters, 2008. **8**(6): p. 1700-1703.
130. Chen, J. H., et al. *Charged-impurity scattering in graphene*. Nature Physics, 2008. **4**(5): p. 377-381.
131. Tan, Y. W., et al. *Measurement of scattering rate and minimum conductivity in graphene*. Physical Review Letters, 2007. **99**(24): p. -.
132. Artyukhin, A. B., et al. *Controlled electrostatic gating of carbon nanotube FET devices*. Nano Letters, 2006. **6**(9): p. 2080-2085.
133. Ferrari, A. C., et al. *Raman spectrum of graphene and graphene layers*. Physical Review Letters, 2006. **97**(18): p. -.
134. Das, A., et al. *Monitoring dopants by Raman scattering in an electrochemically top-gated graphene transistor*. Nature Nanotechnology, 2008. **3**(4): p. 210-215.
135. Yan, J., et al. *Electric field effect tuning of electron-phonon coupling in graphene*. Physical Review Letters, 2007. **98**(16): p. -.

136. Casiraghi, C., et al. *Raman fingerprint of charged impurities in graphene*. Applied Physics Letters, 2007. **91**(23): p. 233108
137. Stampfer, C., et al. *Raman imaging of doping domains in graphene on SiO₂*. Applied Physics Letters, 2007. **91**(24): p. 241907.
138. Ishigami, M., et al. *Atomic structure of graphene on SiO₂*. Nano Letters, 2007. **7**(6): p. 1643-1648.
139. Lazzeri, M. and F. Mauri. *Nonadiabatic Kohn anomaly in a doped graphene monolayer*. Physical Review Letters, 2006. **97**(26): p. 266407
140. Meng, S., et al. *Determination of DNA-base orientation on carbon nanotubes through directional optical absorbance*. Nano Letters, 2007. **7**(8): p. 2312-2316.
141. Sankey, O. F. and D. J. Niklewski. *Abinitio Multicenter Tight-Binding Model for Molecular-Dynamics Simulations and Other Applications in Covalent Systems*. Physical Review B, 1989. **40**(6): p. 3979-3995.
142. Lewis, J. P., et al. *Further developments in the local-orbital density-functional-theory tight-binding method*. Physical Review B, 2001. **64**(19): p. 195103.
143. Jelinek, P., et al. *Multicenter approach to the exchange-correlation interactions in ab initio tight-binding methods*. Physical Review B, 2005. **71**(23): p. 215101.
144. Mullard, P. J. L. a. W. G. NIST Chemistry Webbook, 2008. **69**: p. <http://webbook.nist.gov/chemistry>.
145. Chen, E. S. and E. C. M. Chen. *The negative ion states of molecules: Adenine and guanine*. Biochemical and Biophysical Research Communications, 2001. **289**(2): p. 421-426.
146. Giovannetti, G., et al. *Doping graphene with metal contacts*. Physical Review Letters, 2008. **101**(2): p. 026803.
147. Wehling, T. O., et al. *Molecular doping of graphene*. Nano Letters, 2008. **8**(1): p. 173-177.
148. Zhang, H., et al. *Growth Mechanism of Graphene on Ru(0001) and O-2 Adsorption on the Graphene/Ru(0001) Surface*. Journal of Physical Chemistry C, 2009. **113**(19): p. 8296-8301.
149. Chen, R. J., et al. *Molecular photodesorption from single-walled carbon nanotubes*. Applied Physics Letters, 2001. **79**(14): p. 2258-2260.

150. Shim, M. and G. P. Siddons. *Photoinduced conductivity changes in carbon nanotube transistors*. Applied Physics Letters, 2003. **83**(17): p. 3564-3566.
151. Romero, H. E., et al. *n-Type Behavior of Graphene Supported on Si/SiO₂ Substrates*. ACS Nano, 2008. **2**(10): p. 2037-2044.
152. Lin, J. A., et al. *Gating of Single-Layer Graphene with Single-Stranded Deoxyribonucleic Acids*. Small, 2010. **6**(10): p. 1150-1155.
153. Wang, X. R., et al. *N-Doping of Graphene Through Electrothermal Reactions with Ammonia*. Science, 2009. **324**(5928): p. 768-771.
154. Rusu, C. N. and J. T. Yates. *Defect sites on TiO₂(110). Detection by O-2 photodesorption*. Langmuir, 1997. **13**(16): p. 4311-4316.
155. Robinson, J. A., et al. *Role of defects in single-walled carbon nanotube chemical sensors*. Nano Letters, 2006. **6**(8): p. 1747-1751.
156. Hirsch, A. and O. Vostrowsky. *Functionalization of carbon nanotubes*. Functional Molecular Nanostructures, 2005. **245**: p. 193-237.
157. Lee, S., et al. *Wafer Scale Homogeneous Bilayer Graphene Films by Chemical Vapor Deposition*. Nano Letters, 2010. **10**(11): p. 4702-4707.
158. Wang, Y., et al. *Interface Engineering of Layer-by-Layer Stacked Graphene Anodes for High-Performance Organic Solar Cells*. Advanced Materials, 2011. **23**(13): p. 1514-1518.
159. Bonnefoi, L., et al. *Electrode optimisation for carbon power supercapacitors*. Journal of Power Sources, 1999. **79**(1): p. 37-42.
160. Yoon, B. J., et al. *Electrical properties of electrical double layer capacitors with integrated carbon nanotube electrodes*. Chemical Physics Letters, 2004. **388**(1-3): p. 170-174.
161. Nutzenadel, C., et al. *Electrochemical storage of hydrogen in nanotube materials*. Electrochemical and Solid State Letters, 1999. **2**(1): p. 30-32.
162. Michael, M. S. and S. R. S. Prabakaran. *High voltage electrochemical double layer capacitors using conductive carbons as additives*. Journal of Power Sources, 2004. **136**(2): p. 250-256.
163. Du, C. S. and N. Pan. *Supercapacitors using carbon nanotubes films by electrophoretic deposition*. Journal of Power Sources, 2006. **160**(2): p. 1487-1494.

164. Hu, L. B., et al. *Highly conductive paper for energy-storage devices*. Proceedings of the National Academy of Sciences of the United States of America, 2009. **106**(51): p. 21490-21494.
165. Xie, X., et al. *Three-Dimensional Carbon Nanotube-Textile Anode for High-Performance Microbial Fuel Cells*. Nano Letters, 2011. **11**(1): p. 291-296.
166. Dimitrakakis, G. K., et al. *Pillared Graphene: A New 3-D Network Nanostructure for Enhanced Hydrogen Storage*. Nano Letters, 2008. **8**(10): p. 3166-3170.
167. Kondo, D., et al. *Self-organization of novel carbon composite structure: Graphene multi-layers combined perpendicularly with aligned carbon nanotubes*. Applied Physics Express, 2008. **1**(7): p. 3.
168. Tung, V. C., et al. *Low-Temperature Solution Processing of Graphene-Carbon Nanotube Hybrid Materials for High-Performance Transparent Conductors*. Nano Letters, 2009. **9**(5): p. 1949-1955.
169. Li, C. Y., et al. *Graphene Nano-"patches" on a Carbon Nanotube Network for Highly Transparent/Conductive Thin Film Applications*. Journal of Physical Chemistry C, 2010. **114**(33): p. 14008-14012.
170. Lu, W., et al. *High performance electrochemical capacitors from aligned carbon nanotube electrodes and ionic liquid electrolytes*. Journal of Power Sources, 2009. **189**(2): p. 1270-1277.
171. Dresselhaus, M. S., et al. *Raman spectroscopy of carbon nanotubes*. Physics Reports-Review Section of Physics Letters, 2005. **409**(2): p. 47-99.
172. Qu, D. Y. *Studies of the activated carbons used in double-layer supercapacitors*. Journal of Power Sources, 2002. **109**(2): p. 403-411.
173. Pasta, M., et al. *Aqueous supercapacitors on conductive cotton*. Nano Research, 2010. **3**(6): p. 452-458.
174. Frackowiak, E. and F. Beguin. *Electrochemical storage of energy in carbon nanotubes and nanostructured carbons*. Carbon, 2002. **40**(10): p. 1775-1787.
175. Duck Hyun Lee, J. E. K., Tae Hee Han, Jae Won Hwang, Seokwoo Jeon, Sung-Yool Choi, Soon Hyung Hong, Won Jong Lee, and a. S. O. K. Rodney S. Ruoff. *Versatile Carbon Hybrid Films Composed of Vertical Carbon Nanotubes Grown on Mechanically Compliant Graphene Films*. Adv. Mater, 2010. (22): p.

176. Kim, Y. J., et al. *Vertically aligned ZnO nanostructures grown on graphene layers*. Applied Physics Letters, 2009. **95**(21): p. -.
177. Sungjin Park, N. M., Ji Won Suk, Ashvin Nagaraja, Jinho An, Richard D. Piner, Weiwei Cai, Daniel R. Dreyer, Vikas Berry,* and Rodney S. Ruoff. *Biocompatible, Robust Free-Standing Paper Composed of a TWEEN/Graphene Composite*. Adv. Mater., 2010. (22): p.
178. Eda, G., et al. *Large-area ultrathin films of reduced graphene oxide as a transparent and flexible electronic material*. Nature Nanotechnology, 2008. **3**(5): p. 270-274.
179. Berger, C., et al. *Electronic confinement and coherence in patterned epitaxial graphene*. Science, 2006. **312**(5777): p. 1191-1196.
180. Wei, D. C., et al. *Synthesis of N-Doped Graphene by Chemical Vapor Deposition and Its Electrical Properties*. Nano Letters, 2009. **9**(5): p. 1752-1758.
181. Yang, P. D., et al. *Controlled growth of ZnO nanowires and their optical properties*. Advanced Functional Materials, 2002. **12**(5): p. 323-331.
182. Junpeng Liu, S. W., Zuqiang Bian, Meina Shan, and Chunhui Huang. *Organic/inorganic hybrid solar cells with vertically oriented ZnO nanowires*. Applied Physics Letters, 2009. **94**(17): p. 173107.
183. Law, M., et al. *Nanowire dye-sensitized solar cells*. Nature Materials, 2005. **4**(6): p. 455-459.
184. Wang, X. D., et al. *Direct-current nanogenerator driven by ultrasonic waves*. Science, 2007. **316**(5821): p. 102-105.
185. Wang, Z. L. and J. H. Song. *Piezoelectric nanogenerators based on zinc oxide nanowire arrays*. Science, 2006. **312**(5771): p. 242-246.
186. Yoon, H., et al. *Aluminum foil mediated noncatalytic growth of ZnO nanowire arrays on an indium tin oxide substrate*. Journal of Physical Chemistry C, 2008. **112**(25): p. 9181-9185.
187. Fan, H. J., et al. *Self-assembly of ZnO nanowires and the spatial resolved characterization of their luminescence*. Nanotechnology, 2004. **15**(11): p. 1401-1404.
188. Wang, X. D., et al. *Growth of uniformly aligned ZnO nanowire heterojunction arrays on GaN, AlN, and Al_{0.5}Ga_{0.5}N substrates*. Journal of the American Chemical Society, 2005. **127**(21): p. 7920-7923.

189. Park, W. I., et al. *Excitonic emissions observed in ZnO single crystal nanorods*. Applied Physics Letters, 2003. **82**(6): p. 964-966.
190. Park, W. I., et al. *ZnO nanoneedles grown vertically on Si substrates by non-catalytic vapor-phase epitaxy*. Advanced Materials, 2002. **14**(24): p. 1841-1843.
191. Jung, S. W., et al. *Time-resolved and time-integrated photoluminescence in ZnO epilayers grown on Al₂O₃(0001) by metalorganic vapor phase epitaxy*. Applied Physics Letters, 2002. **80**(11): p. 1924-1926.
192. Anthony, S. P., et al. *Tuning optical band gap of vertically aligned ZnO nanowire arrays grown by homoepitaxial electrodeposition*. Applied Physics Letters, 2007. **90**(10): p. -.
193. Tseng, Y. K., et al. *Two-step oxygen injection process for growing ZnO nanorods*. Journal of Materials Research, 2003. **18**(12): p. 2837-2844.
194. Hu, J. Q., et al. *Synthesis of uniform hexagonal prismatic ZnO whiskers*. Chemistry of Materials, 2002. **14**(3): p. 1216-1219.
195. Li, Q. H., et al. *Electronic transport through individual ZnO nanowires*. Applied Physics Letters, 2004. **84**(22): p. 4556-4558.
196. Kind, H., et al. *Nanowire ultraviolet photodetectors and optical switches*. Advanced Materials, 2002. **14**(2): p. 158-+.